

**Cancer Drug Screening Scale-up:
Combining Biomimetic Microfluidic Platforms
and Deep Learning Image Analysis**

by

Zhixiong Zhang

A dissertation submitted in partial fulfillment
of the requirements for the degree of
Doctor of Philosophy
(Electrical and Computer Engineering)
in the University of Michigan
2020

Doctoral Committee:

Professor Euisik Yoon, Chair
Dr. Yu-Chih Chen
Professor Jacques E. Nor
Professor Kensall D. Wise

Zhixiong Zhang
zzxlmzcg@gmail.com
ORCID iD: 0000-0001-6542-7257

© Zhixiong Zhang, 2020

Table of Contents

List of Figures	iv
List of Tables	vii
Abstract	viii
Chapter 1 : Introduction	1
1. 1 Cancer Drug Development Status	1
1. 2 Conventional phenotypic drug screening	3
1. 3 Tumor Microenvironment (TME)	4
1. 4 Research goal of biomimetic drug screening platform	5
1. 5 Deep learning image analysis for high-throughput drug screening	6
Chapter 2 : Microfluidics 3D Gel-Island Chip for Single Cell Isolation and Lineage-Dependent Drug Responses Study	8
2.1 Introduction.....	9
2.2 Design of gel-island chip	11
2.3 Single cell loading and cell culture	12
2.4 Cancer cell differentiation study	17
2.5 Cancer drug susceptibility test	20
2.6 Chapter summary	22
Chapter 3 : Scalable Multiplexed Drug-Combination Screening Platforms Using 3D Microtumor Model for Precision Medicine	24
3.1 Introduction.....	25
3.2 Microfluidic filter structure for cell capture and sphere formation.....	27
3.3 Microfluidic tree structure as logarithmic concentration gradient generator	29
3.4 Mixer array and drug inlets “Sudoku puzzle”	32
3.5 Multiple PDMS layers for drug mixing and routing.....	37
3.6 Validation of logarithmic concentration gradient on-chip.....	38
3.7 Cancer cell loading and sphere formation	41
3.8 Synergy effect analysis	41

3.9 Drug combination screening on breast and pancreatic cancer cell lines	42
3.10 Drug Combination screening on pancreatic cancer PDX cell line	46
3.11 Chapter summary	51
Chapter 4 : High-Throughput Microfluidic Clonal Sphere Chip Identifies Cancer Stem Cells Located at the Leading Edge of Tumorigenic Subclones	52
4.1 Introduction.....	53
4.2 Hi-Sphere chip for clonal sphere culture	55
4.3 Chip flipping strategy for sphere culture	58
4.4 Size-based selective sphere retrieval for inter-sphere heterogeneity study.....	59
4.5 Cell tracker staining enabling intra-sphere heterogeneity study	61
4.6 High aldehyde dehydrogenase activity in leading edge cells	64
4.7 Secondary generation sphere formation comparison between leading edge and core	66
4.8 Chapter summary	67
Chapter 5 : Label-free Estimation of Therapeutic Efficacy on 3D Cancer Spheres Using Convolutional Neural Network Image Analysis	69
5.1 Introduction.....	70
5.2 Design of the cancer sphere platform	73
5.3 Morphological changes of spheres after drug treatment.....	75
5.4 Estimation of cancer sphere viability using brightfield microscopy	77
5.5 Critical morphology features for sphere viability prediction	81
5.6 Inter-drug model validation and mixed prediction for different drugs	83
5.7 Chapter summary	84
Chapter 6 : Morphology-based Prediction of Cancer Cell Migration Using Artificial Neural Network and Random Decision Forest.....	86
6.1 Introduction.....	87
6.2 Morphological prediction of cell migration pipeline	89
6.3 Microfluidic single cell migration chip design and cell migration experiment.....	90
6.4 Mitochondrial classification and image processing.....	92
6.5 Feature extraction and data pre-processing	95
6.6 Cell migration direction prediction	96
6.7 Cell motility (migration speed) prediction	100
6.8 Validation of morphological features by altering cell migration behaviors.....	103
6.9 Chapter summary	105
Chapter 7 : Conclusions	108
7.1 Summary.....	108

7.2 Future works	112
7.2.1 Pharmacokinetic study:	112
7.2.2 Interpretable deep learning model to understand cancer cell behavior	113
References	114

List of Figures

Figure 1-1. Cost of Developing a New Drug	2
Figure 1-2. Pre-clinical Drug Screening Models.....	4
Figure 1-3. Tumor microenvironment components.....	5
Figure 2-1. Overview of the gel-island chip design	12
Figure 2-2. Gel-island loading process with single cell encapsulation	13
Figure 2-3. Long-term cell culture capability.....	15
Figure 2-4. Diffusion test using dextran-conjugated fluorescein to verify conformal mass transfer inside culture chambers	16
Figure 2-5. MDA-MB-231 and T47D breast cancer cells cultured in conventional petri-dish for 7 days .	17
Figure 2-6. T47D breast cancer cell differentiation.....	18
Figure 2-7. Distribution of Notch reporter gene fluorescent intensity ratio between 48h (day2) and 6h (day0) after cell loading under 2 culture conditions: 3D collagen gels (black, N=209), and 2D culture media (red, N=116).....	19
Figure 2-8. Drug susceptibility test of T47D Notch+ breast cancer cells under 2mg/mL 3D collagen gel condition, cultured on chip for 48 hours followed by 72 hours drug treatment	21
Figure 3-1. Schematics of multiplexed 8-drug combination screening chip.....	28
Figure 3-2. COMSOL simulation results for logarithmic “Christmas tree mixer” structure	30
Figure 3-3. Formation of uniform spheres	32
Figure 3-4. Schematics of multiplexed 8-drug combination screening chip.....	38
Figure 3-5. Generation of linear and logarithmic concentration gradient validated by fluorescent dye	40
Figure 3-6. Drug combination screening results of control (culture media) and 7 drugs (Cisplatin, Docetaxel, Doxorubicin, Gemcitabine, Irinotecan, Oxaliplatin, 5-FU) using pancreatic cancer cell line MIA PaCa-2.....	43
Figure 3-7. SUM159 and MCF7 drug combination susceptibility test.....	45

Figure 3-8. Chip-to-chip variance characterization experiment. We repeated drug combination screening experiments on breast cancer cell line SUM159, using 4 fabricated chips under identical treatment conditions.....	46
Figure 3-9. Drug combination screening results of UM5 using 7 commonly used chemo-drugs and control (culture media).....	48
Figure 3-10. Drug combination screening results of UM16 using 7 commonly used chemo-drugs and control (culture media).....	49
Figure 3-11. Drug combination screening results of UM53 using 7 commonly used chemo-drugs and control (culture media).....	50
Figure 3-12. Drug combination screening results of control (culture media) and 7 drugs (Cisplatin, Docetaxel, Doxorubicin, Gemcitabine, Irinotecan, Oxaliplatin, 5-FU) using pancreatic cancer PDX cells.....	50
Figure 4-1. Overview of the Hi-Sphere chip design.....	56
Figure 4-2. Sphere culture and size tracking using Hi-Sphere chip.....	57
Figure 4-3. Hi-Sphere selective retrieval for inter-sphere heterogeneity study	60
Figure 4-4. Holo-sphere retrieval and staining to identify cells located at sphere edge and sphere core ...	63
Figure 4-5. Comparison of ALDH activity between sphere leading edge and sphere core	65
Figure 4-6. 2nd sphere formation rate comparison between leading edge and center	66
Figure 5-1. Tumor sphere chip and culture chamber.....	74
Figure 5-2. Cell loading in a sphere chamber and sphere aggregation	75
Figure 5-3. Cancer spheres treated by Doxorubicin. Representative images of SUM159 cancer spheres treated by Doxorubicin with six different concentrations.....	76
Figure 5-4. Cancer spheres classification and drug inhibition score regression using brightfield image and CNN model.....	78
Figure 5-5. Cancer spheres classification and drug inhibition score regression for Doxorubicin	80
Figure 5-6. Cancer spheres classification and drug inhibition score regression for Oxaliplatin	81
Figure 5-7. Neural network structure and trained filters for prediction	82
Figure 5-8. Inter-drug model validation and prediction model combining different drugs.....	84
Figure 6-1. Workflow of critical morphological features discovery in cell migration, which includes microfluidic migration chip experiments, high-content imaging, image processing, machine learning modelling, and control experiment validation.	90
Figure 6-2. Microfluidic migration chip overview	91
Figure 6-3. Image processing flow for the original microscope image (a-f) and mitochondrial classification (g, h).....	94

Figure 6-4. Morphological feature correlation heatmap.....	96
Figure 6-5. Results and important features for cell migration direction prediction	98
Figure 6-6. Selected important features for cell migration direction/speed prediction	99
Figure 6-7. Cell migration speed prediction.....	101
Figure 6-8. Typical images for normal/drug-pretreated/motile cells and medium value differences of selected important features for cell migration direction/speed prediction. (a-c) Typical images for normal/drug-pretreated/motile cells	104

List of Tables

Table 3-1. Example drug inlets layout for 4 drugs	32
Table 3-2. Initialization of adjacency matrix.	34
Table 3-3. Filling adjacency matrix at the second line next to diagonal with “a”.	34
Table 3-4. Filling adjacency matrix at the third line next to diagonal with “b”.	35
Table 3-5. Filling adjacency matrix at the fourth line next to diagonal with “c”.	35
Table 3-6. Completion of adjacency matrix.	36
Table 3-7. Example drug inlets layout for 16 drugs. Number 1~16 stands for 16 different drugs.	36

Abstract

The development of cancer drugs is usually costly and time-consuming, mainly due to growing complexity in screening large number of candidate compounds and high failure rates in translation from preclinical trials to clinical approval. Despite the great efforts, the preclinical screening platforms combining good clinical relevance and high throughput for large-scale drug testing is still lacking. In addition, accumulating evidence suggests that cancer drug response can be altered by tumor microenvironment (TME), which includes not only cancer cells but also physical, and biochemical cues in niches. To improve the current cancer drug screening assays, it is important to mimic local TME to achieve better physiological relevance. In the first part of this dissertation, three TME-mimicking microfluidic platforms were introduced for three different *in-vitro* TME-mimicking tumor sphere models: spheres in matrix, self-aggregated spheres, and single-cell clonal spheres. First, a 3D gel-island chip investigated the heterogeneity of single-cell drug responses in biomimetic extracellular matrix (ECM). With 1,500 isolated single cell chambers containing ECM, it was demonstrated that ECM support was favorable for some population of cancer cells to maintain stemness and develop drug resistance. This result suggested the importance of drug screening at single-cell resolution in TME-mimicking platforms. Secondly, a drug combination screening chip enabling high-throughput and scalable combinatorial drug screening was demonstrated for the aggregated sphere model. Instead of screening a single drug on each of the tumors, this chip allows the screening of all pairwise drug combinations from eight different cancer drugs, in total 172 different treatment conditions, and 1,032 tested samples in a single microfluidic chip. The presented design approach was easily scalable to incorporate arbitrary number of drugs for large-scale drug screening. Finally, single-cell Hi-Sphere chip enabled high-throughput clonal sphere culture and selective retrieval. Combining

fluorescent dye on-situ staining techniques, we identified rare cancer stem-like cell population and confirms its location at the leading edge of spheres.

Advance in experimental throughput generates massive data, which demands the corresponding automatic analysis and intelligent interpretation capabilities. The second part of this dissertation focuses on the applications of computer vision and machine learning algorithms to automated biomedical data processing. Image analysis with convolutional neural network was applied for drug efficacy evaluation in a fast and label-free manner. The estimated drug efficacy is highly correlated with the experimental ground truth (R -value > 0.93), while the predicted half-maximal inhibitory concentration is within 8% error range. In addition, metastatic fast-moving cells could be identified after extracting morphological features from the microscope images and applying deep learning algorithm for image analysis, achieving over 99% accuracy for cell movement direction prediction and 91% for speed prediction. In summary, this dissertation presents high-throughput TME-mimicking microfluidics and deep learning image analysis for large-scale drug screening solutions.

Chapter 1 : Introduction

1. 1 Cancer Drug Development Status

The development of effective cancer drug has always been the central topic in both clinical and industrial cancer research [1-4]. For the last several decades, more than 100 anticancer drugs have been discovered and approved by the FDA [5, 6], with the overall cancer death rate declined by 29% from 1991 to 2017 [7]. Despite the success, the development of cancer drug is very costly and time consuming. It can take between 10 and 15 years to develop a new drug, at a cost of about US\$2.6 billion. [8, 9]. There are three main steps in drug development and testing: preclinical trials, when the drug compound is discovered and first tested; clinical trial, which is when the drug is tested in people; and post-clinical research, which takes place after the drug is approved [10, 11] (Fig. 1-1). Despite the great initiative and efforts to improve drug development procedures and techniques, only 0.03% of candidate compound from preclinical trials are eventually approved by the FDA [12]. In fact, many compounds yielding promising preclinical efficacy fail in performing desirably in clinical trials [13, 14]. There is an unmet need develop better preclinical drug screening model to fill the gap between preclinical drug testing model and translation to human trials.

In general, there are two strategies for preclinical cancer drug development: phenotypic screening and genotypic target screening [15, 16]. Facilitated by the advancement of genetic profiling tools, genotypic target screening has been the dominant choice in pharmaceuticals

development for the past decade [17]. This hypothesis-driven method is based on the detection of mutations or alteration at specific molecular locations in human genome that are known to be responsible for certain cancers [18, 19]. However, the limited knowledge of complexed human genome content and drug mechanism of action, together with the frequent treatment failures due

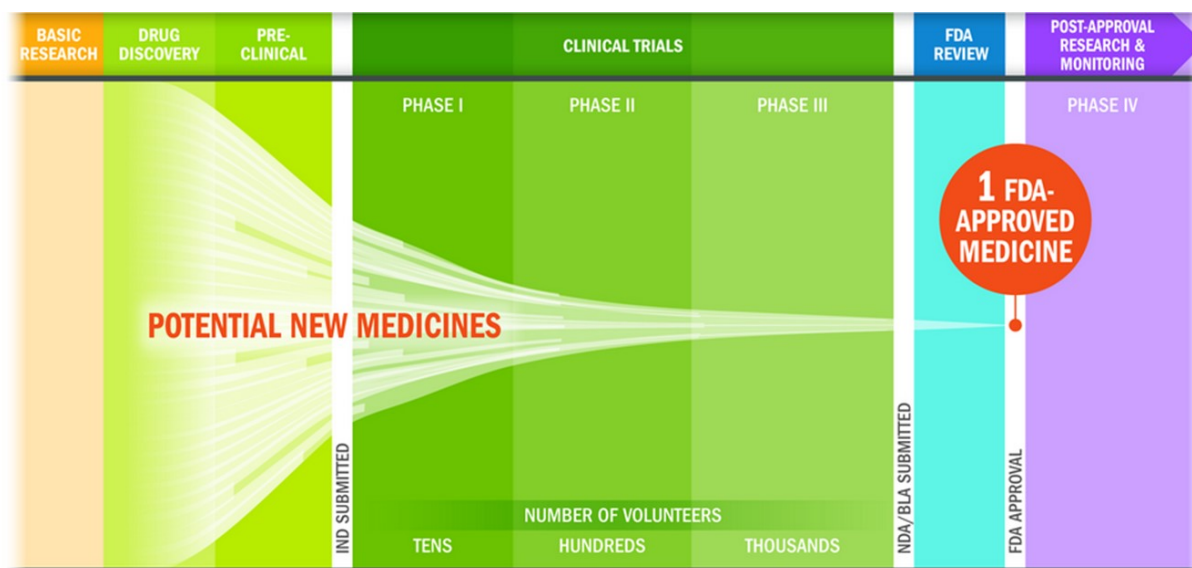


Figure 1-1. “Cost of Developing a New Drug”. Tufts CSDD & School of Medicine and US FDA Infographics, Nov. 2014.

to acquired resistance [20, 21], have led people to realize the limitation of genetic method and regain interest in phenotypic screening to identify potential drug candidates [22, 23]. The phenotypic screening method is an unbiased approach based on the measures of drug response, which does not merely rely on the knowledge of specific drug target [24, 25]. Recent development of phenotypic screening research focuses on not only cell viability and growth rate [26], but a comprehensive investigation on various cancer behaviors including morphologies, differentiation, metastatic and metabolic activities, cellular interactions [27-29] and many other features in a quantitative manner [30]. The improvement in 3D cellular phenotyping models, like multicellular

co-culture organoid and “tissue on a chip”, is also narrowing the gap between in-vitro assays and in-vivo assays [31, 32].

1. 2 Conventional phenotypic drug screening

Traditionally, the most widely used *in-vivo* model is using whole living animals to investigate the effect of any therapeutic candidate or to study any biological process. This model has good physiology mimicking capability with minimal genetic drift. However, the long experiment time and the high costs limits its application in large-scale drug screening [33]. There are many ethical debates on the justice of having animals under certain experimental conditions and unnecessary sacrifice [34]. Another popular phenotypic drug screening model is two-dimensional (2D) model, where cancer cells are cultured on planar surface made from polystyrene or glass. This monolayer cell culture model has the merit of high-throughput, low-cost, and good repeatability. However, this simple model usually generates quite different outcomes from the clinical trials [35, 36]. From the drug screening point of view, this discrepancy is possibly caused by failing to reflect the complex physiology of tissue-specific architecture and mechanical/biochemical signals. [37-39]. 2D cancer model also largely alters cellular phenotypic/genetic characteristic and thus, drug response. People has been trying to find a sweet spot between throughput requirement and physiological relevance. With the recent development in cell culture platforms, 3D cell culture becomes a promising technique with good potential in mimicking the key factors of local physiological properties and preserving tumor heterogeneity and drug resistance [40]. Yet, a good 3D cancer drug screening platform requires careful design to incorporate different component that have influence on cancer drug responses (Fig. 1-2). There is

an unmet need to develop high-throughput drug screening platforms for large-scale in-vitro drug screening that recapitulate tumors' response to chemo-drugs under various 3D cell culture.

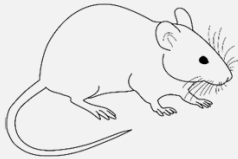
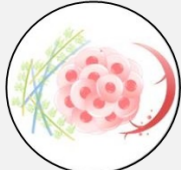
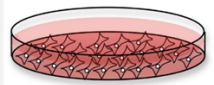
	 Animal Model	 3D Sphere Model	 2D Plates Model
Pros	<ul style="list-style-type: none"> • Good physiology recapitulation • Minimal genetic drift 	<ul style="list-style-type: none"> • Mimic native tumor environment • Preserve tumor heterogeneity and drug resistance 	<ul style="list-style-type: none"> • Simple to use, good repeatability • High throughput and low cost
Cons	High cost, long turnaround time, sacrifice animals	Require carefully-designed tumor microenvironment	Largely alter cell characteristic and drug response



Figure 1-2. Pre-clinical Drug Screening Models.

1.3 Tumor Microenvironment (TME)

Tumor, as heterogeneous populations of malfunctional cells, is surrounded by collections of stromal cells, blood vessels, extracellular matrix (ECM), and other molecular cues (Fig. 1-3) [41, 42]. By sending and receiving both mechanical and biochemical signals from microenvironments, solid tumor establishes favorable conditions for growth and acquires the essential hallmark functions [43-46] including uncontrolled proliferation, transformation, and invasion. Accumulating evidence suggest that TME plays an important role in tumor cells

acquiring therapeutic response and resistance [47-51], by preventing drug molecule penetration, inducing cancer phenotype transition, and facilitating genetic mutations [51, 52]. For this reason, more and more cancer studies have been trying to mimic TME to simulate tumor therapeutic response under local environment and targeting the TME to overcome cancer acquired resistance and eventually improve clinical outcome [52-54].

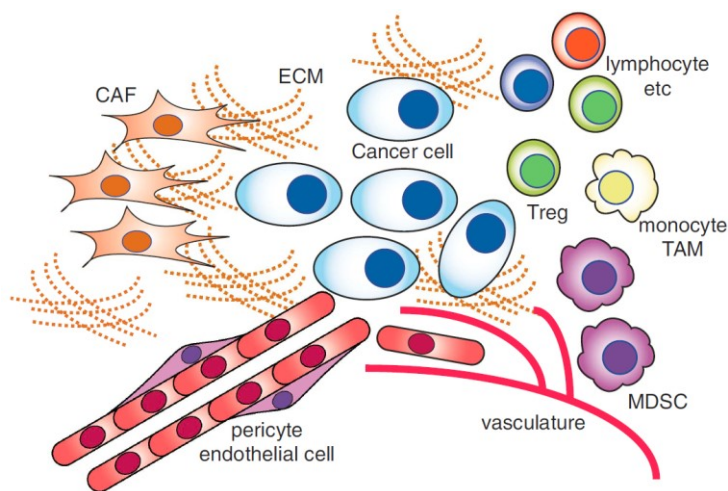


Figure 1-3. Tumor microenvironment components [16]

1. 4 Research goal of biomimetic drug screening platform

To facilitate the study of cancer drug, we present three microfluidic platform, 3D gel-island chip, drug combination screening chip, and single cell hi-chip, to mimic a variety of different tumor microenvironments. The 3D gel-island chip was designed to study single cell drug response under the condition with solid ECM support, and its influence in cancer cell differentiation and drug response. In addition, the drug combination screening platform was designed to achieve scalable high-throughput drug combination screening using a self-aggregated spheroid model, which recapitulate tumor 3D spherical structure and reflects more clinical-relevant combinatorial

drug efficacy compared to conventional 2D drug screening assays. Finally, the single cell Hi-Sphere chip enables high-throughput clonal sphere culture and retrieval. With the help of Hi-Sphere chip, we identified Tumor Initiating Cells (TICs) or Cancer Stem Cells (CSCs) in different tumor clones and different locations in single clones, which has been widely believed that give rise to tumor progression, metastasis, and chemo-drug resistance.

1. 5 Deep learning image analysis for high-throughput drug screening

In recent decades, microfluidics has shown great potential in advancing biotechnology applications in regards of high-throughput parallelization, small sample handling, and wide range of functionality [55]. The development of microfluidic technology provided us with considerably large amount of data, including biomedical images, videos, cellular behavioral measurements and sequence reading data [56]. Yet, the lack of the capability of analyzing the vast amount of data has become the bottleneck in biological discovery [57]. On the other hand, due to the advent of large-scale data computing and storage, machine learning techniques, especially deep learning, has enabled rapid analysis of complex biomedical images in a high-throughput manner. An increasing number of research works paired microfluidic devices with machine learning tools to realize system automation and data analysis in biology. Previous work includes single cell counting [58], label-free screening [59] and classification [60, 61], cancer diagnosis [62].

Despite the increasing number of works integrating machine learning and microfluidics, very few applies machine learning techniques in drug screening studies, which is a data-abundant and labor-intensive field. In the latter chapters of this dissertation, we applied deep learning to two microfluidic cancer drug studies. The first deep learning model achieves label-free measurement

of cancer cell drug responses. By analyzing brightfield microscope images of drug-treatment tumors with different doses, the cell viability and drug efficacy could be accurately predicted without relying on cell viability fluorescent assays. In the second work, cell migratory direction and speed were predicted based on morphological features using computer vision and machine learning algorithms. Combined with drug treatment experiment, we established the correlation between cellular morphology and cancer cell metastasis behavior.

Chapter 2 : Microfluidics 3D Gel-Island Chip for Single Cell

Isolation and Lineage-Dependent Drug Responses Study

One of the most important components in TME is extracellular matrix (ECM), which not only provides structural support to cellular constituents, but also initiates regulatory biochemical cues for a variety of important cell functions in tissue. The application of ECM has become more and more important in understanding cancer pathology and drug testing. Although the ECM-gel has been used in the cell culture both in bulk and on-chip, previous works focus on the collective cell behaviors rather than single-cell heterogeneity. To track the behavior of each individual cells, we developed a gel-island chip, which can form thousands of islands containing single cells encapsulated by desired ECM. Optimized by Poisson's distribution, the device can attain 34% capture efficiency of exact single cell per island. Good culture media exchange rate and high cell viability can be achieved in the gel-islands. The cells in the islands can be automatically counted for high-throughput analysis. As the proof of concept, we monitored the proliferation and differentiation of single Notch⁺ (stem-like) T47D breast cancer cells. The 3D collagen gel environment was found to be favorable for stem-like phenotype through better more self-renewal and de-differentiation (Notch⁻ to Notch⁺ transition). More interestingly, we found that the Notch-de-differentiated cells were more resistant to doxorubicin and cisplatin than the Notch⁺ cells. Combining 3D ECM culture and single cell resolution, the presented platform can automatically analyze the individual cell behaviors of hundreds of cells using small amount of drug and reagents.

2.1 Introduction

In-vitro cell culture has been widely used in cell behavior study for more than 100 years. However, it is not until 80's that people started to highlight the importance of 3D cell culture, especially for understanding the roles of extracellular matrix (ECM) in the tissue physiology and cancer pathology [1]. To bridge the different drug responses between conventional 2D cell culture and in-vivo experiment, more and more cancer studies are performing experiments in the more realistic 3D culture environment [2-3]. Compared to the 2D culture, which grows cells on artificial rigid polystyrene (Young's modulus: 3 GPa) or glass (Young's modulus: 50-90 GPa), 3D culture grows cells in the elastic ECM (Young's modulus: 50-5000 Pa, depending on tissues) environment and can better mimic the in-vivo environment [4-7]. In addition to the mechanical property, cells are known to sense the biochemical signals from surrounding ECM using various signal transduction cascades via the receptors on the cell membrane [8]. Hence, it is important to apply 3D ECM culture in microfluidics for re-capitulating tumor microenvironment.

Due to the genomic and epi-genomic instability of tumor, cancer cells are notorious for its heterogeneity. Among various sub-populations, cancer stem-like cells (CSCs), which play critical roles in cancer metastasis, therapeutic resistance, and relapse, are important clinical targets [9-12]. As stem-like cell, CSC is capable of either self-renew (symmetric division) to generate CSCs or differentiate (asymmetric division) to make differentiated cancer cells [13]. Considerable evidence suggests that the symmetric division of CSC is critical for the progression of tumor, while skewing toward asymmetric division can lead to tumor suppression [14-15]. Though it is believed that 3D culture environment is favorable for stem-like phenotype, it is not clear whether this is caused by

(1) reduced asymmetric division, (2) increased symmetric division, or (3) better survival of stem-like cells [16-17]. In addition, CSC are typically more resistant to chemotherapies, yet it is not clear whether the self-renewing CSCs has stronger resistance compared to differentiating CSCs [18-19]. Using conventional dish-based approach, only the final cell number and gene expression (or Live/Dead) can be counted by fluorescence-activated cell sorting (FACS). The averaged end-point results provide little insight into the cellular heterogeneity of CSCs, nor the process of how the population is skewed. To decipher the changes of CSC populations in different conditions and treatments, there is a need for single cell analysis to monitor the fates of each individual cells.

Due to the benefits of small sample volumes, precise fluid control, and high-throughput scaling, microfluidic technology has emerged as a state-of-the-art approach for single cell analyses [20-24]. There are a number of previous works reporting on microfluidic platforms for 3D cell culture, but many of them use the suspension culture with hydrogel, which cannot emulate the cell-ECM interactions in-vivo [25-27]. To incorporate 3D ECM in microfluidics, some works control the hydrogel matrix using laminar flow [28], surface tension (achieved using micropillars) [29], and physical confinements [30-31], but these works cannot achieve precise spatial control for performing single cell assay. Hydrogel droplet formation [32-33] and 3D bioprinting [34] encapsulating single cells have merits in high-throughput and precise micro-environment control. However, limited biomaterials can be used for these technologies, making it difficult to study a wide range of different ECMs, which have distinct biochemical properties. In addition, the shear force induced by inkjet printing can compromise the cell viability. Though filling hydrogel with cells in the microwells can be one simple alternative [35], exposed microwells can easily suffer from media evaporation, which increases osmolality and thus affect cell viability. Also, cells will be inevitably washed away when exchanging media on microwells. To reliably culture single cells

in 3D hydrogel for cellular heterogeneity study, we developed a gel-island chip, which attains (1) reliable single cell encapsulation in hydrogel-based 3D culture, (2) high-throughput assay of hundreds of single cells, (3) automatic single cell monitoring for cellular heterogeneity characterization, and (4) efficient use of ECMs and reagents.

2.2 Design of gel-island chip

The microfluidics gel-island chip consists of 1500 individual culture chambers (150 $\mu\text{m}\times 150\ \mu\text{m}$, with 100 μm in height) (Fig. 2-1 (a)). All the culture chambers are aligned in series and connected to a main microfluidics perfusion channel (200 μm wide) by a narrow channel of 150 μm length and 40 μm width. A separate channel is designed in parallel with main channel for applying vacuum, with the separation of 50 μm -thick PDMS sidewall between culture chambers and vacuum channel (Fig. 2-1 (b)). The whole microfluidics chip is divided into 3 subunits with 500 culture chambers in each. These three subunits share a joint vacuum channel, so that the loading process for the whole chip can be performed simultaneously.

The gel-island chip is composed of one layer of PDMS (polydimethylsiloxane), which was fabricated on a silicon substrate by standard soft lithography, and a glass slide. Each microfluidic chip contains 1500 chambers with 2.25 nL (150 $\mu\text{m}\times 150\ \mu\text{m}\times 100\ \mu\text{m}$) volume capacities. The main channel was designed as 200 μm in width to ensure sufficient culture media or drug supply near the entrance of each chambers. One mask was used to fabricate the 100 μm thick SU8 (Microchem) for the microfluidic channel. The 40 grams of PDMS was cured by 100 $^{\circ}\text{C}$ for 1 day and then peeled off from the master. After punching the inlet and outlet using 0.6mm diameter

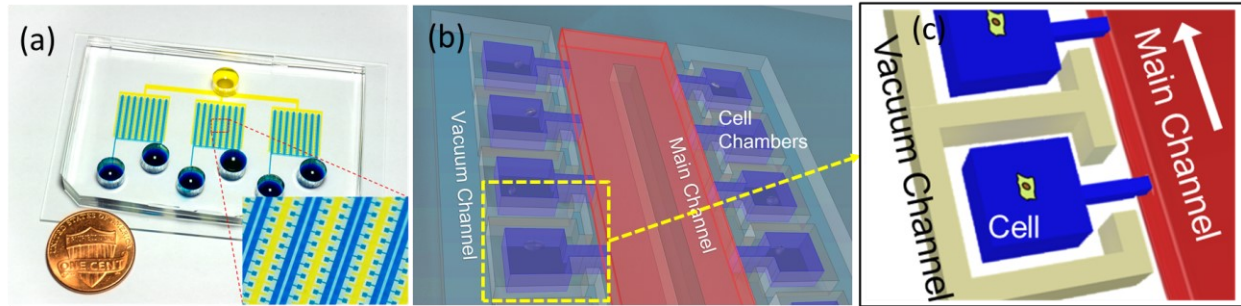


Figure 2-1. Overview of the gel-island chip design. (a) Photograph of a fabricated device. (b) Schematic of the gel-island chip. (c) schematics of single cells isolated in culture chambers.

biopsy punch, the PDMS layer activated by oxygen plasma treatment (80 Watts, 60 seconds) was bonded to the glass slide. The bonded device was placed on the hot plate of 80 °C for 5 minutes to enhance the bonding strength.

2.3 Single cell loading and cell culture

In order to study single cell behavior in 3D ECM microenvironment that recapitulate the in-vivo environment, we developed a loading scheme to form isolated collagen islands while enabling perfusion media exchange. Due to the surface tension effect, initially the main channel of the device is completely filled with fluids, leaving the air trapped inside the chambers (Fig. 2-2 (a)). Then, vacuum is applied to the vacuum channel next to the chambers (Fig. 2-2 (b)). Due to the high gas-permeability of the Polydimethylsiloxane (PDMS) sidewall, air in chambers can diffuse through PDMS into the vacuum channel gradually and drive the gel solution into the chamber. After applying vacuum for 100 seconds, the air in chambers is completely replaced by gel solutions and single cells are captured (Fig. 2-2 (c)). The flow resistance from main channel to

the chamber is designed to be two orders of magnitude higher than the flow resistance in main channel. According to Hagen-Poiseuille equation, when pumping air into the main channel, the gel solution in main channels can be purged, while the collagen solution in the culture chambers remains (Fig. 2-2 (d)). Thus, isolated collagen gel islands are formed, and the cell culture media can be exchanged through the main channel for long-term cell culture. Since the distribution of cells per chamber should follow Poisson distribution, the maximized number of single-cell islands can be achieved when loading the same cell number as the total number of the chambers. Using optimized loading density, 34% of the 1500 chambers are loaded with single cells (Fig. 2-2 (e, f)).

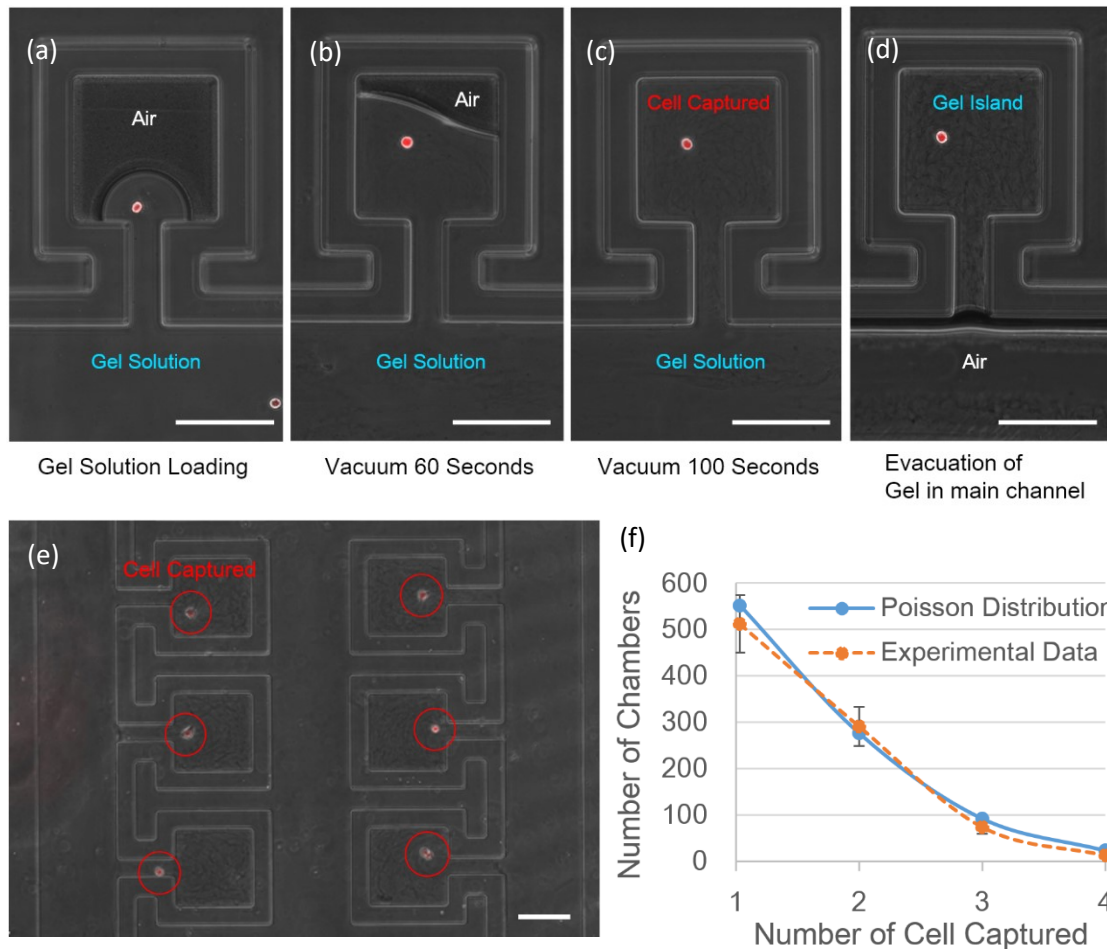


Figure 2-2. Gel-island loading process with single cell encapsulation. (a) Loading the cell solution into the main channel. (b) Gel solution partially fills culture chamber after 60 seconds of applying vacuum. (c) Gel solution fully occupied the whole chamber

after 100 seconds of applying vacuum, with a single cell captured. (d) The gel solution in main channel was evacuated by pumping air. (e) Gel-island device loaded with MDA231 breast cancer cells. (f) Distribution of the number of captured cancer cells per chamber when loading 1500 cells into each device (N=3). (Scale bar: 100 μ m)

Since the collagen gel in main channel was evacuated by air flow, we were able to load culture media into main channel and supply nutrient to cells in chambers via diffusion. To characterize the diffusion rate of nutrient molecules, we created collagen islands using the method described in previous section and then flowed dextran conjugated fluorescein (MW = 40k) in main channel to mimic large protein molecules diffusing into culture chambers (Fig. 2-3 (a)). By comparing the fluorescent intensity between culture chambers and main channel, we verified that it takes less than 2 hours for fluorescein concentration in the chambers to reach 80% of that in the main channel, and around 4 hours to reach 90% (Fig. 2-3 (b)). In addition, we demonstrated that the fluorescent intensity difference between chambers at upstream and downstream was less than 10% (Fig. 2-3 (c)), indicating uniform media supply in the whole device. In order to make sure the location of the encapsulated cells does not lead to large variance in mass transfer, we also verified

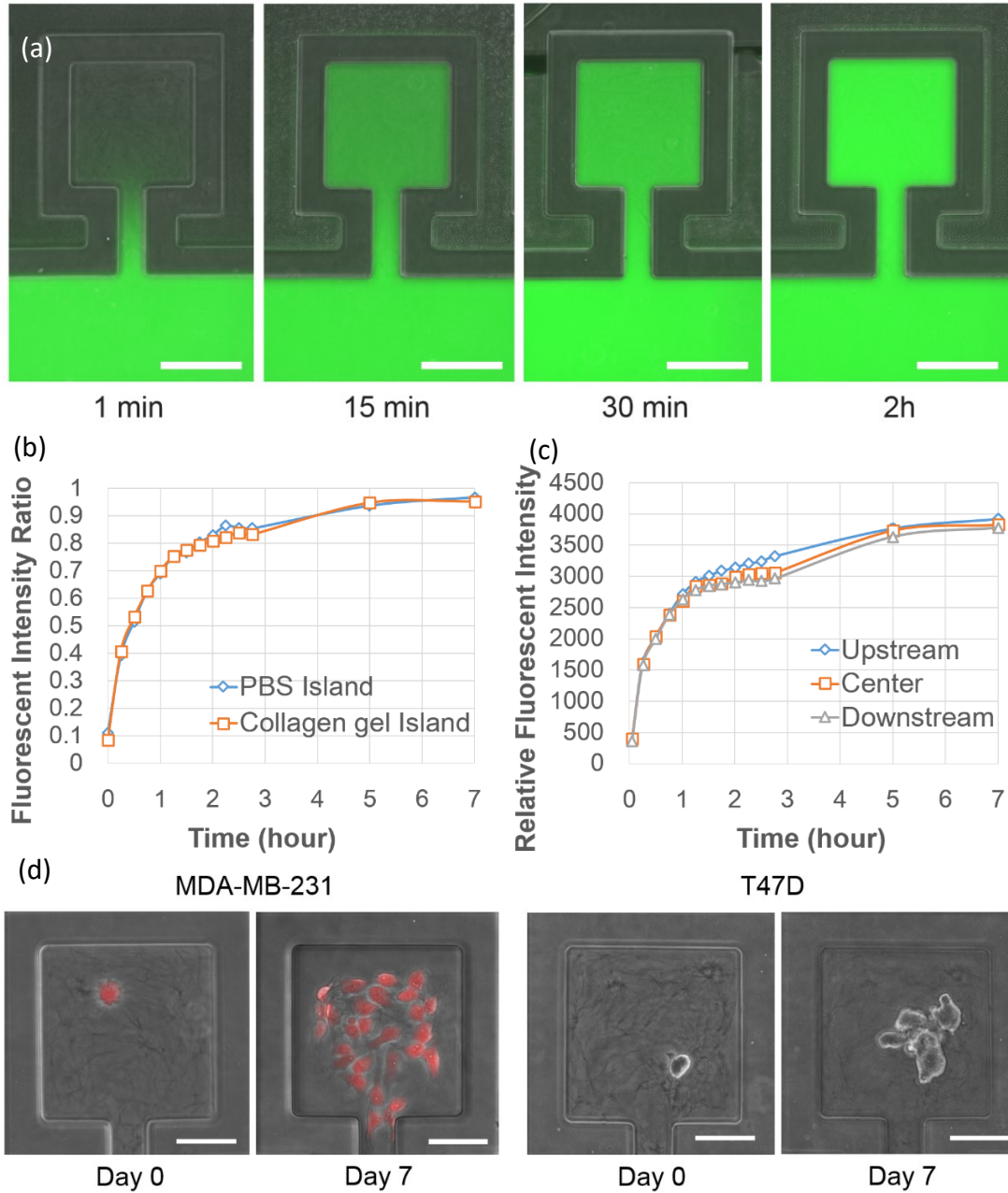


Figure 2-3. Long-term cell culture capability. (a) Device view of dextran conjugated fluorescein (Molecular weight = 40k) diffusion test at 1 minute, 15 minutes, 30 minutes and 2 hours. Fluorescein solution was loaded in main channel and diffused in collagen islands. (Scale bar: 100 μm) (b) Ratio of mean fluorescent intensity of chambers to mean fluorescent intensity of nearby main channel vs. time. (N=5) (c) Relative fluorescent intensity in chambers at the upstream, center, and downstream of the device (N=5) (d) On-chip cell culture of MDA-MB-231 and T47D breast cancer cells for 7 days. (Scale bar: 50 μm)

conformal biomolecule distribution inside culture chambers (Fig. 2-4). The diffusion experiments suggest good media exchange capability for cell culture. To further demonstrate the long-term cell culture capability of the reported microfluidics platform, we loaded the MDA-MB-231 and T47D (breast cancer) cells into the island chip and cultured for 7 days. As shown in Fig. 2-3 (d), single cell derived colonies were formed in the culture chambers. The size of the on-chip colony was comparable with the bulk collagen gel culture control (Fig. 2-5). Using the isolated gel-islands, we were able to track individual single cell proliferation and differentiation behaviors in the 3D environment, providing insights about cellular heterogeneity.

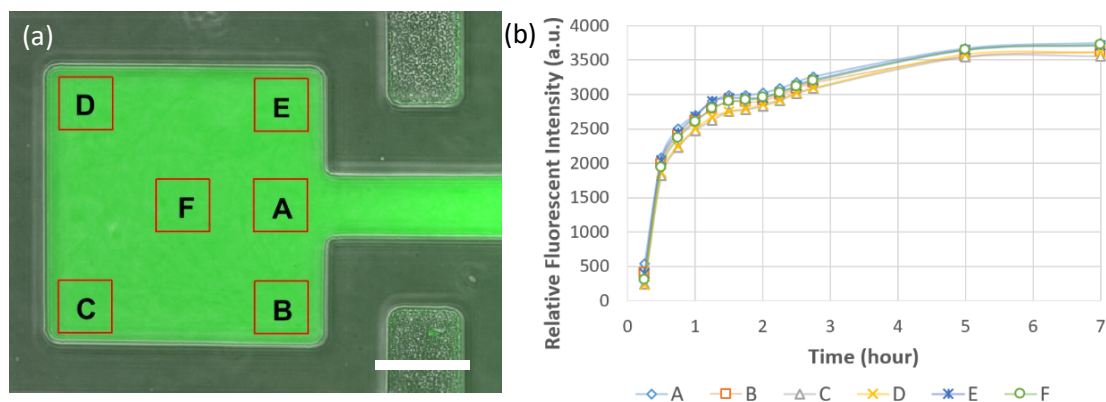


Figure 2-4. Diffusion test using dextran-conjugated fluorescein to verify conformal mass transfer inside culture chambers: (a) measurement of relative fluorescent intensity at six different region inside culture chambers, (b) Relative fluorescent intensity changes in six different regions inside culture chambers (N=5). (Scale bar: 50 μ m)

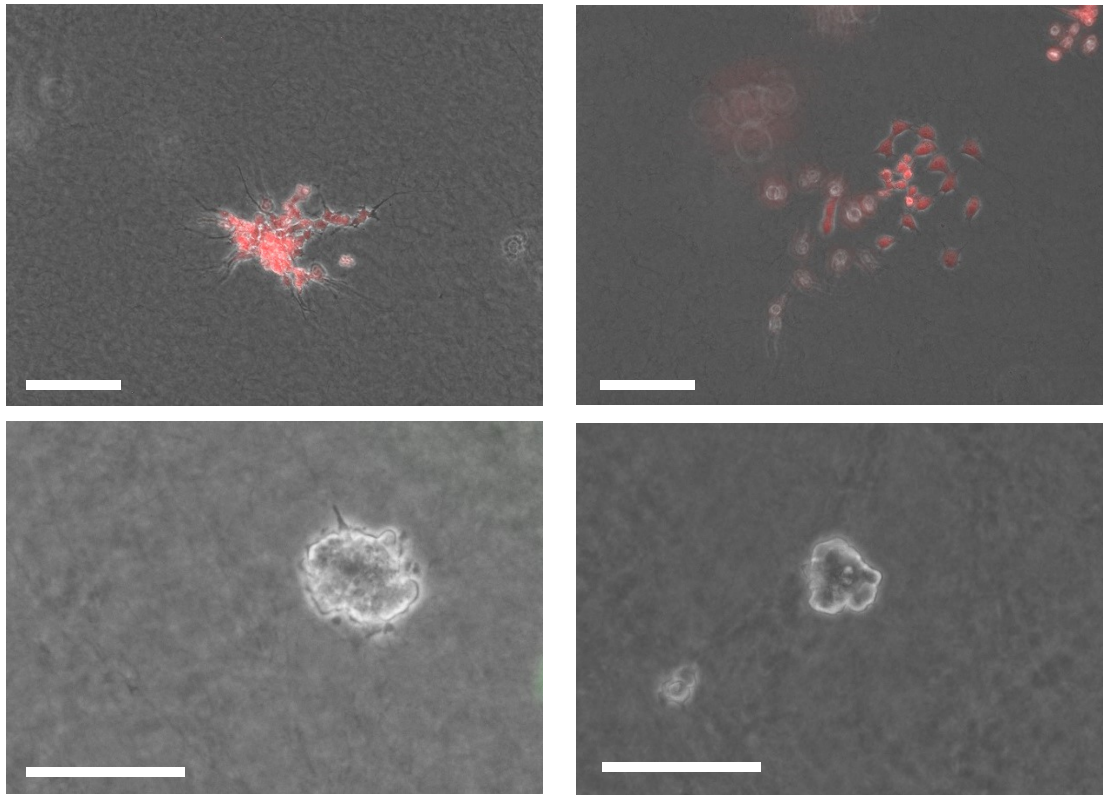


Figure 2-5. MDA-MB-231 and T47D breast cancer cells cultured in conventional petri-dish for 7 days: (a) MDA-MB-231. (b) MDA-MB-231. (c) T47D bulk. (d) T47D bulk. (Scale bar: 100 μm)

2.4 Cancer cell differentiation study

Using Notch reporter system [35], Notch activity of each individual cell was determined by its GFP expression (fluorescent brightness). To study cell proliferation and differentiation behaviors in single cells resolution, T47D cells were loaded with collagen gel at a concentration of 2mg/mL or regular culture media (2D control) into different devices (Fig. 2-6 (a)). The cells loaded with collagen gel solution will be cultured in gel-island, while the ones loaded with media will be in the 2D culture environment. After 2 days culture, although 2D control group had higher percentage of proliferating cells, compared to the 3D environment, more Notch+ cells

differentiated to Notch- in the 2D environment when normalizing to the total number of proliferation events (Fig. 2-6 (b)). In addition to the Notch+ cells, when characterizing the cell fate

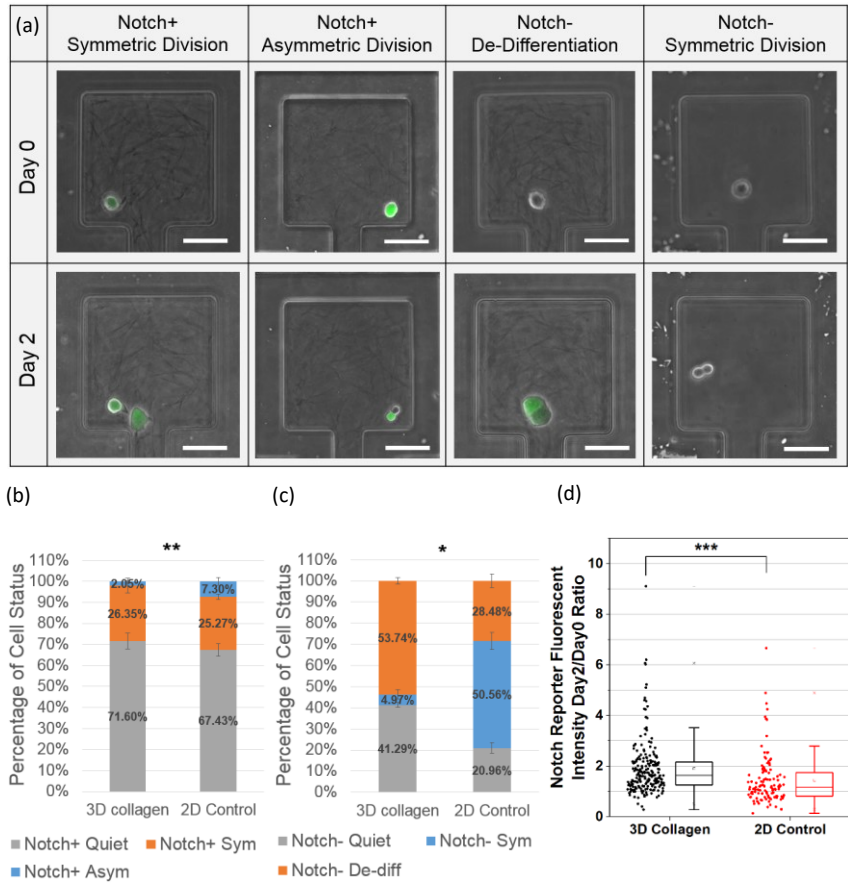


Figure 2-6. T47D breast cancer cell differentiation: (a) Examples of different cell status after culturing on chip for 2 days. (b) T47D Notch+ cell status. (c) T47D Notch- cell status. The data samples used in significance test of (b) and (c) are the ratio of Notch+ symmetric division population percentage to Notch+ asymmetric division population percentage in 3D collagen culture conditions vs. that in 2D Control culture conditions. (d) Distribution of Notch reporter gene fluorescent intensity ratio between 48h (day2) and 6h (day0) after cell loading under 2 culture conditions: 3D collagen gels (black, N=209), and 2D culture media (red, N=116). * refers to $P < 0.05$, ** refers to $P < 0.01$, *** refers to $P < 0.001$, NS refers to not significant. (Scale bar: 50 μm)

for Notch- population, we observed significantly more Notch- to Notch+ transition cases in 3D collagen condition than in 2D condition (Fig. 2-6 (c)). Using conventional approach, people cannot identify the process of skewing of the population. With the help of the presented platform, we

found that the skewing toward stem-like morphology was caused by both maintaining self-renewal potentials and de-differentiation (Notch- to Notch+ transition). In addition to the binary separation of Notch+ and Notch- cells, we tracked the Notch expression of each individual cells by its GFP intensity. GFP fluorescent intensity of each individual cells were measured 6 hours and 48 hours after cell loading (Fig. 2-7). As shown in Fig. 2-6 (d), the Notch expression of cells were elevated in the 3D culture environment compared to 2D culture. This data also supports that 3D collagen condition enhances the expression of Notch signaling pathways.

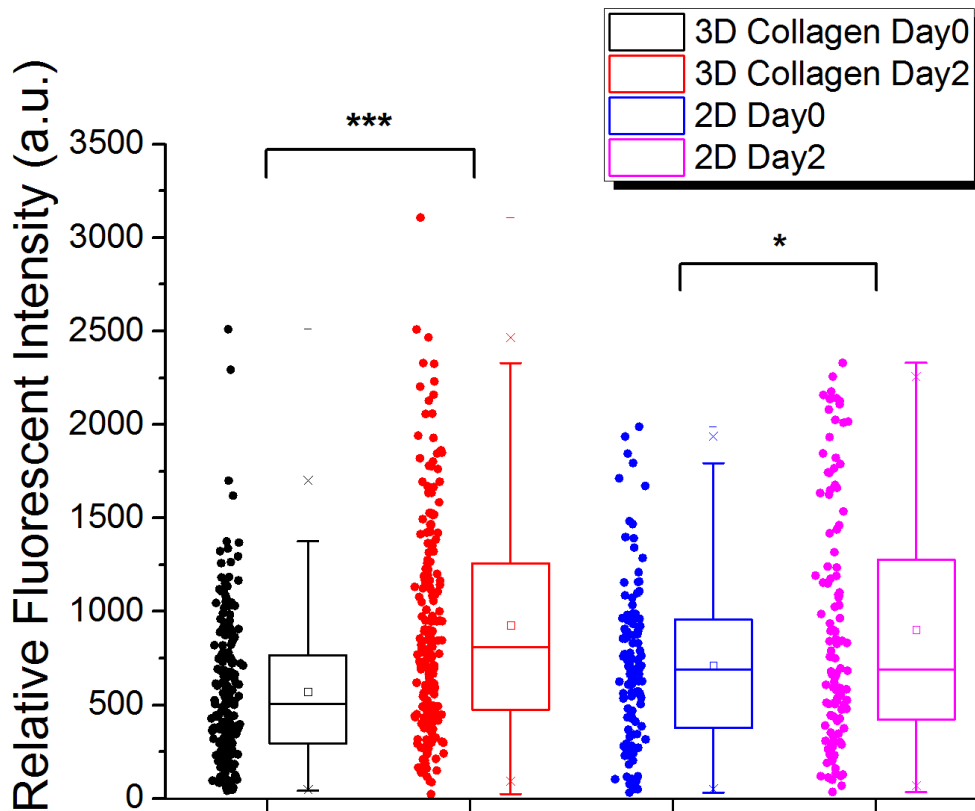


Figure 2-7. Distribution of Notch reporter gene fluorescent intensity ratio between 48h (day2) and 6h (day0) after cell loading under 2 culture conditions: 3D collagen gels (black, N=209), and 2D culture media (red, N=116). * refers to $P < 0.05$, *** refers to $P < 0.001$.

2.5 Cancer drug susceptibility test

Conventionally, people use 96-well or 384-well plates for drug screening, and the results are measured by MTT-based colorimetric analysis or Live/Dead cell counting using flow cytometry. Though this approach has been used for decades and are still prevailing, these conventional assays provide limited insight about cellular heterogeneity. Though CSC can be sorted based on the markers, the differentiation and state transition can happen before or during the drug treatment. More importantly, it is almost impossible to distinguish CSC derived from self-renewal or de-differentiation using dish-based approach. To precisely correlate the cell states and drug efficacy, the states of each single cells should be tracked before and after the drug treatment. Here, we categorize the cells into 6 different states: symmetrically divided Notch+ cell, asymmetrically divided Notch+ cell, quiescent Notch+ cell, de-differentiated Notch- cell, symmetrically divided Notch- cell, and Notch- quiescent cell. Using the gel-island chip, the drug (doxorubicin, cisplatin) efficacy of each type of cell state was characterized (Fig. 2-8 (a)).

Firstly, using the single cell monitoring capability of gel-island chip, we noticed the Notch+ cells were less sensitive to chemo-drug than Notch- cells (Fig. 2-8 (b)). The observation match well with the expectation that Notch pathways correlate with cell stemness and drug resistance [37][38]. Secondly, among the proliferating cells, symmetrically divided Notch+ cells were found to be more resistant than asymmetrically divided ones (Fig. 2-8 (c)). Again, the difference can be explained by the higher stemness of the self-renewing cells than that of the differentiating cells. More interestingly, Notch- de-differentiated cells, which underwent Notch- to Notch+ transition, showed significantly higher drug resistance than all other cell states, indicating that the de-differentiating cells can be a major contributor of drug resistance. The similar drug response pattern was observed in the two drug we tested. This result suggests that the drug response of

cancer cells is not only determined by the cell status at a single static time point but also the process of cell proliferation, differentiation, and de-differentiation. Hence, it is importance to use single-cell tools to track individual cell behavior for understanding the heterogeneous cell responses to cancer drugs.

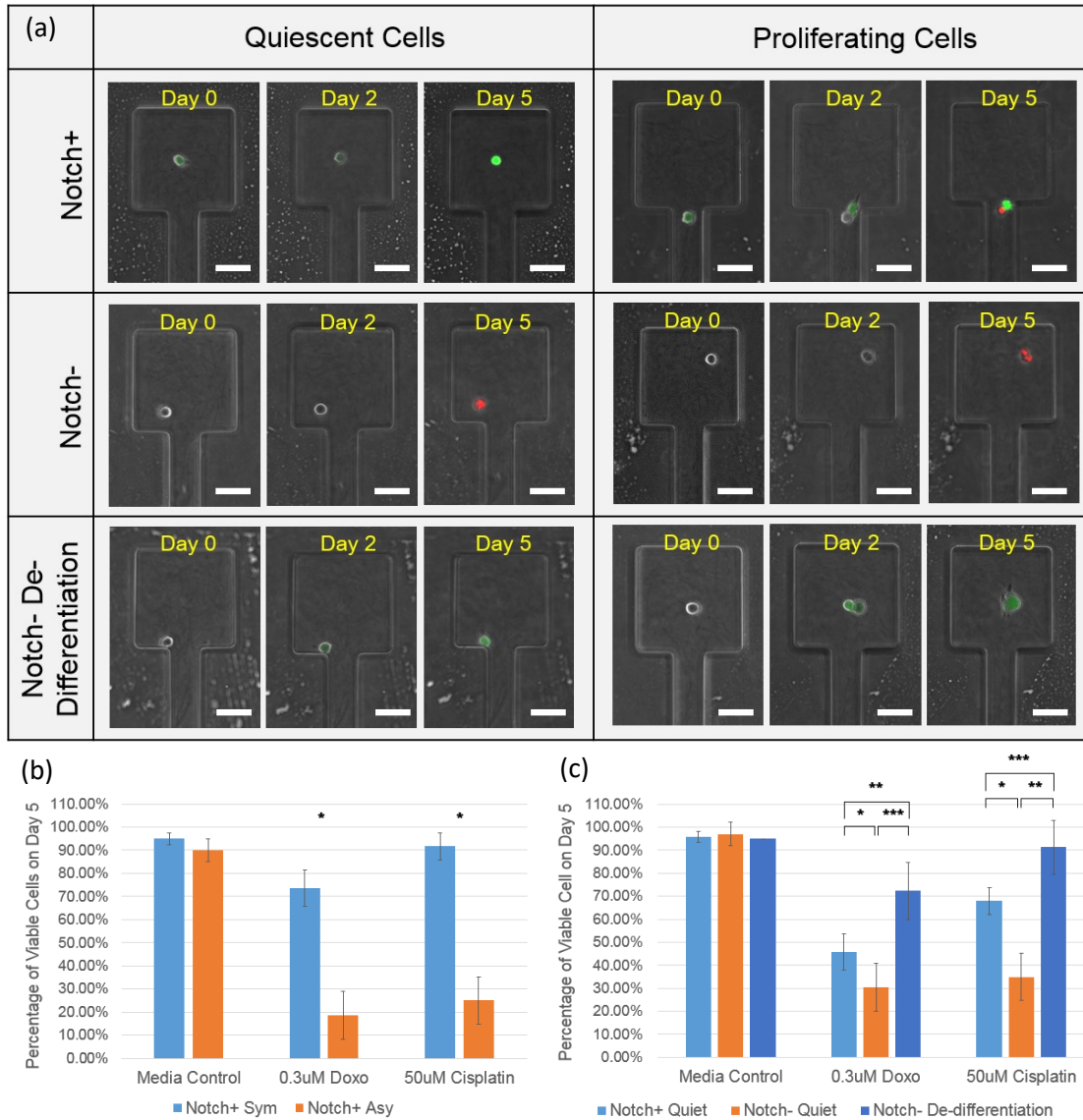


Figure 2-8. Drug susceptibility test of T47D Notch+ breast cancer cells under 2mg/mL 3D collagen gel condition, cultured on chip for 48 hours followed by 72 hours drug treatment: (a) Examples of cell status its drug response (the green fluorescence in day0 and day2 images is from GFP, the green/red fluorescence in day5 is from Live/Dead dye). (b) Drug susceptibility

comparison between symmetrically divided Notch+ cells (blue, N=3) and asymmetrically divided Notch+ cells (orange, N=3).
(c) Drug susceptibility comparison between 3 types of non-proliferating cells: Notch+ quiescent cells (light blue, N=3), Notch- quiescent cells (orange, N=3), and Notch- de-differentiation cells (dark blue, N=3). * refers to $P < 0.05$, ** refers to $P < 0.01$, and *** refers to $P < 0.001$. (Scale bar: 50 μm)

2.6 Chapter summary

We reported a gel-island chip combining single cells resolution and 3D ECM cell culture environment. By simply applying vacuum, single cells can be loaded into the islands with gel solution. Then, the gel in the main channel is evacuated by pumping air, thus forming isolated gel-islands. Using optimized cell concentration, the single cell capture rate can reach 34% based on Poisson's distribution. Good media exchange rate into the islands, as well as upstream and downstream uniformity were demonstrated. We also showed that cells cultured in the gel islands for 7 days maintained high viability. Using this platform, we monitored the symmetric and asymmetric division of the Notch+ (stem-like) T47D breast cancer cells. Compared to conventional approach, which only allows people to observe the cells skewing to stem-like morphology in 3D culture without identifying the process in single cell resolution. Utilizing the presented platform, we found that the skewing was caused by both the increased self-renewal of stem-like cells and the de-differentiation of Notch- (non-stem-like) cells. In addition, we performed the drug testing of doxorubicin and cisplatin to compare the different fates of individual Notch+ and Notch- cells. As expected, Notch+ cells were more resistant than Notch- cells. Interestingly, we found that de-differentiated (Notch- to Notch+) cells were significantly more drug resistant than Notch+ cells, demonstrating that the drug efficacy can be correlated with the

state change of cells. The finding suggests the importance of monitoring single cells in 3D ECM environment, which was previously not possible using conventional approaches.

Chapter 3 : Scalable Multiplexed Drug-Combination Screening Platforms Using 3D Microtumor Model for Precision Medicine

Cancer heterogeneity is a notorious hallmark of this disease, and it is desirable to tailor effective treatments for each individual patient. Drug combinations have been widely accepted in cancer treatment for better therapeutic efficacy as compared to single compound. However, experimental complexity and cost grow exponentially with more target compounds under investigation. The primary challenge remains to efficiently perform a large-scale drug combination screening using a small number of patient primary samples for testing. Here, we report a scalable, easy-to-use, high-throughput drug combination screening scheme, which has the potential of screening all possible pairwise drug combinations for arbitrary number of drugs with multiple logarithmic mixing ratios. We introduced a “Christmas tree mixer” structure to generate a logarithmic concentration mixing ratio between drug pairs, providing a large drug concentration range for screening. A three-layer structure design and special inlets arrangement facilitate simple drug loading process. As a proof of concept, we implemented an 8-drug combination chip, which is capable of screening 172 different treatment conditions over 1,032 3D cancer spheroids on a single chip. Using both cancer cell lines and patient-derived cancer cells, we demonstrated effective drug combination screening for precision medicine.

3.1 Introduction

In recent decades, considerable efforts have been made in precision cancer therapy, which aims to customize appropriate treatment decisions based on individual cases [1]. Though advances in DNA profiling and next-generation sequencing (NGS) have identified thousands of mutations that are critical to cancer progression [2, 3], this genotypic method does not always pinpoint ideal cancer therapeutics due to the limited biological understanding [4]. In addition, the presence of non-DNA genetic variations, including epigenetic modifications, lineage-specific changes and tumor micro-environment modulations [6] could make it even more complicated to correlate cancer cell genetic information with clinical consequences [7, 8]. These drawbacks can be addressed by empirical phenotypic drug testing [9, 10], in which patient cancer cells are exposed to multiple treatments in vitro as a therapeutic guidance for individual patients [11].

As compared to mono-drug treatment, drug combination has emerged as treatments for many diseases [12], especially for cancer due to its difficulty in treatment and cellular heterogeneity [13]. Although many new cancer drugs have been developed, mono-drug treatments typically fail curing cancer [14] due to the existence of alternative pathways to compensate the pathway target of drug [15, 16]. In order to overcome the limitations of mono-drug therapies, drug combinations, which aim to inhibit multiple redundant pathways of tumor cells, [17] have been widely accepted for better therapeutic efficacy [18]. To identify appropriate drug combinations, it is desirable to include more compound candidates [19], yet the resulting experimental complexity and cost increases exponentially [20]. For example, investigation of 50 different compounds in pairwise combination yields ${}_{50}C_2 = 1225$ different combinations. Furthermore, we assume 7 different concentration ratios for each combination, and 6 replicates for each treatment condition,

which yields $1225 \times 7 \times 6 \times 10 = 51450$ experiments. This is not only costly but also time-consuming for a typical test panel of well-plate platforms.

In 2013, The US Food and Drug Administration expressed their dedication in developing novel combinatorial therapies, highlighting the need for innovative technologies to accelerate the discovery of novel drug combinations [22, 23]. To achieve high-throughput drug combination screening, several systems have been presented incorporating robotics and automatic handling [24]. However, they are limited by complicated operation systems [25] and time-consuming serial processes [26]. Microfluidics emerges as a promising technology for both clinical precision medicine and industrial-scale drug discovery [27], thanks to its capability of handling small samples and highly multiplexed operations for high-throughput assays [28]. Previous microfluidic high-throughput drug screening platforms introduce a “Christmas tree structure” to generate a linear drug concentration gradient, but they are limited to the combination of two drugs [29, 30], which may not meet the needs for high-throughput drug screening. In addition, since cells respond to different drug concentrations in a non-linear manner, in some cases drug screening experiments require testing dosages ranging several orders of magnitude to calculate the 50% inhibition concentration (IC₅₀) [31]. The narrow concentration range provided by conventional microfluidic linear gradient generators severely limits the use of microfluidics in drug screening [32]. Previous work using microfluidic generating logarithmic concentration gradient requires complicated valve operation and interface system, which is not desirable for routine drug screening application [33].

Furthermore, conventional in vitro cancer drug screening was mostly performed on two-dimensional (2D) well-plates as a simple, fast, and cost-effective tool [34]. However, accumulating evidence on in vitro cancer studies shows that a large number of cellular features and gene expression are skewed in a 2D culture environment [35], which makes it less reliable to make

accurate clinical decisions. Three-dimensional (3D) cell culture systems have been widely used as better models in mimicking the in vivo tumor microenvironment [36], and it has become increasingly popular in drug screening studies [37]. In this work, we report a scalable, easy-to-handle, high-throughput drug combination screening scheme, incorporated with custom software for drug efficacy readout and data analysis. The presented microfluidic design enables screening of all possible pairwise drug combinations from arbitrary number of different drugs. As a proof of concept, we demonstrated an 8-drug screening chip with logarithmic concentration gradient. We performed drug combination screening experiment with multiple cell lines. Combining ${}_8C_2 = 28$ drug combinations, 6 mixing ratios, and 6 replicates, plus some single compound control chambers, a total of 1,032 drug efficacy screening experiments can be accomplished in a single 8-drug screening chip. Using the presented chip, we successfully performed drug combination screening of pancreatic cancer patient-derived cell lines, as a demonstration for precision medicine applications.

3.2 Microfluidic filter structure for cell capture and sphere formation

The proposed drug combination screening chip consists of 1032 microtumor culture units, (28 drug combinations \times 7 concentration mixing ratios + 4 culture media controls) \times 6 replicates = 1032. Cells loaded to the chip will be automatically distributed to all the culture chambers to form microtumors. To facilitate cell capturing and microtumor culturing, each culture unit is composed of a center sphere culture chamber, a ring chamber surrounding the center sphere culture chamber, and a thin gap (5 μm in height, 50 μm in length) connecting the two chambers. A total of 20 octagon micropillars (5 μm in height, 25 μm in side length, and 25 μm in spacing between

pillars) are sparsely deployed between the polydimethylsiloxane (PDMS) thin gap to provide mechanical support and prevent the thin gap from collapsing (Fig. 3-1 (a)).

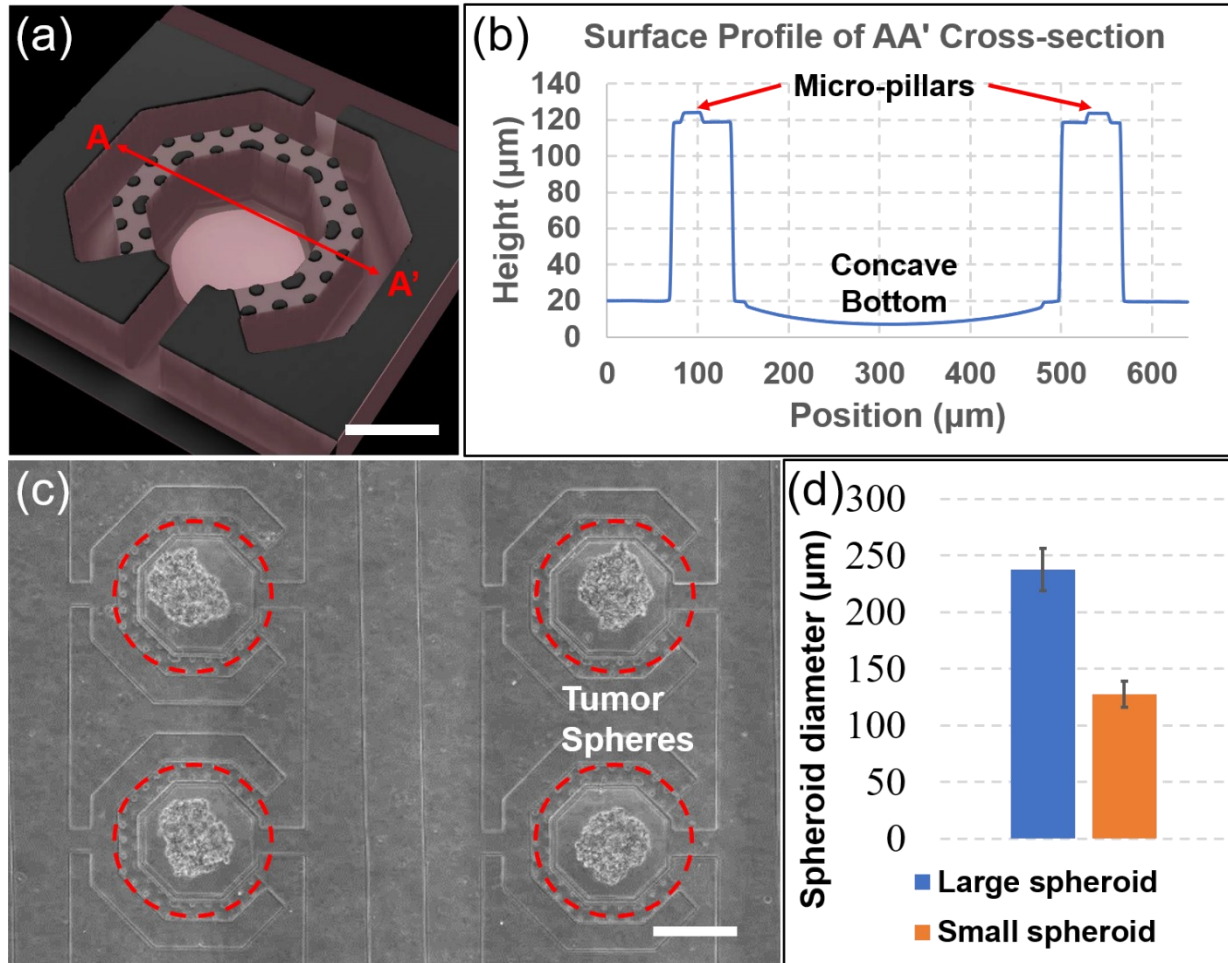


Figure 3-1. Schematics of multiplexed 8-drug combination screening chip. (a) Separate views of three PDMS layers. 32 holes are punched through all the three PDMS layers for drug inlets using 6mm biopsy punch, connecting the mixing and routing layers. (b) Top view of the mixing layer: 32 inlets are allocated to 8 drugs, with a group of 4 connecting to each other with the same number in the routing layer. Before drug treatment, cells were loaded to the inlets and automatically deployed to 1,032 culture chambers driven by gravity flow. Cell inlets are also used for drug outlet during drug treatment process. (c) Top view of the routing layer, same number on different rows are connected in routing layer.

3.3 Microfluidic tree structure as logarithmic concentration gradient generator

We presented a “Christmas tree mixer” structure with non-uniform channels sizes to achieve a logarithmic mixing ratio gradient between two different compounds. The “Christmas tree mixer” is composed of five stages of microfluidic meander channels, with an incremental number from three to seven in each stage (Fig. 3-2 (a)). Solutions containing two different compounds are introduced from the top inlets and flow through the microchannel network. The fluid streams are combined in each branch channel stage, yielding mixture of distinct compositions, and splitting to the next stage. Finally, a concentration gradient is generated across the last stage of branching channels [29]. The splitting ratio of the flow at each stage is determined by the flow resistance. According to Hagen-Poiseuille equation, hydraulic resistance of a channel is approximately inversely proportional to squared channel width [44]. When all the microfluidic meander channels are designed to be of the same size (width, height, length), the flow resistance through all the branch channels are the same. In this case, a linear concentration gradient with an arithmetic progression ratio will be established in the last stage.

However, most drug screening experiments require log-scale concentration gradient covering a wider concentration range. In order to generate non-linear concentration gradient, channels on both two sides are designed to be wider than those at the center, so that the flow resistance of meander channels on the sides are smaller than that of the channels at the center. For example, two drug compounds, A and B, are loaded on the two sides of the mixer (Fig. 3-2 (a)). Due to a small flow resistance inside channels compared to center channels, mostly of the flow will be guided side channels, while only a small portion mixed with each other at the center meander channels. In this case, when the mixture from the previous stage flowing to the next stage, a large volume of compound A from the channels on the left merged with the small volume of

mixture compound A+B from the center channel, yielding a mixture containing mostly A with a small portion of B. The more drastically different the volumes are, the less amount of compound B is contained in the final mixture, the larger concentration ratio of compound A to compound B is. In this manner, we can generate a logarithmic concentration gradient (Fig. 3-2 (b)).

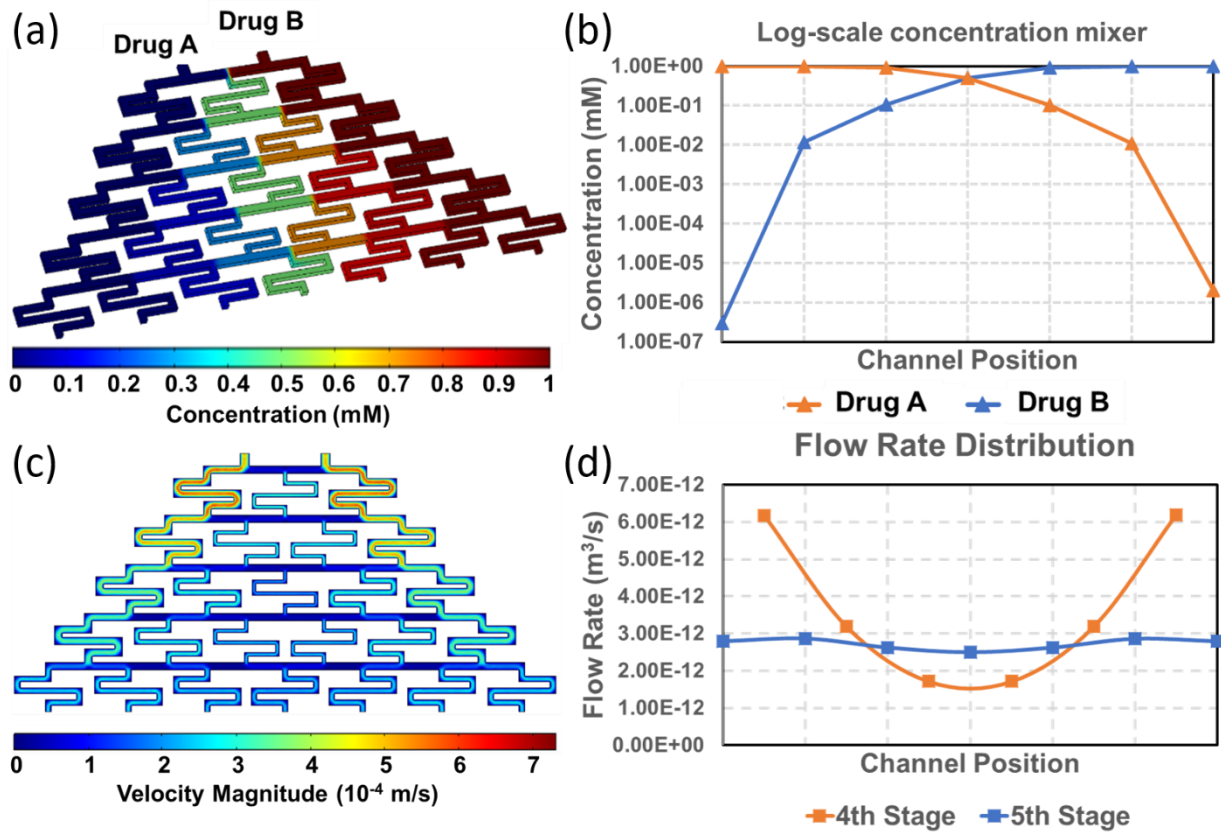


Figure 3-2. COMSOL simulation results for logarithmic "Christmas tree mixer" structure (a) Concentration simulation of "Christmas tree mixer" using COMSOL. (b) Measurement of the concentration of both drug A and drug B at the final stage of the mixer. (c) Velocity simulation of "Christmas tree mixer" using COMSOL. (d) Flow rate measurement of the channels in 4th stage and 5th stage (last stage), validating that the last stage can be a "buffering layer" to balance the flow rates among between branches.

Another critical design of this chip is that meander channels at the last stage (i.e. 5th stage) of mixer array have the same dimension, instead of following the previously described rule of “side channels wider than center channels”. This last stage meander channels are used as a “buffering layer” between the upstream “Christmas tree mixer” and downstream sphere culture chambers (Fig. 3-2 (c)). The rationale behind this last stage meander channel design is that the sphere culture chambers connected to the downstream also contributes to the equivalent resistance of the last stage of the “Christmas tree mixer”. Even if the channel dimension of the last stage is carefully designed, because of the contributions of the hydraulic resistance from the downstream microfluidic structure, the equivalent resistance seen from the previous stage will be affected. On the other hand, the “Christmas tree mixer” also have an influence on the flow resistance of cell capture structures. When cells are loaded from cell inlets to cell culture chambers, the imbalanced channel design of “Christmas tree mixer” will also affect the cell loading uniformity, resulting in more cells loaded to chambers that are connected to side channels due to a lower flow resistance. Channels of the same dimension at the last stage of “Christmas tree mixer” help balance the cell loading (Fig. 3-2 (d)) and form tumor spheres of uniform size among all branches (Fig. 3-3).

We demonstrate the COMSOL simulation results of the presented mixer structure (Fig. 3-2 (a)), in which the channel dimension is designed to be symmetric. As described above, the channels at the last stage are the same in dimension (90 μm in width). To achieve the proper range of mixing ratios, the center channels are designed to be 60 μm in width, the channels on both sides are 120 μm in width, while the channels in between are 90 μm in width. As a result, seven concentration ratios between drug A and drug B are achieved at a logarithmic gradient, ranging in 1:10⁶, 1:100, 1:10, 1:1, 10:1, 100:1, and 10⁶:1 (Fig. 3-2 (b)), which is desirably wide for drug screening platforms.

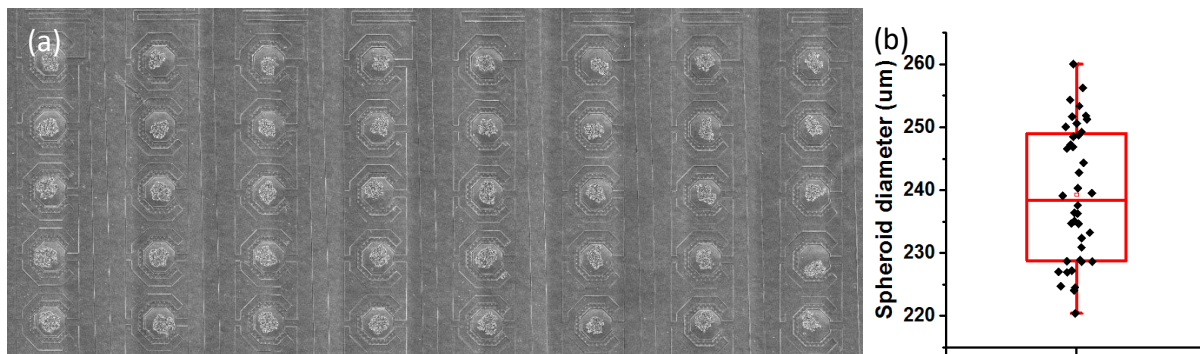


Figure 3-3. Formation of uniform spheres. (a) A microscope view containing 40 SUM159 spheroids showing uniform spheroids size. (b) Scattering plot showing a small variation of < 4.4% in the diameter size. (Scale bar = 300 μm)

3.4 Mixer array and drug inlets “Sudoku puzzle”

By deploying the “Christmas tree mixer” structures, we could generate a concentration gradient between two drugs. However, if all the ${}^8C_2 = 28$ combinations of 8 drugs need to be screened using “Christmas tree mixer” side by side, at least $28 \times 2 = 56$ drug inlets are, which requires a very complicated microfluidic interface tubing system. To address this issue, adjacent Christmas tree mixers are designed to share a common drug inlet. However, this design requires special arrangement of the inlet array to guarantee the adjacent drug pairs cover all the possible combinations. For example, we could arrange the drug inlets as table 3-1 if there are 4 drugs:

Table 3-1. Example drug inlets layout for 4 drugs. Number 1, 2, 3, 4 stands for 4 different drugs.

1	2	3	4
2	4	1	3

In which, number 1~4 stand for 4 different drugs, and there is a “Christmas tree mixer” between each number pairs to generate concentration gradient. In this case, all the possible pairwise combinations, 1-2, 2-3, 3-4, 1-3, 2-4, and 1-4 are covered. However, the arrangement problem becomes much more complicated when the drug number becomes larger, for example, the computational complexity could reach 10^{26} possible permutations when the drug number comes to 16. To make it possible for scaling-up, a general solution to the inlet arrangement is require so that the same design strategy could be applied to any arbitrary number of drugs. Although there are many possible solutions that could fulfill the requirements, we find a general solution for all even number of drugs. To make it convenient to explain, we rephrase the inlets arrangement problem to the following “Sudoku puzzle” problem:

Let N be any even number, use number 1~ N to fill in a table with N columns and $N / 2$ rows. If we define the combination of horizontally adjacent numbers as a “pair”, also define “1, 2” and “2, 1” are the same pair. We will have $N \times (N - 1) / 2$ pairs in the table. Try to fill in table, such that:

(a) Each row contains N non-repeating numbers from 1 to N .

(b) All the $N \times (N-1)/2$ pairs are non-repeating and covering all the possible combinations.

Since all the requirements are defined on adjacency relationship, we find it very convenient to introduce an “adjacency relationship matrix” to keep record of the existing adjacent number. Take the adjacency matrix for $N = 6$ as example:

Table 3-2. Initialization of adjacency matrix.

	1	2	3	4	5	6
1	x					
2		x				
3			x			
4				x		
5					x	
6						x

There are $6 \times 6 = 36$ entries in this adjacency matrix. Each entry represents the existence of certain adjacent number pairs in the original Sudoku table. For example, if we put an “x” in the entry located at row2 column3, it means that the combination of “2-3” already exist in the original Sudoku table. Similarly, entry in row5 column1 means that “5-1” is covered. In this case, if all the entries in this “adjacency matrix” is filled with a “x”, its corresponding Sudoku table is a good solution. It is obvious that the diagonal entries don’t exist, so we ignore those entries.

To fill in this table, we first assume this n-by-n array should be symmetric. In this way, it is convenient to guarantee “a-b” and “b-a” appear at the same time. Also, it is easy to proof that the first row and first column are arbitrary. To make it simple, we fill in number 1~6 in original Sudoku table, together with its corresponding adjacency matrix as follows:

Table 3-3. Filling adjacency matrix at the second line next to diagonal with “a”.

1	2	3	4	5	6
2					5
3					4
4					3
5					2
6	5	4	3	2	1

	1	2	3	4	5	6
1	x	a				
2	a	x	a			
3		a	x	a		
4			a	x	a	
5				a	x	a
6					a	x

We keep filling in the entries in third line along diagonal direction.

Table 3-4. Filling adjacency matrix at the third line next to diagonal with "b".

1	2	3	4	5	6
2	4			3	5
3	1			6	4
4	6			1	3
5	3			4	2
6	5	4	3	2	1

	1	2	3	4	5	6
1	x	a	b			
2	a	x	a	b		
3	b	a	x	a	b	
4		b	a	x	a	b
5			b	a	x	a
6				b	a	x

Taking advantage of the symmetry of the table, we could derive:

Table 3-5. Filling adjacency matrix at the fourth line next to diagonal with "c".

1	2	3	4	5	6
2	4	1	6	3	5
3	1			6	4
4	6			1	3
5	3	6	1	4	2
6	5	4	3	2	1

	1	2	3	4	5	6
1	x	a	b	c		c
2	a	x	a	b		
3	b	a	x	a	b	c
4	c	b	a	x	a	b
5			b	a	x	a
6	c		c	b	a	x

Finally, we fill in the 5th line along diagonal direction, we could get the full solution to 6 by 6 adjacency Sudoku table as follows:

Table 3-6. Completion of adjacency matrix.

1	2	3	4	5	6
2	4	1	6	3	5
3	1	5	2	6	4
4	6	2	5	1	3
5	3	6	1	4	2
6	5	4	3	2	1

	1	2	3	4	5	6
1	a	a	b	c	d	c
2	a	x	a	b	e	d
3	b	a	x	a	b	c
4	c	b	a	x	a	b
5	d	e	b	a	x	a
6	c	d	c	b	a	x

In this work, due to the limitation of wafer area and availability of chemo-drugs, we only conduct experiment on devices for 4 drugs and 8 drugs. However, the introduced method using “adjacency matrix” could be applied to get any arbitrary even numbers. As a demonstration, we showed the matrix for 16 drugs (Table 3-2).

Table 3-7. Example drug inlets layout for 16 drugs. Number 1~16 stands for 16 different drugs.

1	2	3	4	5	6	7	8	9	10	11	12	13	14	15	16
2	4	1	6	3	8	5	10	7	12	9	14	11	16	13	15
3	1	5	2	7	4	9	6	11	8	13	10	15	12	16	14
4	6	2	8	1	10	3	12	5	14	7	16	9	15	11	13
5	3	7	1	9	2	11	4	13	6	15	8	16	10	14	12
6	8	4	10	2	12	1	14	3	16	5	15	7	13	9	11
7	5	9	3	11	1	13	2	15	4	16	6	14	8	12	10
8	10	6	12	4	14	2	16	1	15	3	13	5	11	7	9

3.5 Multiple PDMS layers for drug mixing and routing

As described in previous drug inlets array section, even if the inlet number could be reduced by sharing common drug inlets, there are still many inlets for each drug. For example, for a 16-drug combination screening chip, it is labor-intensive to load all the 16 drugs into $16^2/2 = 128$ drug reservoirs, especially when there are many chips to operate. In order to further minimize the pipetting/tubing number, we present a three-layer chip design inspired by multilayer circuit board design. The three PDMS layers are routing layer, mixing layer, and lid layer from bottom to top (Fig. 3-4 (a)). In the mixing layer, different drug compounds are combined using previously mentioned “Christmas tree mixers” that are patterned on it, together with sphere culture chambers (Fig. 3-4 (b)). In the routing layer, a total of N ($N =$ number of drugs to be screened) microfluidic channels are implemented to connect multiple drug reservoirs for the same drug. Through these routing channels with extremely large cross-section area, thus negligible flow resistance compared to micro-channels in the mixing layer, each drug compound can be automatically dispensed to all the drug inlets within seconds. The layout of the routing channels could be generated and optimized automatically using PADS Autorouter, a circuit board design software (Fig. 3-4 (c)). Since the flow resistance of the routing channels is extremely small (around 4 orders of magnitude) compared to that of the mixing layer, the drug solution will fill all the drug reservoirs in seconds when one of the certain drug is loaded to any of the drug reservoirs. The lid layer PDMS covers the mixing layer to form an enclosed microfluidic system. The mixing PDMS layer was flipped to face upward before bonding to lid layer, so that cells could be captured at the $5\ \mu\text{m}$ thin gap in each individual chamber.

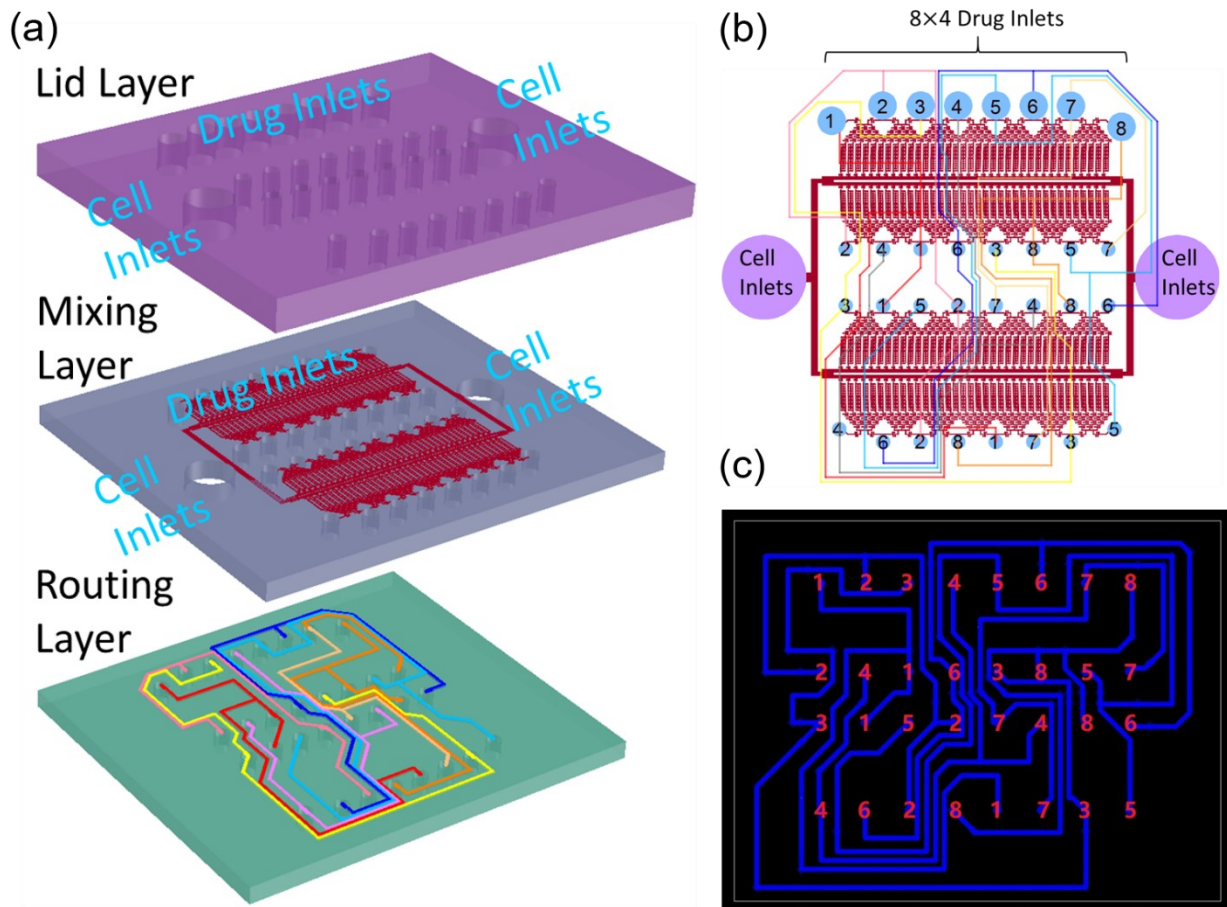


Figure 3-4. Schematics of multiplexed 8-drug combination screening chip. (a) Separate views of three PDMS layers. 32 holes are punched through all the three PDMS layers for drug inlets using 6mm biopsy punch, connecting the mixing and routing layers. (b) Top view of the mixing layer: 32 inlets are allocated to 8 drugs, with a group of 4 connecting to each other with the same number in the routing layer. Before drug treatment, cells were loaded to the inlets and automatically deployed to 1,032 culture chambers driven by gravity flow. Cell inlets are also used for drug outlet during drug treatment process. (c) Top view of the routing layer, same number on different rows are connected in routing layer.

3.6 Validation of logarithmic concentration gradient on-chip

In order to test drug solution mixing on-chip, both fabricated linear concentration gradient device and logarithmic concentration gradient device were loaded with fluorescent dyes. The fluorescent intensity profile could be used to represent the concentration of different drugs. PBS

(no fluorescence) and three fluorescence dyes with different excitation wavelength were used: Tetramethylrhodamine (TRITC, red), Fluorescein (green), and DAPI (blue). After overlaying all the fluorescent images from each channel, we observed a rainbow-like color gradient formed in linear concentration gradient device (Fig. 3-5 (a)). By measuring the fluorescence intensity of all dyes, we verified each of the pairwise compound was mixed in six concentration ratios of 0% :100%, 20%: 80%, 40%: 60%, 60%: 40%, 80%: 20%, and 100%: 0%, which is accordant with simulation results (Fig. 3-5 (c)). For logarithmic gradient generator, due to the tradeoff between the dynamic range and detection resolution of camera, different exposure times were needed to validation high concentration region and low concentration region, respectively. One image was taken with short exposure time (30 ms) to achieve larger detection range and avoid fluorescence saturation, so that the concentration relationship between 10%, 50%, and 90% could be verified (Fig. 3-5 (b)); While the other image is taken using long exposure time (300 ms), enabling the measurement of fluorescence intensity difference between 0%, 1% and 10%. Thus, combining the measurement in these two images, it was validated that the logarithmic mixing ratio in fabricated device matches well with COMSOL simulation results (Fig. 3-5 (d)).

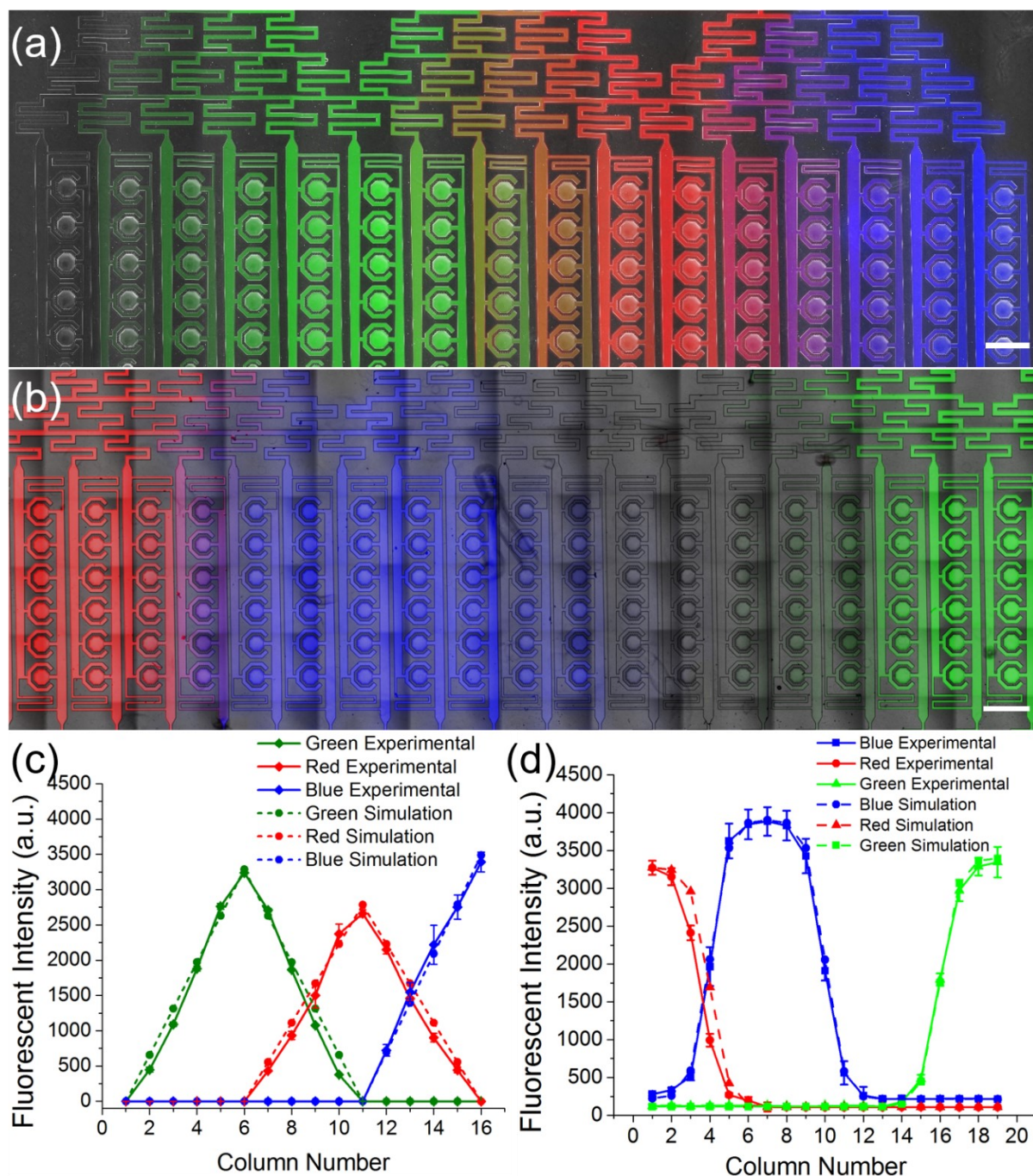


Figure 3-5. Generation of linear and logarithmic concentration gradient validated by fluorescent dye (a) Linear gradient generation using PBS, Fluorescein (green), tetramethylrhodamine (red), and DAPI (blue), from left to right. The final image was created by overlapping images of the brightfield, FITC, TRITC, and DAPI channels. (b) Logarithmic gradient generation using tetramethylrhodamine (red), DAPI (blue), PBS, and Fluorescein (green), from left to right. The final image was created by overlapping images of the brightfield, FITC, TRITC, and DAPI channel. (c) Comparison of fluorescent intensity between linear gradient generation experiment (solid lines) and simulation results (dashed lines). (d) Fluorescent intensity measurement of

logarithmic gradient generation experiment (solid lines), which correlates well with simulation (dashed lines). (Scale bar = 500 μm)

3.7 Cancer cell loading and sphere formation

For cell loading balance considerations, two cell inlets are used on both left side and right side. In the loading process, 500 μL cell suspension is loaded to both cell loading inlets, while the 32 drug inlets are left empty, which are used as outlets. Driven by the pressure difference between cell loading inlets and drug loading inlets, cells are distributed to 1032 sphere culture chambers, and captured at the 5 μm thin gap in each individual chamber. The chamber bottom was designed to be curved (Fig. 3-1 (b)), so that cells finally aggregate at the rounded bottom in central octagonal chamber, which is coated with Pluronic-108. After culturing cells for 1 day, cells form spheroids of uniform size (Fig. 3-1 (c)). By regulating chamber dimensions, we are able to control the equivalent flow resistance of the cell culture gap. The larger the chamber dimension is, the smaller the flow resistance is, the more cells could be captured at the cell capture gap, the larger the spheroids could be finally formed. As a demonstration, we showed that two different sizes of spheres could be achieved (large sphere: $238 \pm 16 \mu\text{m}$ in diameter, small spheres: $124 \pm 11 \mu\text{m}$ in diameter), with two different chamber dimension designs (large chamber: 440 μm in diagonal, small chamber: 240 μm in diagonal), respectively (Fig. 3-1 (d)).

3.8 Synergy effect analysis

To quantify the synergistic effect of various drug combinations, we calculated “Maximum Synergy Index” (MSI) inspired by loewe additivity [41]. Based on dose equivalence principle, that

for a given effect, dose a of drug A is equivalent to dose b_a of drug B, and reciprocally. In addition, dose b_a can be added to any other dose b of drug B to give the additive effect of the combination. The additive effect of drugs A and B can be expressed as [42]:

$$\text{Effect (a + b)} = E_A(a + a_b) = E_B(b_a + b)$$

To quantify the combination synergistic index, we first calculated the linear interpolation value of each combination with different mixing ratio based on single drug effect. For example, drug A with dose a yields $I_a\%$ inhibition rate, while drug B with dose b yields $I_b\%$ inhibition rate. The combination of drug A and drug B with the mixing ratio of 1:1 should yields $I_{ab} = (I_a\% + I_b\%)/2$ inhibition rate. The “synergy index” of drug A and drug B with certain mixing ratio is defined as dividing the experimental inhibition rate $I_{ab,exp}$ by theoretical inhibition rate $I_{ab,theory}$. The largest synergistic index among all the screened mixing ratio between drug A and drug B, which has the best chance of achieving the best therapeutic result, is defined as the Maximum Synergy Index (MSI) of the drug combination between A and B. An MSI greater than 1 indicates a synergistic drug combination, since the maximum inhibition rate of the drug combination is higher than the linear interpolation of individual drugs.

3.9 Drug combination screening on breast and pancreatic cancer cell lines

To demonstrate the efficacy of high-throughput drug combination screening, we conducted a screening experiment with pancreatic cancer cell line, MIA PaCa-2, using a fabricated 8-drug logarithmic concentration gradient chip. All the pairwise combinations of seven chemo-drugs (Cisplatin, Docetaxel, Doxorubicin, Gemcitabine, Irinotecan, Oxaliplatin, Fluorouracil) together with culture media positive control were screened in a single-chip (Fig. 3-6). As a result, we

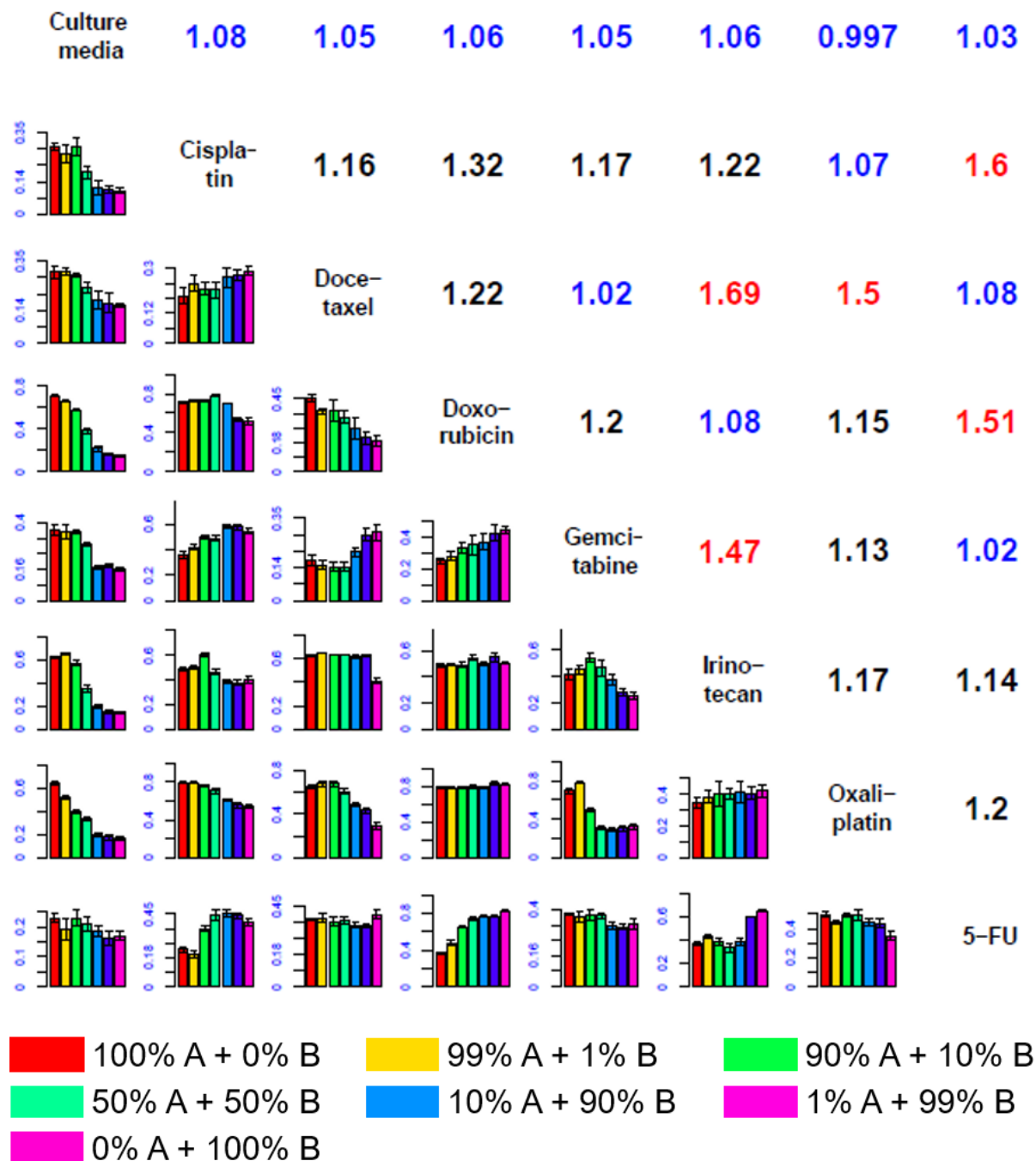


Figure 3-6. Drug combination screening results of control (culture media) and 7 drugs (Cisplatin, Docetaxel, Doxorubicin, Gemcitabine, Irinotecan, Oxaliplatin, 5-FU) using pancreatic cancer cell line MIA PaCa-2. Each subplot in the lower triangular table illustrates the cell death rate under the combination of drugs at each corresponding row and column. Each bar with different colors represent different concentration mixing ratio of certain drug combination. “Maximum Synergistic Index” (MSI) is denoted at upper triangle table, which is defined by the largest synergistic index among all the screened mixing ratio between

the pair of drugs. Synergistic drug combination pairs with high MSI (>1.4) are highlighted in red, while those non-synergistic ones with low MSI (<1.1) are highlighted in blue.

identified a few drug combinations with high synergistic indexes, which were highlighted in red. For example, the combination of docetaxel + irinotecan, doxorubicin + 5-FU, docetaxel + oxaliplatin, and gemcitabine + Irinotecan showed synergistic indexes higher than 1.4, which have been proven to be more effective than single drugs in previous clinical and research literatures [45-48]. While the non-synergistic drug combinations, highlighted in blue in the table, such as cisplatin + oxaliplatin and gemcitabine + 5-FU [49] may result from their similar mechanism of action. Both cisplatin and oxaliplatin are DNA alkylating agents forming platinated intra-strand and inter-strand cross-link, interfering with DNA replication. [50]. While gemcitabine and 5-FU are both belongs to nucleoside analog family of medication, which induces cell apoptosis by inhibiting the synthesis of new DNA [51]. We further demonstrated the general usage for the presented chip for other types of cancer cell lines using SUM159 and MCF7, on a fabricated 4-drug screening chip with linear concentration gradient mixer (Fig. 3-7). We also showed reliable drug combination screening result among 4 fabricated 8-drug screening chips using SUM159 breast cancer cells, with negligible drug efficacy variations among different chips (Fig. 3-8).

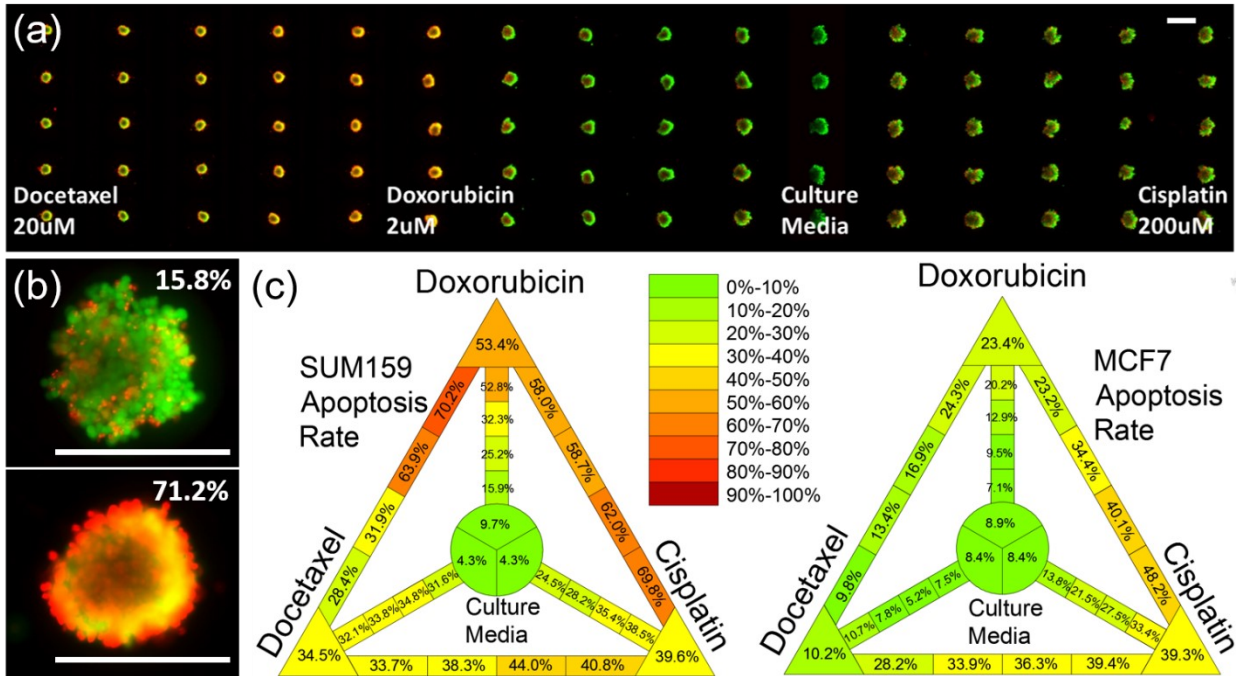


Figure 3-7. SUM159 and MCF7 drug combination susceptibility test. (a) Using 20 μM docetaxel, 2 μM doxorubicin, culture media, and 200 μM cisplatin. Live (green) / dead (red) staining are used after drug treatment for cell viability readout. (b) Example images of 2 spheroids with death rate of 15.8% and 71.2% measured by custom software, respectively. (c) Heterogeneous drug response between SUM159 and MCF7 breast cancer cell lines. Cell death rate under certain drug treatment condition is quantified using different color. SUM159 is susceptible to doxorubicin + docetaxel and doxorubicin + cisplatin, while MCF7 is only sensitive to doxorubicin + cisplatin. (Scale bar = 300 μm)

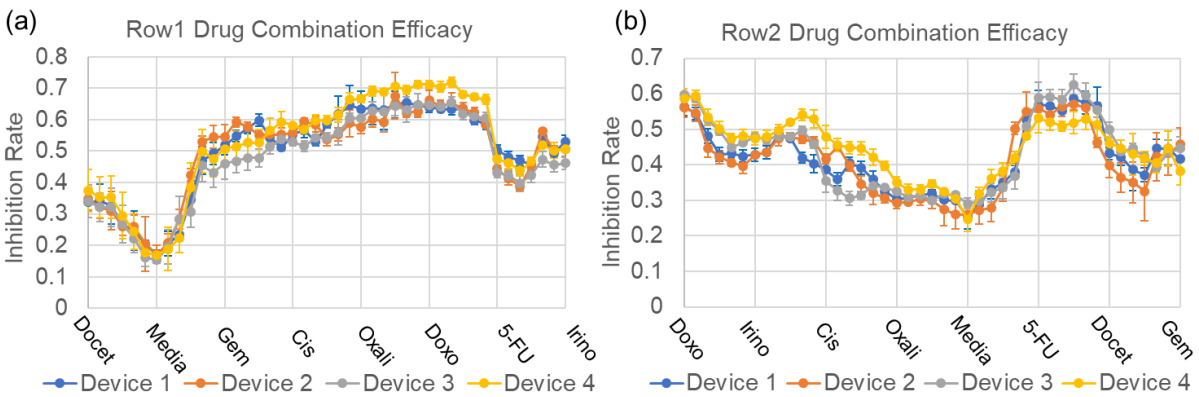


Figure 3-8. Chip-to-chip variance characterization experiment. We repeated drug combination screening experiments on breast cancer cell line SUM159, using 4 fabricated chips under identical treatment conditions. (a) Drug combination screening result in row 1. The average standard deviation among 4 devices is 3.11%, with maximum standard deviation of 5.26% and minimum of 0.79%. (b) Drug combination screening result in row 2. The average standard deviation among 4 devices is 3.36%, with maximum standard deviation of 5.54% and minimum of 0.70%.

3.10 Drug Combination screening on pancreatic cancer PDX cell line

PDX models have been believed as an in vitro cancer mode that is more physiologically relevant more readily applicable to the clinics, due to its preservation of the inter-tumor and intra-tumor heterogeneity, as well as the phenotypic and molecular characteristics of the original cancer [52]. Thus, we further tested pancreatic cancer PDX cell lines to demonstrate the potential of presented chip for precision medicine. Combining the drug combination screening results of three PDX cell line samples, UM5 (Fig. 3-9), UM16 (Fig. 3-10), and UM53 (Fig. 3-11), we established general drug responses of pancreatic cancer to a panel of combination treatments (Fig. 3-12 (a)). Among all drug combinations, a few of them with high average inhibition rate, such as fluorouracil + oxaliplatin, gemcitabine + oxaliplatin, and docetaxel + oxaliplatin, are identified as generally effective drug combinations for pancreatic cancer treatment. In fact, both fluorouracil + oxaliplatin and gemcitabine + oxaliplatin have been approved by US Food and Drug Administration (FDA) for pancreatic cancer combinatorial treatment [53, 54]. In addition, we also pinpointed the unique drug responses of each PDX sample. For UM16, none of the well-accepted drug combination was effective in inhibiting cell growth (Fig. 3-12 (b)). The non-conventional combination of gemcitabine and docetaxel, however, achieved a good drug efficacy. UM5 showed resistant to most of the drug compound except for the combination of 10% gemcitabine and 90% Oxaliplatin (Fig. 3-12 (c)). The heterogeneous drug response among different patient samples confirmed the

importance of customizing personalized chemotherapy for each individual. The successful combinatorial drug screening experiments using PDX cell lines suggest the potential of the presented platform in discovering new combination and precision medicine.

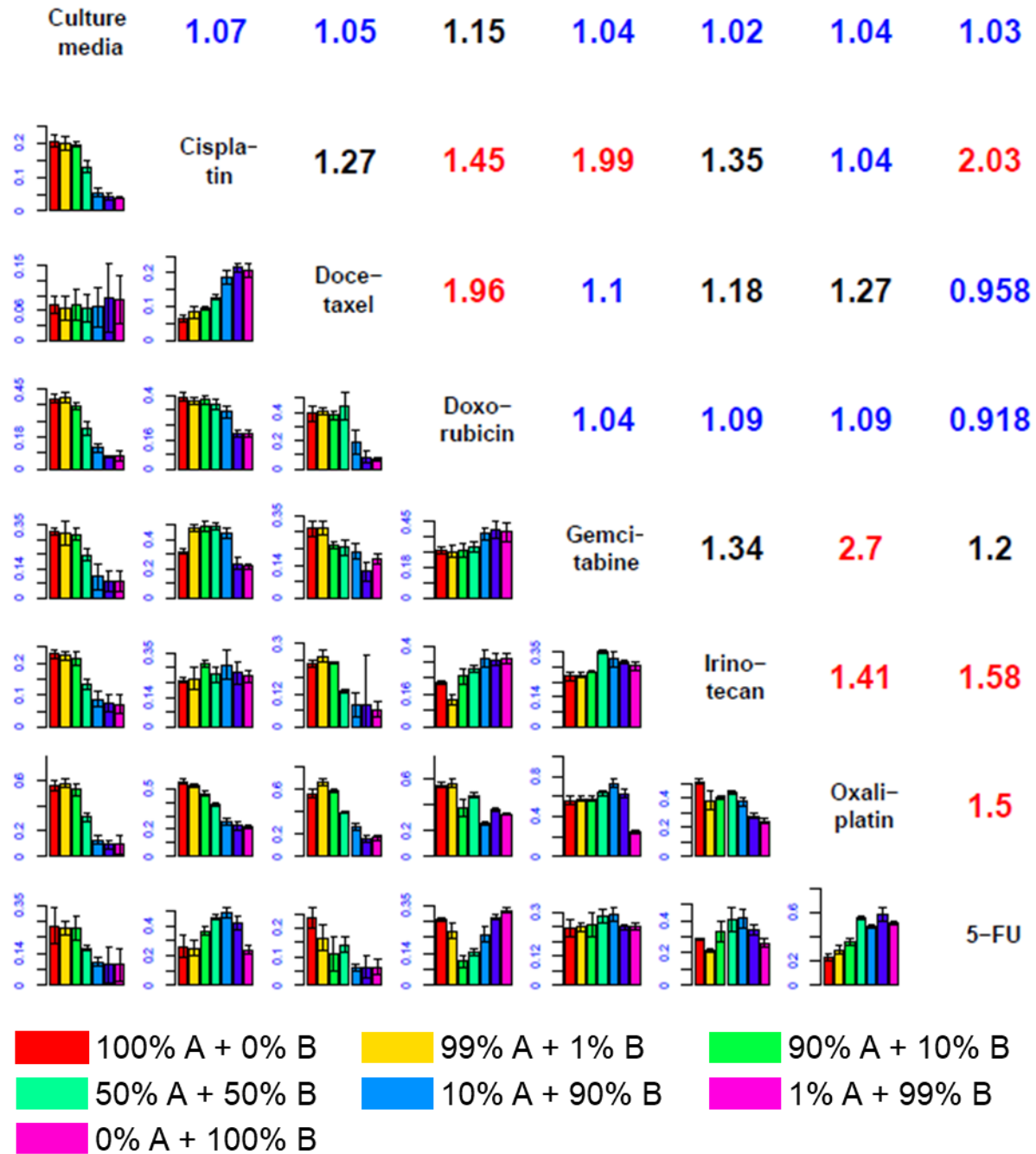


Figure 3-9. Drug combination screening results of UM5 using 7 commonly used chemo-drugs and control (culture media). With the name of all compounds are denoted at diagonal entries, each subplot illustrates the cell death rate under the combination of drugs at each corresponding row and column. Maximum Synergistic Index (MSI) is denoted at upper triangle table. Highly synergistic pairs are highlighted in red ($MSI > 1.4$), while non-synergistic ones are highlighted in blue ($MSI < 1.1$).

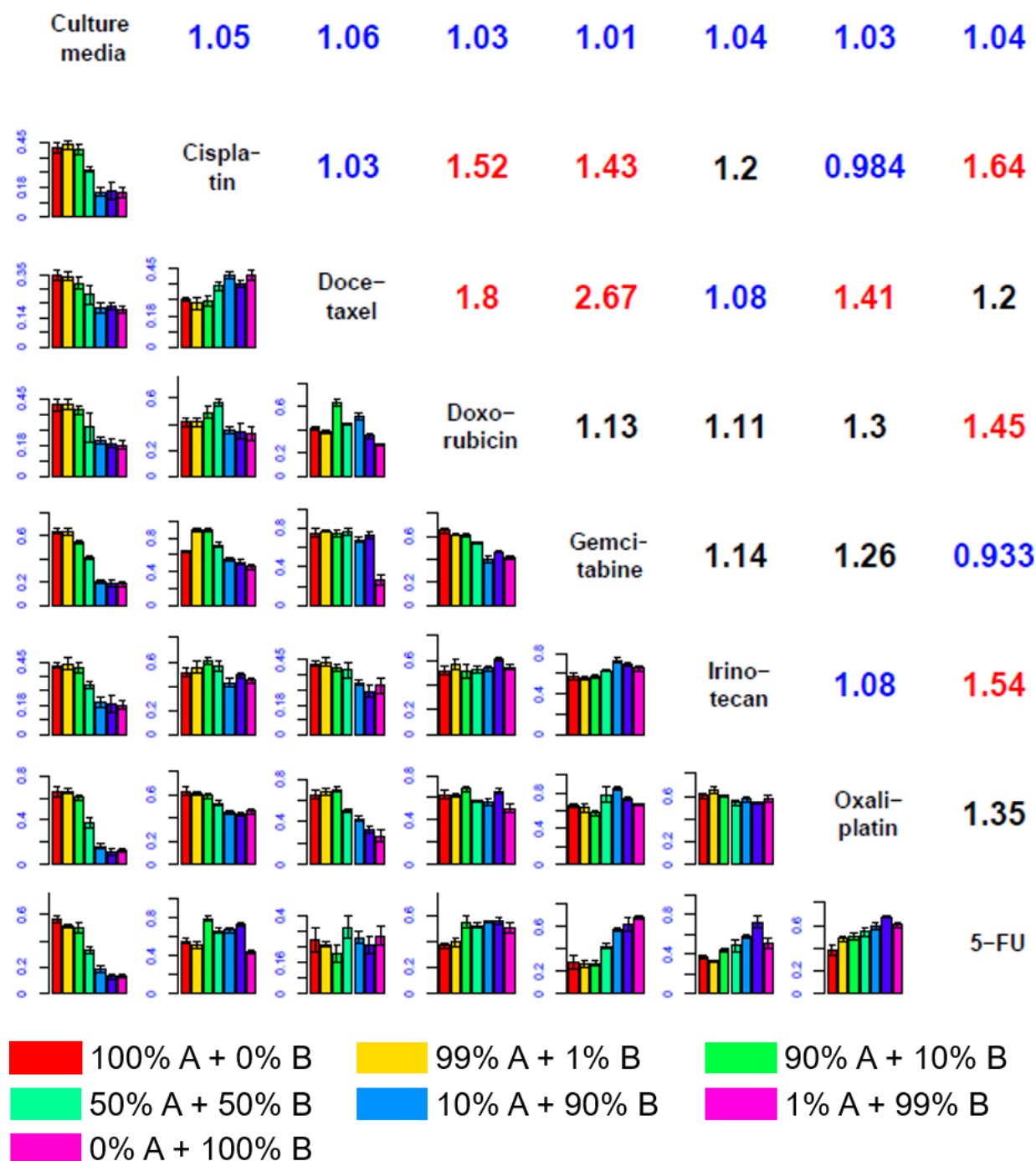


Figure 3-10. Drug combination screening results of UM16 using 7 commonly used chemo-drugs and control (culture media). With the name of all compounds are denoted at diagonal entries, each subplot illustrates the cell death rate under the combination of drugs at each corresponding row and column. Maximum Synergistic Index (MSI) is denoted at upper triangle table. Highly synergistic pairs are highlighted in red ($MSI > 1.4$), while non-synergistic ones are highlighted in blue ($MSI < 1.1$).

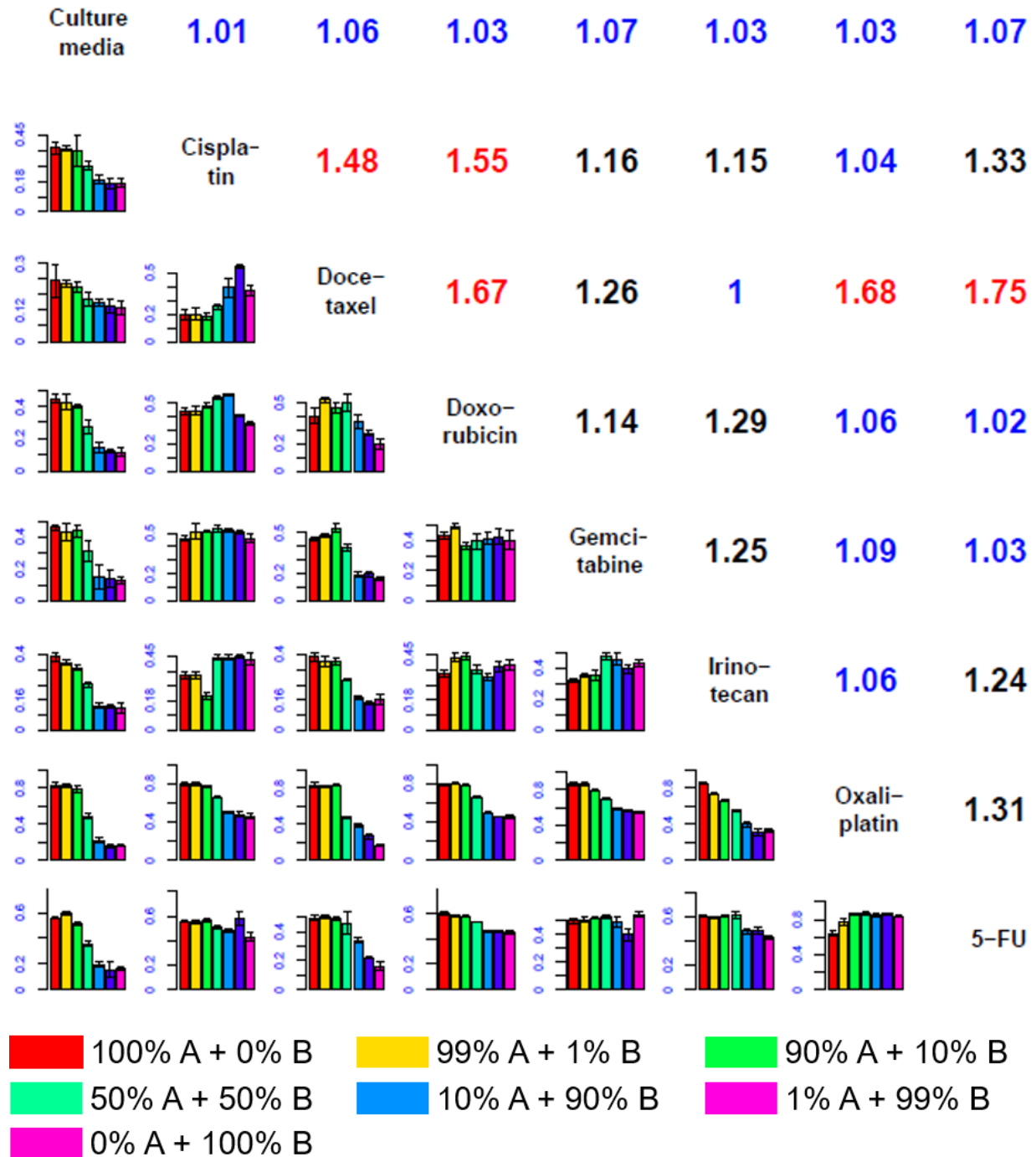


Figure 3-11. Drug combination screening results of UM53 using 7 commonly used chemo-drugs and control (culture media). With the name of all compounds are denoted at diagonal entries, each subplot illustrates the cell death rate under the combination of drugs at each corresponding row and column. Maximum Synergistic Index (MSI) is denoted at upper triangle table. Highly synergistic pairs are highlighted in red ($MSI > 1.4$), while non-synergistic ones are highlighted in blue ($MSI < 1.1$).

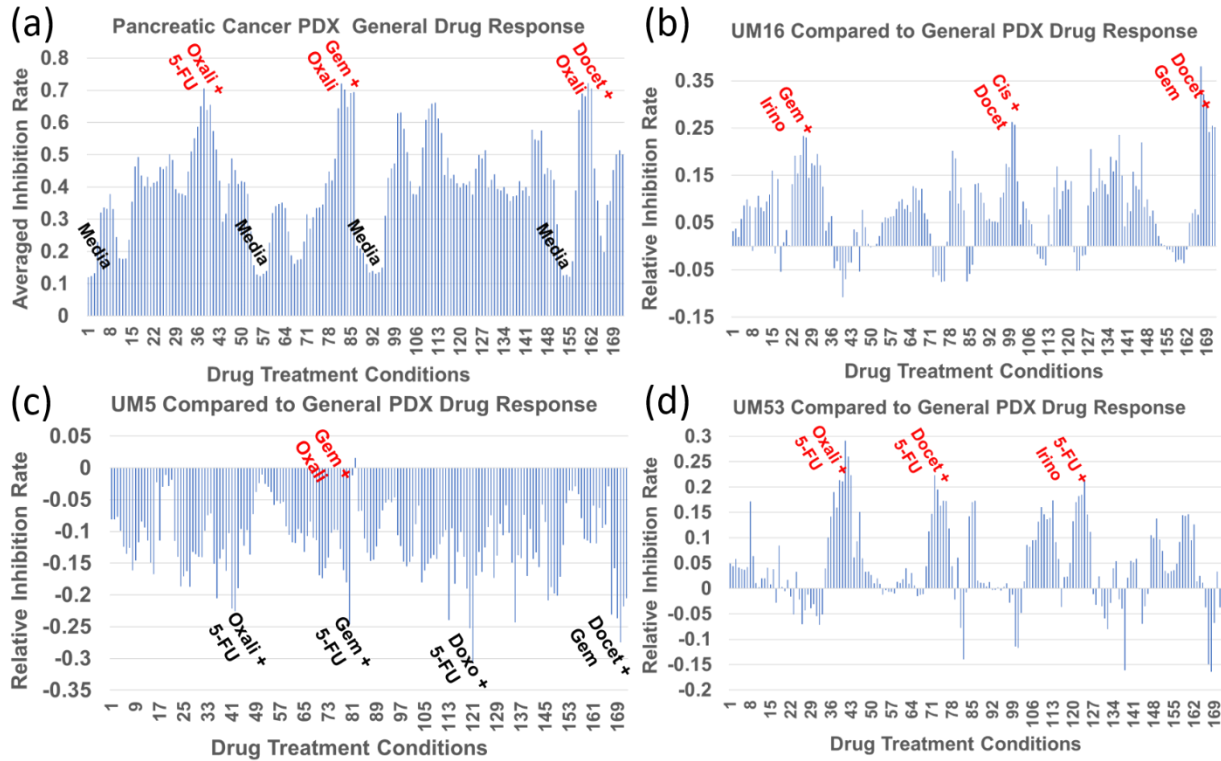


Figure 3-12. Drug combination screening results of control (culture media) and 7 drugs (Cisplatin, Docetaxel, Doxorubicin, Gemcitabine, Irinotecan, Oxaliplatin, 5-FU) using pancreatic cancer PDX cells. 172 different pairwise drug combinations with different mixing ratios are listed in X-axis. (a) Average drug response of all PDX cells for 172 different drug treatment conditions. (b) UM16 relative drug responses compared to the average drug response of all PDX cells. (c) UM5 relative drug responses compared to the average drug response of all PDX cells. (d) UM53 relative drug responses compared to the average drug response of all PDX cells.

3.11 Chapter summary

We reported a high-throughput, easy-handling, multiplex drug-combination screening platform scheme. By innovatively using three-layer PDMS structure, drug inlets sharing scheme, and specially arranged drug inlets array, we successfully demonstrated the feasibility of scaling up combinatorial drug screening for larger number of drugs. In addition, we presented a logarithmic concentration gradient generator, which provides a wider dynamic concentration range as compared to linear gradient generator. Furthermore, we adopted 3D tumor spheroids models for drug screening to better mimic *in vivo* tumor microenvironment. The design of spheroid culture chamber with 5 μm cell capture gap, micropillar array, and rounded bottom structure guaranteed the formation of uniform spheroids of $238 \pm 16 \mu\text{m}$ in size. As a demonstration of the design scheme, we fabricated an 8-drug combination screening chip, which generates ${}^8C_2 = 28$ pairwise drug combinations, with 7 mixing ratios between each pair of drugs, yielding 172 different treatment conditions. Combining 6 replicates for each treatment condition, 1,032 drug efficacy screening experiments can be accomplished in a single 8-drug screening chip. The drug screening experiment using pancreatic cancer cell line, MIA-PaCa-2, identified the synergistic effects between docetaxel + Irinotecan, doxorubicin + 5-FU, docetaxel + oxaliplatin, and gemcitabine + Irinotecan, which match well with the clinical trial results reported in literature. We further verified the application of the fabricated chip in precision medicine using patient derive xenograft (PDX) cell lines, which better mimic the drug response of patients. We pinpointed the most synergistic drug combinations for each patient based on our screening results. The preliminary results verified the efficacy and synergistic effect of high-throughput drug combination screening. The presented design approach is easily scalable to incorporate a large number of drugs for large-scale drug screening.

Chapter 4 : High-Throughput Microfluidic Clonal Sphere Chip Identifies Cancer Stem Cells Located at the Leading Edge of Tumorigenic Subclones

Cancer heterogeneity refers to the co-existence of multiple subclones with distinct genotypic and phenotypic properties, which contributes to drug resistance and cancer relapse. Cancer heterogeneity can be interpreted in two levels: inter-clonal heterogeneity and intra-clonal heterogeneity. Inter-clonal heterogeneity represents the morphological and molecular variation between multiple tumor clones. On the other hand, intra-clonal heterogeneity stands for the cellular diversity within each individual clone. This cellular level of heterogeneity could be introduced by the spatial distribution of each individual cancer cell within a clonal sphere, which introduces different exposure to tumor-microenvironment cues, and thus diversified differentiation stages. In order to understand cancer hierarchy and drug resistance, clonal sphere derived from a single cancer cell has been widely used. However, very few works incorporate both levels of heterogeneity. In this work, we studied the topic of inter-clonal and intra-clonal heterogeneity as a whole, using a high-throughput clonal sphere (Hi-Sphere) chip combined with fluorescence labelling techniques. The Hi-Sphere chip is capable of culturing more than 2,400 single-cell-derived clonal spheres and selectively retrieve them based on sphere size. By combining fluorescence labelling technique, we compared cells from the tumor leading edge to the tumor core. We discovered the majority of cancer stem-like cells (CSCs) were located at the leading edge of a specific subclone, called holoclone. This preliminary result not only validated the feasibility of using Hi-Sphere chip for both inter-tumor and intra-tumor heterogeneity studies, but it also provided us the spatial information of CSC for future drug resistance studies.

4.1 Introduction

Solid tumors are inherited heterogeneous diseases containing cancer cells at different stages of differentiation [1]. It has been widely believed that tumor heterogeneity contributes to tumor progression, metastasis, drug resistance and tumor relapse [2]. As tumor progresses, the increased cellular heterogeneity gives rise to a multitude of neoplastic cells presenting distinct morphological and signaling signatures [3]. In general, there are two levels of tumor heterogeneity: inter-tumor heterogeneity and intra-tumor heterogeneity [4, 5]. The coexistence of inter-tumor heterogeneity and intra-tumor heterogeneity makes it more challenging to understand the complex tumor hierarchy and develop cancer therapy. Although considerable efforts have been made in studying cancer cell heterogeneity at different level [6, 7], these works treated inter-tumor and intra-tumor heterogeneity as separate topics. There is a need to bridging the gap between tumor hierarchy levels and consider these tumor signatures as a whole.

Inter-tumor heterogeneity refers to the phenotypic and molecular variation between multiple tumors or subclones from the same patient source [8]. For example, a recent hypothesis of tumor hierarchy categorizes tumor clones as holoclones, meroclones and paraclones [9], which are derived from stem cells, transit-amplifying cells and differentiated cells, respectively. It is believed that holoclones play an important role in tumor proliferation and relapse [10]. Meanwhile, a deeper level of tumor heterogeneity is known as intra-tumor heterogeneity, which deals with the individual cancer cells with distinct cellular features within a solid tumor [11]. Among many intra-tumor heterogeneity mechanisms, cancer stem-like cell (CSC) model has shown to play a pivotal role [12, 13]. CSCs are a small subpopulation of cells within tumors capable of self-renewal, differentiation, and tumorigenicity. The search for strategies targeting CSCs represents one of the emerging fields in cancer studies [14]. A large number of surface marker (CD24, CD44, ALDH,

EpCam) has been used to identify CSCs among bulk populations. However, none of these markers has been validated as universal gene among all cancer types. It is fundamentally challenging to pinpoint CSCs without direct correlation with CSC behavioral signature [15, 16]. Recently, Cancer cell sphere culture models using sphere-forming assays are valuable tools to study the biology of CSC [17]. When cancer cells are cultured in serum-free suspension condition, bulk non-stem cells undergo apoptosis due to loss of anchorage [18], while only CSCs survive and proliferate to form spheres [19]. Based on this unique property of CSCs, sphere formation assay has been widely used in selection and enrichment of CSCs [20, 21]. An ideal sphere formation assay should avoid cell aggregations at the initial seeding step, so that anchorage-dependent cells cannot survive and dilute CSCs population. Most of the conventional clonal sphere assays, like micro-titer plates [22, 23], hanging-droplet assays [24], and robotic dispensing [25] suffer from poor control of single cell isolation, lack of long-term culture capability, or costly automatic control system. It is hard to measure the clonal sphere formation rate accurately and explore CSC heterogeneity.

In recent decades, microfluidics emerges as a promising technique for single cell clonal sphere culture [26]. Considerable development has been achieved in high-throughput single cell encapsulation and long-term clonal sphere culture tasks. However, it is also very critical to develop the technique of separation and re-collection of clonal spheres based on the clonal and cellular heterogeneous property. In this work, we presented a high-throughput microfluidic clonal sphere (Hi-Sphere) chip (Fig. 4-1 (a)), which enables: (1) 3,200 individual chambers for hydro-dynamic single-cell isolation, (2) long-term clonal sphere culture and automatic sphere size tracking, (3) easy retrieval and separation of different subtypes of clonal spheres for inter-sphere heterogeneity study. (4) a fluorescent labelling technique correlating cancer cell spatial location and stem-like features for investigation of intra-tumor heterogeneity. With the help of Hi-Sphere chip, we first

validated that certain subtypes of clonal spheres are poised with self-renewal potentials and tumorigenic properties. Based on that, we further compared cells located at the outer periphery (leading edge) of the spheres and cells at the inner core of the spheres. Using both phenotypic assays and biomarker analysis, we confirmed our discovery that the majority of the CSC cells were located at the outer part of the spheres, while only a small portion of CSCs were found at the inner core. These findings provide us a better understanding of the tumor heterogeneity as a whole and help targeting specific cancer populations.

4.2 Hi-Sphere chip for clonal sphere culture

Inspired by the previous work on microfluidic single cell capture chip [30], the presented microfluidics Hi-Sphere chip is composed of 3,200 individual culture chambers (32 rows by 100 columns), with $150\ \mu\text{m} \times 150\ \mu\text{m}$, and $100\ \mu\text{m}$ in height (Fig. 4-1 (a)). The culture chambers on the same row are connected to the inlet and the outlet by two main channels ($100\ \mu\text{m}$ in height), respectively. Each culture chamber consists of a single cell capture site, which is $5\ \mu\text{m}$ in height and $10\ \mu\text{m}$ in width. A single cancer cell flowing into the sphere culture chamber will block the cell capture site, preventing the next cancer cell to enter the same chamber (Fig. 4-1(b)). This hydrodynamic cell capture design minimizes the contamination from multiple-cell-plating cases (3.9%), while achieving high-throughput single cell clonal sphere culture ($81.6\% \pm 13.2\%$), which

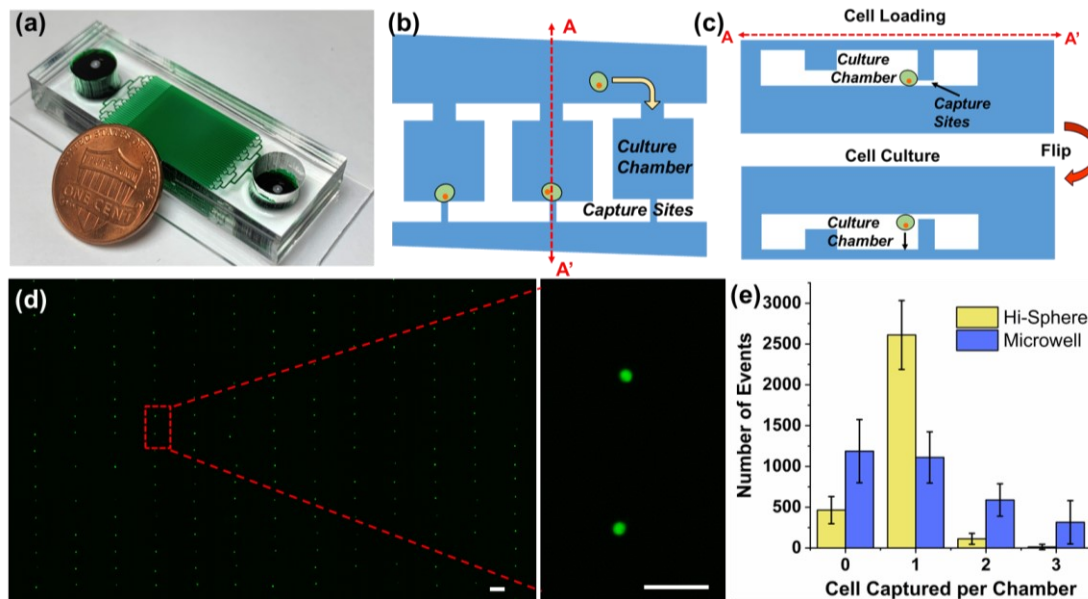


Figure 4-1. Overview of the Hi-Sphere chip design (a) Photograph of a fabricated device. (b) Schematic of the Hi-Sphere chip. Driven by gravity flow, single cells flew from inlets to culture chambers, and captured at capture site. (c) Cross-section view of Hi-Sphere chip while cell loading and cell culture. Once single cells captured in culture chambers, microfluidic chip was flipped upside down. Cells fall inside deep culture chambers and get isolated. (d) A sample microscope image of Hi-Sphere chip after cell loading. (e) Comparison between Hi-Sphere devices and microwell devices. (Scale bar = 100 μm)

is much higher than the single cell chamber percentage ($34.7\% \pm 9.8\%$) in microwell devices (Fig. 4-1 (d), (e)). In order to demonstrate the reliability of culturing spheres using Hi-Sphere chips, we loaded patient-derived-cell line, HN-13 cells, to five identical Hi-Sphere device replicates. They were imaged on day 0 (right after loading), day 3, day 6, and finally day 12 (Fig. 4-2 (a)). A custom MATLAB program was applied to the collected microscope images to automatically measure the sphere size. Though individual single cells have wide range of sphere-forming capability and different growing curve, the collection of a large number of single cells in each device show similar distribution in day 12 sphere size (Fig. 4-2 (b)). We further quantified the sphere-forming potential by calculating the percentage of spheres that with diameter larger than 70 μm on day 12 out of all

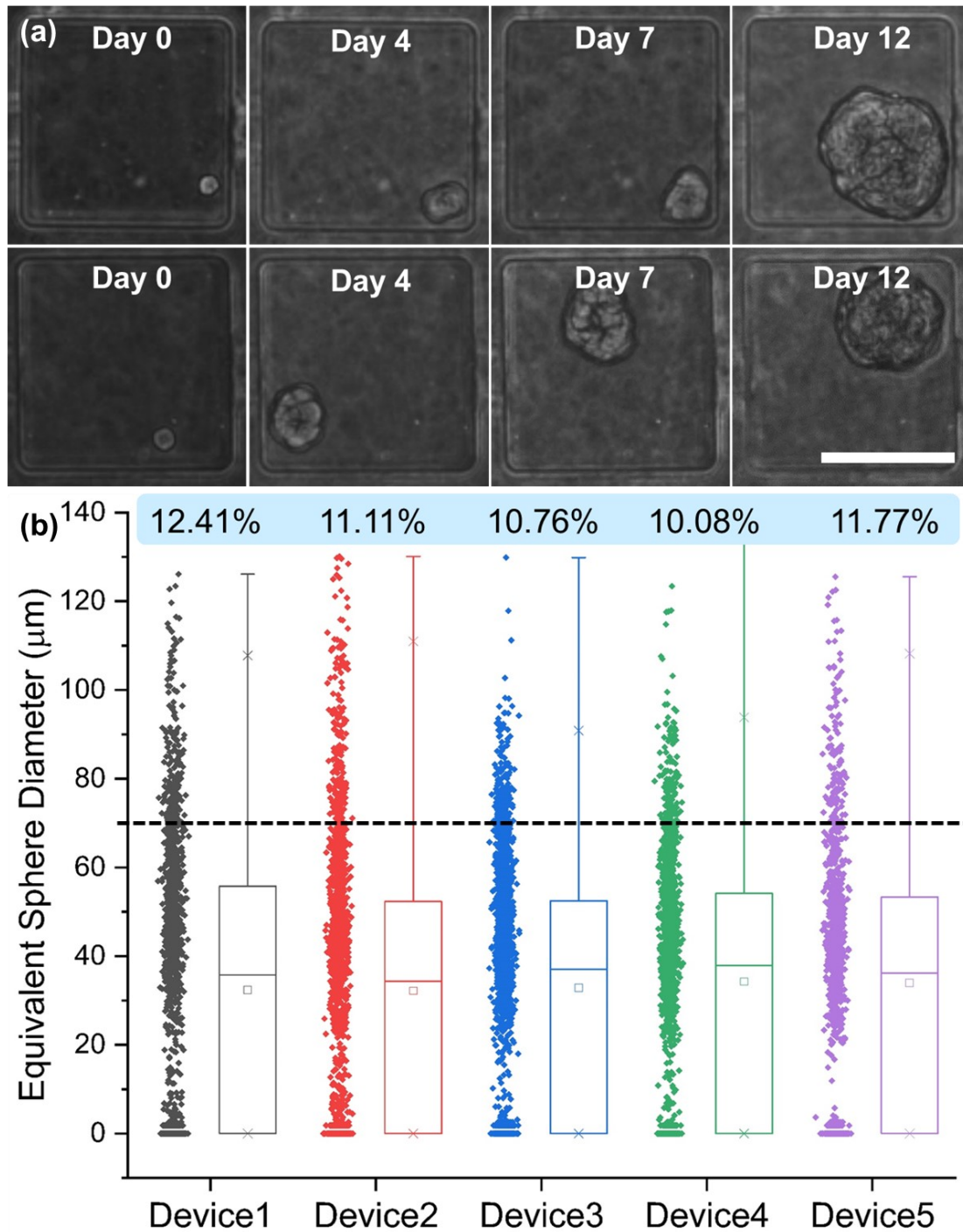


Figure 4-2. Sphere culture and size tracking using Hi-Sphere chip. a) Microscope images showing single cell clonal sphere growth on day 0, day 3, day 6, and day 12. b) Day 12 sphere equivalent diameter measured across 5 devices. The similar sphere size distribution across different devices showing reliability and repeatability. Using 70 μm as the threshold for holo-spheres, HN-13 cells has $11.2\% \pm 0.9\%$ sphere formation rate. (Scale bar = 100 μm)

loaded single cells. As a result, the sphere formation rate across 5 device replicates is $11.2\% \pm 0.9\%$ (S.D.). This indicates that the sphere culture experiment is repeatable across different devices.

4.3 Chip flipping strategy for sphere culture

In recent decades, considerable development has been achieved in single cell encapsulation and long-term clonal sphere culture tasks. However, very few works put their efforts on selectively retrieving the spheres based on sphere size for further analysis. On the other hand, accumulating evidence suggests that tumor heterogeneity may contribute to tumor progression, metastasis, and drug resistance to targeted therapy [2, 32, 33]. The technique for separation and re-collection of clonal spheres based on the heterogeneous property will be very valuable in studying the cause the consequence of tumor heterogeneity. We realized that there is a fundamental tradeoff between the ease of sphere retrieval and the risk of losing track of clonal spheres using our scheme: a sphere should escape its culture chamber very easily if we wish to collect it after the experiment, but should remain steady in the culture chamber during the assay period. In order to solve this dilemma, we proposed a chip-flipping culture method. The microfluidic chip was flipped upside down after cell loading process was complete (Fig. 4-1 (c)). We put 200 μ L cell culture media to the inlet, while 100uL cell media in the outlet. Due to the decreased hydraulic pressure fails to push the cancer cells at the capture site, and gravity force drives the cells to fall in the deep-well like culture chambers. In this way, these cells remain in their chambers even if there is any backflow. When the assay is complete, we could simply flip back the chip to let the spheres fall on the blank substrate.

4.4 Size-based selective sphere retrieval for inter-sphere heterogeneity study

One hypothesis on CSC hierarchy categorizes cancer subclones based on morphological appearance, including holoclone, meroclone, and paraclone. Holoclones containing self-renewing stem cells, and meroclones containing transient amplifying cells and differentiated cells [9, 34]. Only holoclones are capable of serial passage and generate all three types of clones, while meroclones and paraclones have very limited proliferation potential. However, some literatures discovered that holoclones and meroclones could also transit to each other in long-term lineages [6, 9]. Therefore, there has been some debates on the distribution of tumor initiating cells in different subclones. Most of the previous works only address this problem by measuring CSC marker expression. However, variations in CSC characteristics were observed with different CSC markers [35]. There is a need in selecting and studying CSCs with phenotypic behavior approaches.

With the advantages of reliable single-cell clonal sphere culture and easy sphere retrieval, Hi-Sphere chip provides a convenient way of identifying tumor-initiating cells from different subclones. In order to separate holo-spheres and other types of spheres, we designed a size-based sphere retrieval strategy consists of two steps (Fig. 4-3 (a)). In the first step, we flipped back the microfluidic chip to the orientation as cell loading, followed by applying negative pressure on device input using a Pasteur pipette bulb (~1000Pa). The backflow pushed spheres moving out of the culture chambers through connecting channels. Since mero-spheres and para-spheres were loosely formed spheres that were smaller than the size of connecting channels (Fig. 4-3 (b)), around 95% of these clones would be selectively collected at the device inlets. On the other hand, holo-spheres, which were in rounded-shape and larger than 70 μm in diameter, remained on chip and could be collected after peeling apart the chip. These two groups of spheres were collected to two

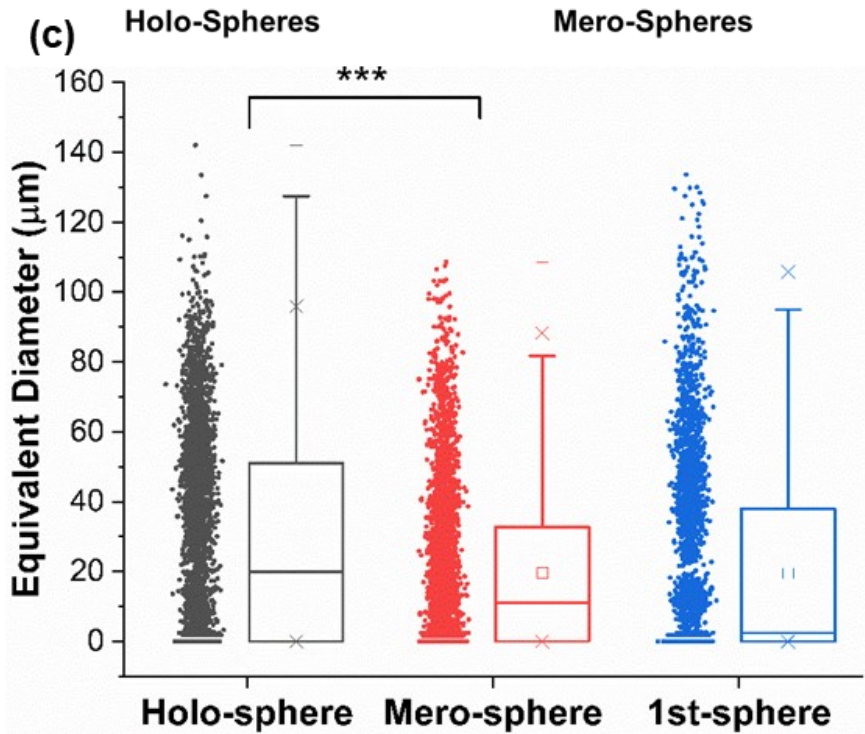
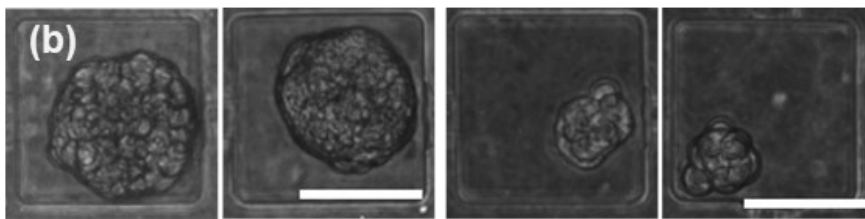
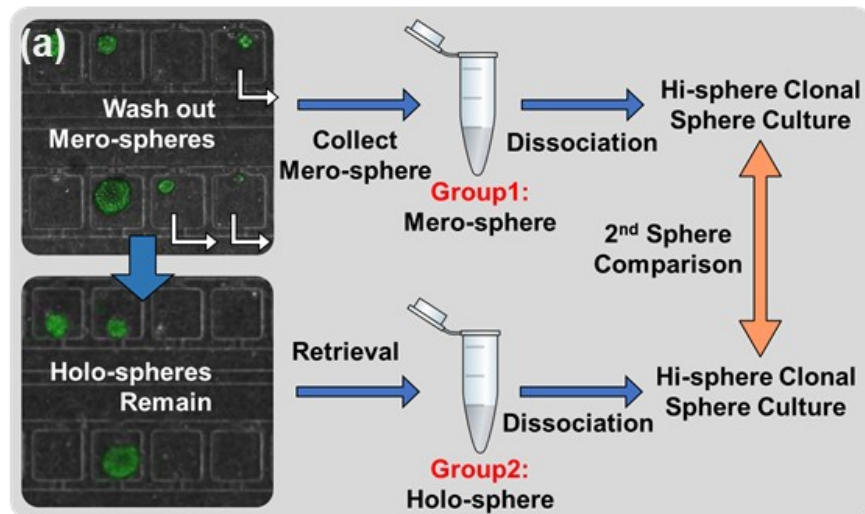


Figure 4-3. Hi-Sphere selective retrieval for inter-sphere heterogeneity study. a) Schematics of holo-spheres, mero-spheres selective retrieval: flipping back the microfluidic chip to the orientation as cell loading, applying negative pressure on device input. The backflow pushes spheres moving out of the culture chambers through connecting channels. Mero-spheres escaped

culture chambers due to loosely connected structure and smaller size. b) Sphere size distribution of holo-spheres and mero-spheres in 2nd generation, compared to 1st generation spheres. (Scale bar = 100 μ m)

separate tubes, dissociated to single cell suspensions, and re-loaded to two groups of Hi-Sphere chips for another generation of sphere culture.

We compared the 2nd Generation Clonal Sphere (2-GCS) formation rates between the single cells from holo-spheres and the other two type of spheres. As a result, 2-GCS formation rate of holo-spheres is significantly higher than that from other types of spheres (Fig. 4-3 (c)). This 3D sphere culture result provides phenotypic behavioral evidence that tumor initiating cells are mainly contained in holoclones. There is another interesting observation when we compare 2-GCS with the 1st Generation Clonal Sphere (1-GCS). Although the collected 1-GCS holo-spheres generate similar percentage of holo-spheres population in 2-GCS, the average sphere size in 2-GCS holo-sphere group is much higher than that in 1-GCS. This indicates that a large number of non-sphere-forming cells in 1-GCS go apoptosis during sphere culture, while cells with self-renewal potentials get enriched by selectively collecting holo-spheres and 2nd generation sphere culture.

4.5 Cell tracker staining enabling intra-sphere heterogeneity study

After observing that most sphere-forming cells were enriched in holo-spheres, we took a further step to explore inside the holo-spheres to investigate intra-sphere heterogeneity. We developed a fluorescent dye staining protocol to distinguish whether a cancer cell is originated from sphere leading edge and sphere core after dissociating the spheres to single cells (Fig 4-4 (a)). Cell Tracker CMFDA fluorescent dye has been widely used for live cell tracking. It utilizes

ubiquitous glutathione transferase inside cells. We confirmed that it has negligible long-term influence in cell metabolism and proliferation. We stained the clonal spheres with Cell Tracker dye while the spheres were still intact. Due to a reasonably large molecular weight (MW = 464.8581), the CMFDA molecule diffused through the compact holo-sphere structure and created a concentration gradient along the radius of the sphere (Fig. 4-4 (b)). Given short incubation time in dye solution, cancer cells at sphere leading edge are exposed to the dye molecules with longer time and higher concentration compared to those at SC, which makes the outer parts of the spheres much brighter in fluorescence. Since the dye molecule converts to a cell-impermeant product that can be retained stable in living cells [36], this process helps us identify cells at sphere leading edge cells against cells at sphere core, even after sphere dissociation. In order to eliminate the variations in glutathione transferase reaction due to different sphere size and structure, we only took top 30% of all cancer cells in fluorescence intensity as sphere leading edge, and bottom 30% as sphere core (Fig 4-4 (c)). In order to validate that the staining protocol effectively separates cells in spheres based on spatial location, we compare staining spheres to staining bulk single cells using the protocol. Since bulk single cells were well-exposed to dye molecules, more than 98% of the bulk single cells shows higher fluorescent intensity than the threshold of sphere leading edge. While no bulk single cell falls to the fluorescent intensity range of sphere core. This demonstrated a clear separation of cells from sphere leading edge and sphere core using top 30% and bottom 30% brightness as the thresholds.

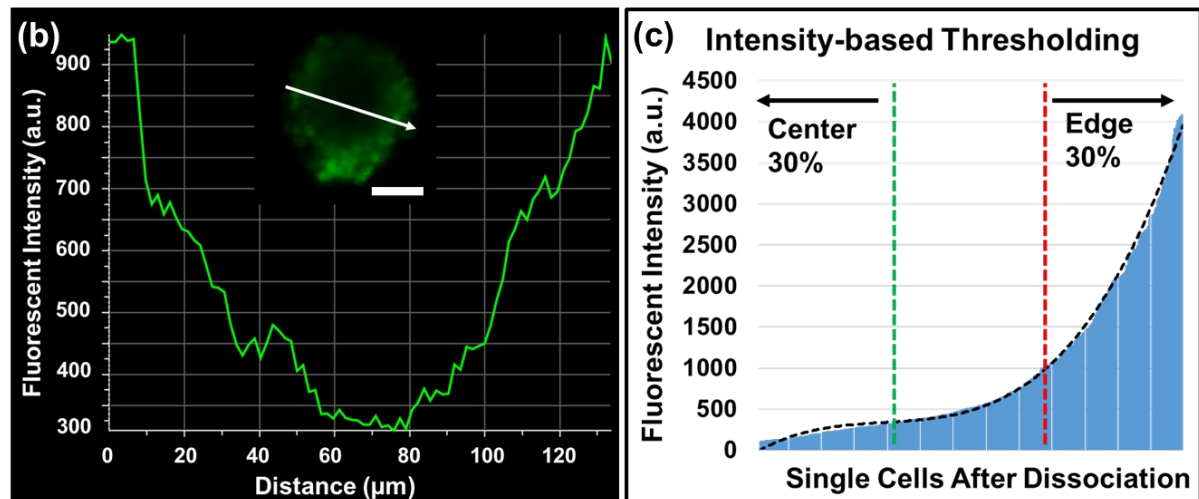
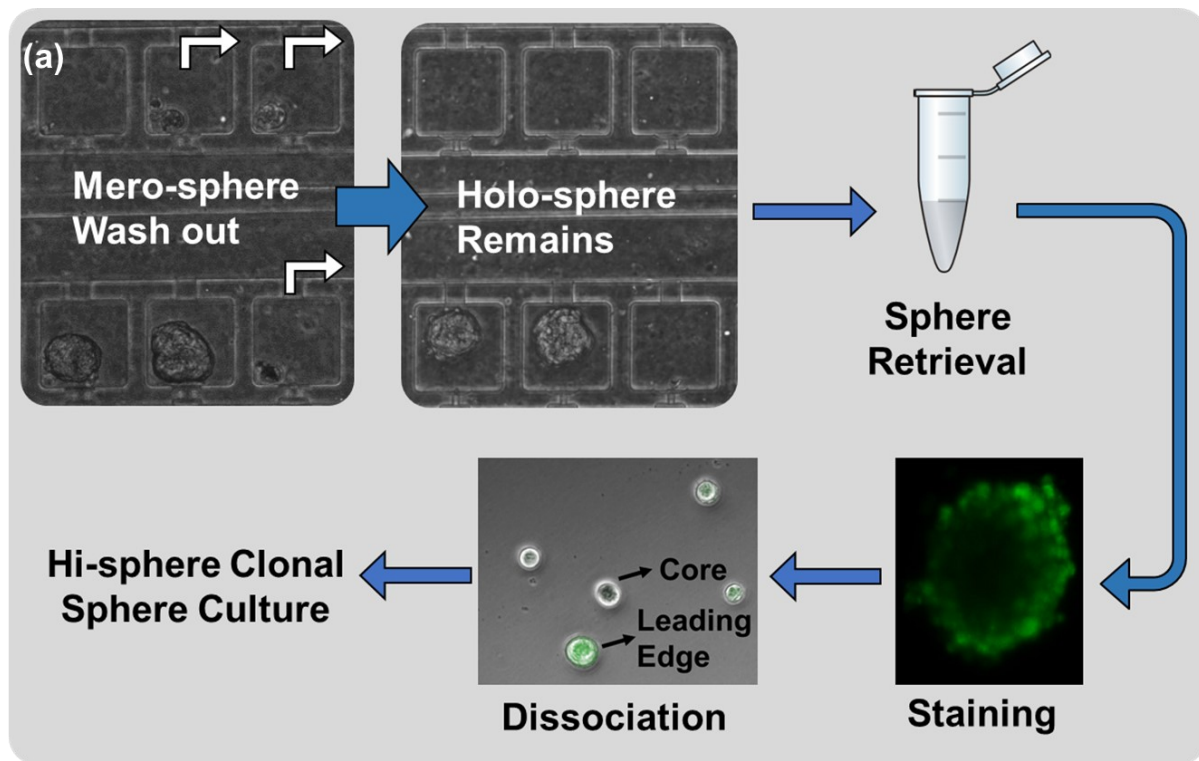


Figure 4-4. Holo-sphere retrieval and staining to identify cells located at sphere edge and sphere core. a) Holo-spheres were stained with Cell Tracker CMFDA dye for 5 minutes before dissociation. Cells from leading edge absorbs more fluorescent dye compared to those from center. b) Fluorescent dye intensity distribution in a holo-sphere. The leading edge is much brighter than sphere core. c) single cell fluorescence intensity distribution after sphere dissociation. Top 30% bright cells were identified as leading edge, while bottom 30% cells were identified as sphere core. (Scale bar = 50 μm)

4.6 High aldehyde dehydrogenase activity in leading edge cells

Aldehyde dehydrogenase (ALDH) class has been proposed as the primary marker for CSCs in many literatures [37, 38]. In order to validate genetic characteristics of the selected sphere-forming cells in holo-spheres, we quantified the cellular ALDH activity using a patient-derived head and neck cancer cell line, HMC-3B. After staining with cell tracker, the spheres were dissociated to single cell suspensions and incubated with AldeRed ALDH activity assay (Fig. 4-5 (a)). To keep the CSC population consistent with the sphere-forming-cell ratio measured with sphere formation experiment, we selected top 12% brightest cells of the whole population as ALDH^{high} cells.

We discovered that most of the ALDH^{high} cells in holo-spheres were found in sphere leading edge (n=61), while only a small population were located at sphere core (n=5) (Fig. 4-5 (b)). The correlation between ALDH activity with cell tracker fluorescent intensity ($r=0.62$) suggested that the closer a cancer cell is to the leading edge, the higher chance that this cell has the CSC-like properties. However, this correlation between stemness and spatial location in sphere relied on the assumption that, there was no intrinsic correlation between the ALDH activity and glutathione transferase activity. In order to investigate this dependency, we repeated the same staining process on dish-cultured bulk cells as control experiment (Fig. 4-5 (c)). We had the following interesting observations: 1) there was weak correlation in the fluorescent intensity between cell tracker dye and AldeRed dye on individual single cells, with Pearson's correlation $r = 0.28$. It validated that the linear correlation between the intensity of the two dyes results from the location-dependent cancer stem-like properties. 2) Using the same AldeRed fluorescence intensity as criterion (21.4 a.u., top 12% brightest cells in spheres), we identified 12/551 ALDH^{high} cells (2.18%) in dish-cultured control group. This ratio was comparable with that from sphere core,

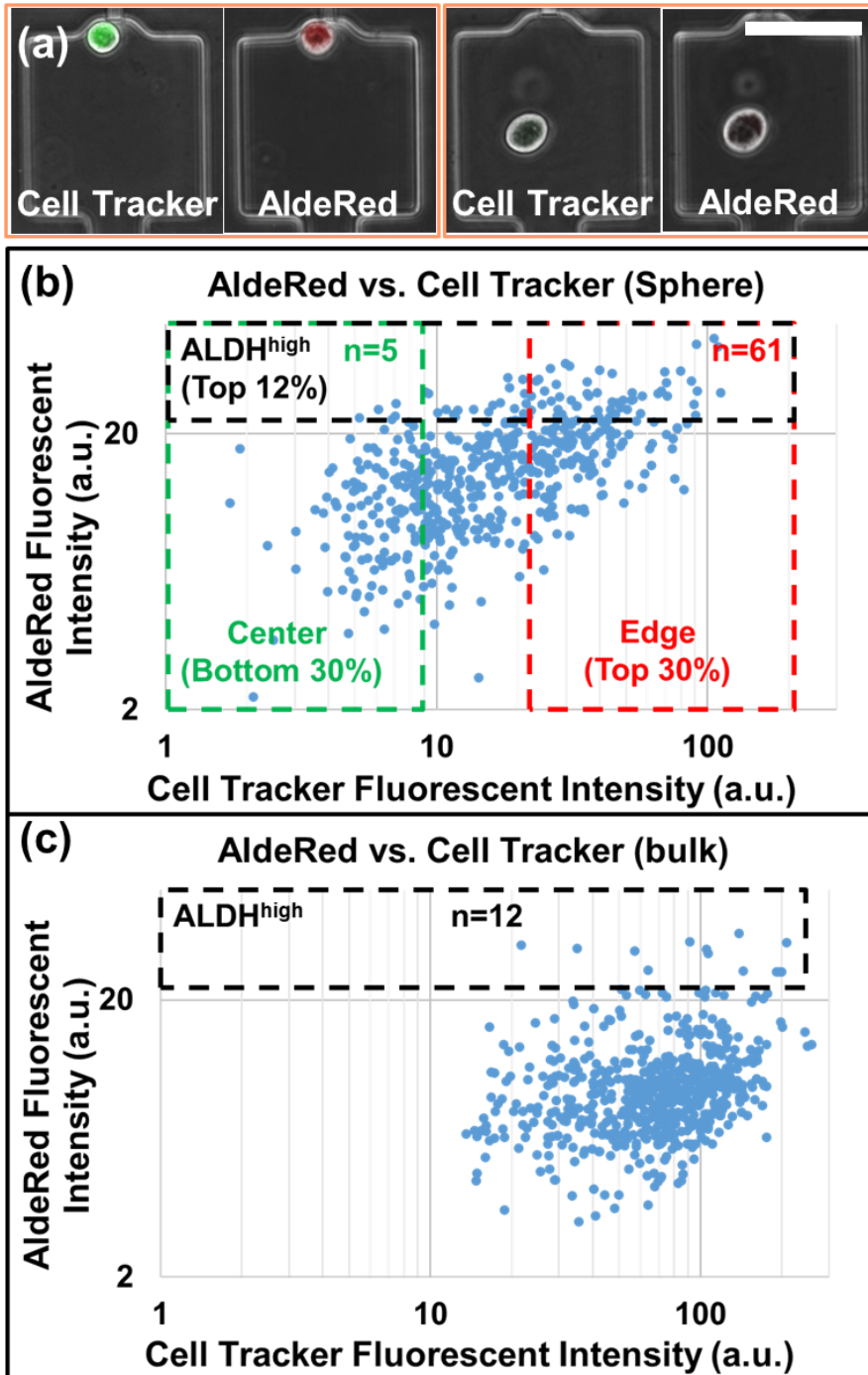


Figure 4-5. Comparison of ALDH activity between sphere leading edge and sphere core. a) Single cell sample images of cell tracker staining and its corresponding AldeRed staining (Scale bar = 100 μ m). b) AldeRed staining on dissociated cancer cells ($N=562$) shows the majority of CSCs are located at sphere leading edge: out of all ALDH^{high} cancer cells, 70 were from leading edge, while only 6 were from center. c) 2D staining control ($N=551$) shows no correlation between AldeRed fluorescence intensity and cell tracker fluorescence intensity.

which was 5/169 (2.96%). However, the ALDH^{high} cell ratio in sphere leading edge was 61/170 (35.9%). This observation of higher percentage of CSC population in sphere leading edge proves that the enrichment of CSCs using sphere assays are mostly originated from the outer part of the spheres.

4.7 Secondary generation sphere formation comparison between leading edge and core

In order to further validate our discovery on CSCs spatial distribution, the dissociated HN13 cells were loaded back to Hi-Sphere chips to compare the 2-GCS rate between cells from sphere leading edge and sphere core (Fig 4-6 (a)). As a result, the 2-GCS formation rate of sphere leading edge was around 2 times higher than that of sphere core (Fig. 4-6 (b)). This result matches well with the ALDH staining outcome and provides a phenotypic evidence on the larger population of CSCs in sphere leading edge.

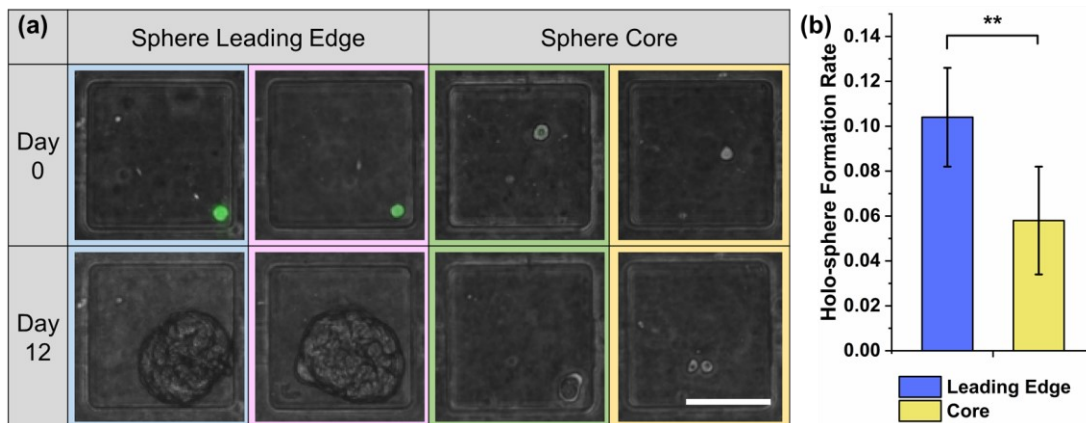


Figure 4-6. 2nd sphere formation rate comparison between leading edge and center. a) sample images of 2nd sphere. b) cells from leading edge shows higher sphere formation rate compared to those from center. (Scale bar = 100 μ m)

4.8 Chapter summary

Like solid tumors, tumor spheres are endowed with a heterogeneous population of cells that can be characterized by functional assays and the expression of distinct molecular markers. The search for new strategies capable of targeting CSCs represents one of the emerging fields in cancer therapy. Sphere-forming assays are valuable tools to enrich CSC population and study the cellular properties. We presented a high-throughput clonal sphere chip suitable for investigating both inter-tumor heterogeneity and intra-tumor heterogeneity. The hydro-dynamic cell capture design guarantees the high percentage of microfluidic chambers initially loaded with single cells. The flipping-chip culture design prevent captured cells from flushed out of the culture chambers, enabling long-term sphere culture with sufficient nutrient supply. We designed a size-based sphere retrieval scheme, which enables effective separation two sub clones, holo-spheres and mero-spheres for downstream inter-sphere heterogeneity analysis. After comparing the secondary sphere formation rates between the two populations, we concluded that holo-spheres contained significantly higher percentage of CSCs . To further explore the location of these CSCs in holo-spheres, we separated cells from sphere leading edge and sphere core using cell tracker fluorescent dye. The diffusion nature of the dye molecules guaranteed that cells from sphere leading edge were more thoroughly stained compared to those from sphere core. After comparing ALDH activity and secondary sphere formation rate, we concluded that the majority of CSCs in holo-spheres were located at the sphere leading edge, while only a small portion of CSCs were from the sphere core. In this work, we demonstrated the high-throughput clonal sphere culture and retrieval capability of Hi-Sphere chip using one head and neck cancer cell line HN13 and one patient-derived cell line, HMC-3B. Using the same experimental protocol, a broader study on multiple cell lines from different origins would be useful in generalize our finding in the location of CSCs. Our sphere

analysis approach also opens up a new opportunity to correlate cell location and genetic profile of each single cell within a clonal sphere, which is important in CSC hierarchy study.

Chapter 5 : Label-free Estimation of Therapeutic Efficacy on 3D Cancer Spheres Using Convolutional Neural Network Image

Analysis

Despite recent advances in cancer treatment, developing better therapeutic reagents remains an essential task for oncologists. To accurately characterize drug efficacy, 3D cell culture holds great promise as opposed to conventional 2D mono-layer culture. Due to the advantages of cell manipulation in high-throughput, various microfluidic platforms have been developed for drug screening with 3D models. However, the dissemination of microfluidic technology is overall slow, and one missing part is fast and low-cost assay readout. In this work, we developed a microfluidic chip forming 1,920 tumor spheres for drug testing, and the platform is supported by automatic image collection and cropping for analysis. Using conventional LIVE/DEAD staining as ground truth of sphere viability, we trained a convolutional neural network to estimate sphere viability based on its brightfield image. The estimated sphere viability was highly correlated with the ground truth (R-value > 0.84). In this manner, we precisely estimated drug efficacy of two chemotherapy drugs, Doxorubicin and Oxaliplatin. We also cross-validated the trained networks of two drugs and found common brightfield morphological features indicating sphere viability. The discovery suggests the potential to train a generic network using some representative drugs for applying to many different drugs. The brightfield estimation of sphere viability saves LIVE/DEAD staining reagent cost and fluorescence imaging time. In addition, the presented

method allows viability estimation in a label-free and non-destructive manner. In short, with image processing and machine learning, the presented method provides a fast, low-cost, and label-free method to assess tumor sphere viability for large-scale drug screening in microfluidics.

5.1 Introduction

Cancer is a major burden of disease in most developed countries. Just within the United States, it was estimated to have 1,735,350 new cases of cancer being diagnosed, and 609,640 people passed away caused by the disease in 2018 [1]. Despite advances in cancer treatment, developing better therapeutic reagents is still essential to help patients. While animal models cannot fully recapitulate situation of treating patients, they have been widely used for drug development over the past decades [2, 3]. Given drug testing in animals has better physiological relevance, it is costly and time-consuming. As compared to animal testing, drug testing in cell culture has significant advantages of low cost and quick turnaround time, so it serves as an important validation step before animal studies. For simple 2D monolayer model, cancer cells are placed on a polystyrene or glass substrate, treated by drugs for a few days, and then examined to measure therapeutic efficacy. While the drug screening in 2D has been developed as a low-cost and high-throughput technique, limited relevance between 2D culture and animal model makes it less desirable nowadays [4]. 3D culture allowing cancer cells to form tumor spheres in suspension or hydrogel can better mimic the profile of drug exposure, nutrients, and oxygen supplies in real tumor [4, 5]. Given 3D sphere model is more complicated than 2D monolayer culture, it is emerging in cancer drug discovery and screening as a more advance model [6-8].

To precisely control the size and environment of 3D spheres for high-throughput drug testing, microfluidic technology has numerous advantages. Unlike cell cultured in conventional well-plates or polystyrene dishes, microfluidic chips provide capabilities of cell manipulation and maintain a well-controlled environment for cell growth in 3D [9, 10]. With micro-fabrication capability, thousands of micro-chambers can be implemented on a chip for high-throughput screening [11, 12]. Cells can be spontaneously loaded into all micro-wells with good uniformity, making microfluidics much less labor-intensive as compared to conventional well-plates [13-20]. However, while there are many microfluidic platforms aiming to drug screening applications [13, 14, 21-23], the adoption of microfluidics in large-scale drug screening is slow. One major bottleneck is the lack of fast and low-cost readout method for drug screening using microfluidic 3D culture system.

To measure drug efficacy, various cell viability assays have been developed [24]. The fluorescence-based LIVE/DEAD staining is composed of two components. The LIVE fluorescent reagent (e.g. Calcein AM) can be activated by intracellular esterase enzymatic activity to indicate viable cells. The DEAD fluorescent reagent (e.g. Ethidium homodimer-1) can diffuse through compromised cell membrane to stain nucleic acid, so DEAD staining can indicate loss of cell membrane integrity in dead cells. The LIVE/DEAD staining method, which marks viability of individual cells, is especially useful in flow cytometry. However, there are several drawbacks when using LIVE/DEAD staining in 3D models. (1) Light absorption, scattering, and poor penetration can deteriorate image quality of 3D sphere/tissue. (2) Fluorescence imaging usually takes several hundred milliseconds exposure time for each image. As compare to brightfield microscopy exposed by a few milliseconds, the imaging throughput is significantly lower by orders of magnitude. (3) LIVE/DEAD staining reagents are costly for large-scale drug screening. (4)

Cytotoxicity of staining makes it only suitable as an end-point assay. There are other more dedicated cell viability assays measuring caspase (e.g. CellEvent™) to indicate apoptotic cells or generating luminescent readout from ATP (e.g. CellTiter-Glo), yet they still suffer from high cost and potential cytotoxicity. Colorimetric assays (e.g. MTT and XTT) monitoring the metabolic function of cells is a fast and cheap alternative to assess cell viability. Healthy cells can reduce tetrazolium-based dye to purple formazan, yet dead cells lose the ability to convert MTT to formazan. Thus, colorimetric change caused by light absorbance of formazan product can be an indicator of cell viability [24]. This method is good for its low cost and easy readout using a plate reader, yet it is hard to distinguish effects of reduced cell number from reduced cellular metabolic activity by examining all cells in bulk. Its cytotoxicity is a concern for continuous monitoring. In addition, monitoring the metabolic function by MTT or XTT requires a large number of cells and reagents to accumulate significant colorimetric change. It works well in conventional static well-plates, yet not favorable for microfluidic platforms having smaller number of cells in perfusion culture [25].

Recent advances in machine learning have enabled analysis of biomedical images in a high-throughput manner. An increasing number of research works paired microfluidic devices with machine learning tools to realize system automation and rapid data analysis. Specifically, microfluidic flow cytometer was assisted with pre-extracted and trained cellular shape feature recognition [26]. It was also reported a phenotypic biomarker assay using machine learning algorithms to predict post-surgery adverse pathology states clinically [27]. In addition, status of cell cycle could be classified in a high-throughput and accurate approach [28,29]. The subcellular features were also recognized and classified using deep learning tool kits [30]. More interestingly, different fluorescence labels such as cell nuclei and cell type can be predicted using unlabeled

transmitted-light images [31]. Those previous works suggest the possibility to develop a low-cost, fast, and non-destructive method for quantifying 3D tumor sphere viability with machine learning. In this work, we present a microfluidic chip that can form 1,920 tumor spheres for testing 6 drug conditions on a chip. The micro-chambers containing spheres were cropped for analysis automatically, so we efficiently collected brightfield images and their drug inhibition scores from conventional LIVE/DEAD staining. With this database, we developed and trained a convolutional neural network (CNN) model to correlate sphere brightfield images with their drug inhibition scores. Thus, the machine learning model can judge drug inhibition of a tumor sphere only using its brightfield image. In this manner, we can accurately estimate the half-maximal inhibitory concentration (IC₅₀) of chemotherapy drugs by brightfield microscopy alone. More interestingly, we found there are common morphological features indicating sphere viability across different drugs, suggesting the potential to train a generic model for drug screening. The presented method provides an automatic, high-throughput, low-cost, and label-free method to assess tumor sphere viability in microfluidics for large-scale drug screening.

5.2 Design of the cancer sphere platform

The presented microfluidic cancer drug screening platform is composed of 6 identical tumor sphere culture sections on a chip. Each section is composed of 320 (an array of 10 columns by 32 rows) units of sphere culture chambers and the inflow and outflow channels (Fig. 5-1 (a, b)). The inflow channels are connected to an inlet reservoir, and the outflow channels are connected to an outlet reservoir. The sphere culture chamber (100 μm in height) is 400 μm in diameter surrounded by a ring of gap supported with micropillars structure (5 μm in height) (Fig. 5-1 (c)).

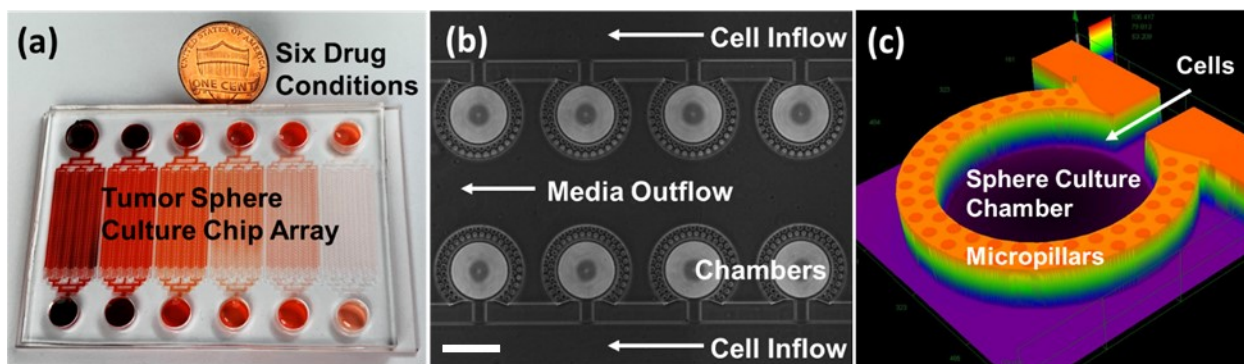


Figure 5-1. Tumor sphere chip and culture chamber. (a) The photo of a cancer sphere chip for drug screening. The chip can test 6 drug concentrations side-by-side for the estimation of IC50. For each condition, it has 320 chambers for sphere culture. (b) A microscope image showing 8 tumor sphere culture chambers with inflow and outflow channels. Cells flow through inflow channels into sphere chambers. As the cell diameter is larger than the gap supported by micropillars, cells are trapped in the sphere culture chambers. The culture media carrying cells can flow out through outflow channels. (Scale bar: 400 μm) (c) Laser confocal microscopy image of a unit chamber measured by Olympus OLS 4000 LEXT.

After bonded with a piece of blank PDMS on top, there is a 5 μm gap between the two layers of PDMS. These gaps between the micro-pillars structure can trap cells in the sphere culture chambers, while allowing culture media to outflow. By properly balancing the flow resistance using tapered inflow channels as described in previous work [32], we are able to uniformly load cancer cells into each sphere chamber. To facilitate sphere aggregation by gravity, we applied an additional layer of photoresist (16 μm in height) to create a rounded substrate in the sphere culture chamber [13,15]. The platform design was adapted from our previous work with the improvement of high number of sphere culture chambers per condition [13]. In addition, the chamber was designed to be circular, so it would be easy to crop by an image processing program.

Using the presented cancer sphere platform, we can reliably form large number (1,920 spheres per chip) of cancer spheres for drug screening. Due to consistent number of cells loaded

per chamber, the spheres formed are uniform in size (diameter: $214 \pm 21 \mu\text{m}$, $N = 100$, \pm indicates standard deviation (S.D.)). The method is more effective than conventional low-attachment well-plate, which forms spheres with different sizes in the wells. As cancer sphere size can affect the diffusion of drug and nutrients, the uniformity of sphere is critical for reliable and reproducible drug testing [38]. In addition, media can be easily exchanged by aspirating and then replenishing fresh media in the inlets/outlets. The isolated cancer spheres in chambers will not be disturbed by media exchange process to aggregate together undesirably. To handle a large amount of images generated by our platform, we developed a custom MATLAB program. The automatic cell cropping function can reliably recognize circular chambers and crop them for further data analysis and machine learning (Fig. 5-2 (d)).

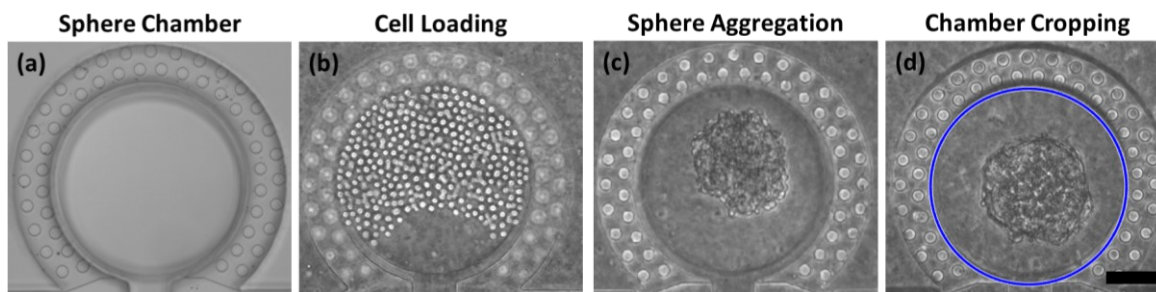


Figure 5-2. Cell loading in a sphere chamber and sphere aggregation. (a) An empty cancer sphere chamber before cell loading. (b) SUM159 breast cancer cells were loaded in the cancer sphere chamber. (c) Cells aggregated to a cancer sphere after 2 days. (d) Automatic chamber cropping program cropped the circular chamber regions (blue circles) for further image processing and machine learning. (Scale bar: $100 \mu\text{m}$)

5.3 Morphological changes of spheres after drug treatment

After cancer spheres aggregated in the chambers, drug treatment was performed on-chip. In this work, we tested two chemotherapy drugs, Doxorubicin and Oxaliplatin. For each drug, six

different concentrations across a wide range were applied for 3 days following previous protocols [13, 39], so IC50s of drugs could be estimated. The spheres treated by Doxorubicin with different concentrations were demonstrated as in Fig. 5-3. For the conditions of low dose (no drug, 0.05 μM , and 0.25 μM), small number of cells were dead as indicated by sparse red fluorescence (DEAD staining) dots. Both brightfield and green fluorescence (LIVE staining) images show consistent healthy morphology. For the intermediate drug concentration of 1 μM Doxorubicin, we observed strong red fluorescence signal in the peripheral region of sphere, suggesting outer cancer cells were killed. At the same time, there was a strong green fluorescence signal inside the sphere, indicating that inner cells of sphere were still alive. The interesting part is that brightfield image suggests the same situation. While there are some dark apoptotic cells around sphere surface forming a dark blurry ring, the center of sphere looks similar to the morphology of healthy spheres. When applying

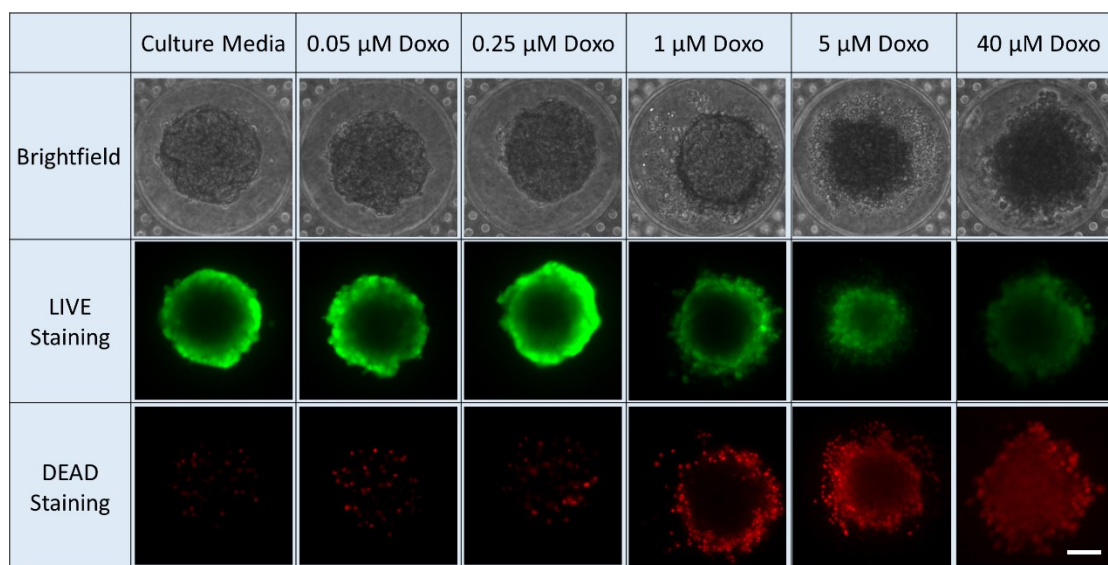


Figure 5-3. Cancer spheres treated by Doxorubicin. Representative images of SUM159 cancer spheres treated by Doxorubicin with six different concentrations. LIVE/DEAD staining was used to quantify sphere viability. FITC green fluorescence image represents the live cells, and TRITC red fluorescence image represents dead cells. With the increase of drug concentration, green fluorescence intensity decreases and red fluorescence intensity increases. The brightfield morphology also changes with different drug treatments. (Scale bar: 100 μm)

high dose of 5 μM and 40 μM Doxorubicin, we found a large number of dead cells inside the core of sphere as indicated by disseminated red fluorescence signal. Similarly, brightfield image shows dark dead cells throughout the sphere. Using Doxorubicin treatment as an example, we demonstrate that the sphere viability indicated by fluorescence-based LIVE/DEAD staining can be correlated with brightfield sphere morphology. Those observations support the feasibility of sphere viability estimation based on brightfield image.

5.4 Estimation of cancer sphere viability using brightfield microscopy

As suggested in previous section, while brightfield images present differences between healthy and unhealthy tumor spheres, human beings cannot quantify sphere viability based on qualitative observation of morphology. For precise quantification of sphere viability based on its brightfield image, we developed a convolutional neural network model. The CNN model was trained using brightfield images as input and drug inhibition score determined by LIVE/DEAD staining or treatment condition as expected output. After training, we first validated that the model can accurately predict the treated drug concentration using brightfield images. Green boxes represent correct prediction cases, which significantly outnumber the wrong cases in red boxes (Fig. 5-4 (a)). As spheres treated by low Doxorubicin dose (no drug, 0.05 μM , and 0.25 μM) were indistinguishably viable, we pooled those three conditions as a group. In this case, we got a high accuracy of 94.7% (Fig. 5-4 (a)). For six-condition classification, the accuracy was 80.4% (Fig. 5-5). As expected, the lower accuracy was caused by confusion between no drug control and low-dose treatment. It was also relatively difficult to predict the spheres treated by 1 μM Doxorubicin

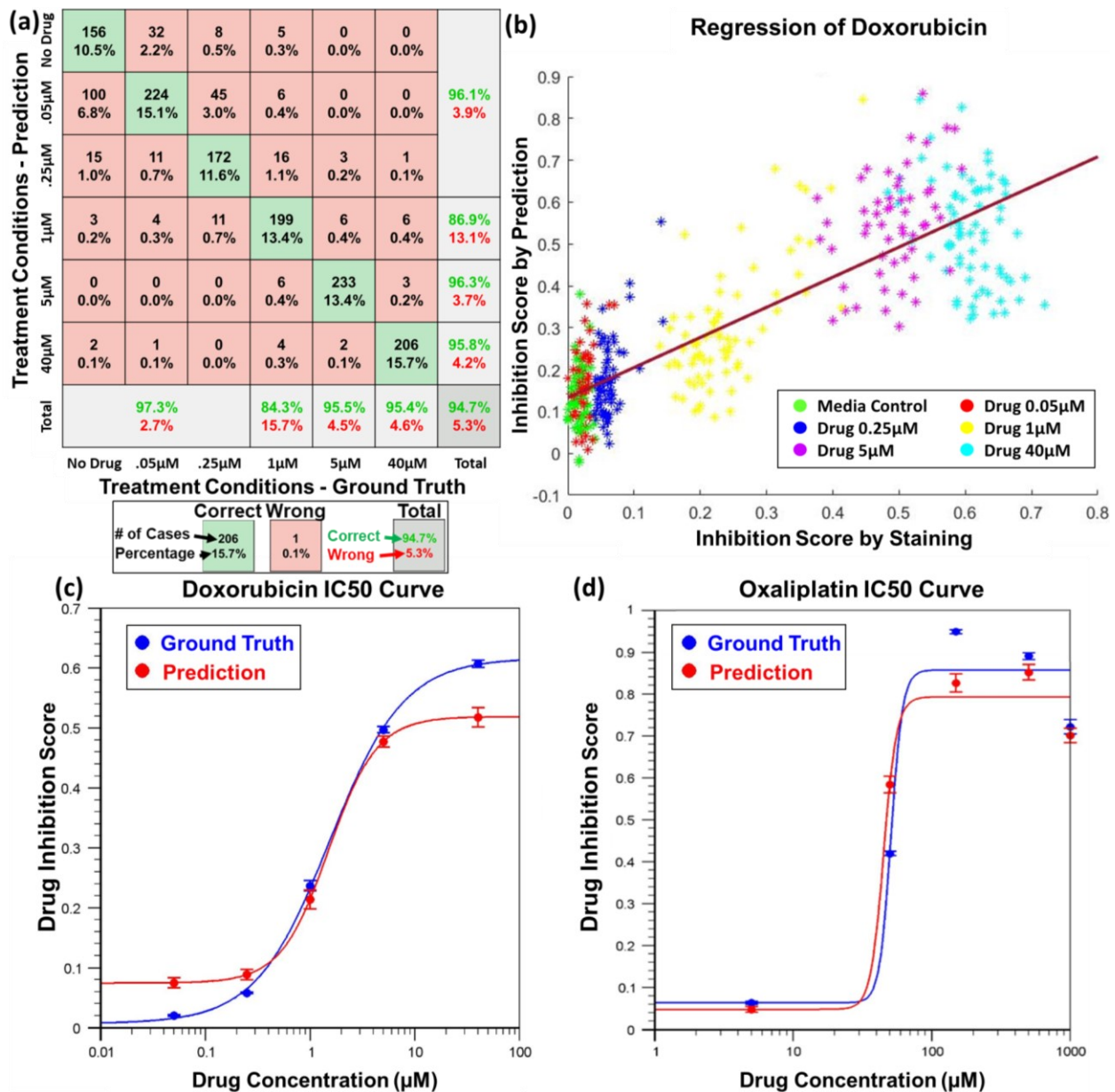


Figure 5-4. Cancer spheres classification and drug inhibition score regression using brightfield image and CNN model. (a) Doxorubicin treatment classification accurately (94.7%) predicts the drug treatment concentration based on its brightfield image. The green boxes represent correct prediction, the red boxes represent wrong prediction, and the grey boxes represent summation of a row/column. Both number of prediction cases and percentage are described in the box. The boxes in a column belongs to spheres treated by the same concentration, and the boxes in a row belongs to spheres predicted to be treated by the same concentration. The first three classes were combined since those drug concentrations are much lower than the IC50 transition point, so hard to distinguish even with LIVE/DEAD staining. (b) Prediction of drug inhibition score using the trained CNN model. X-axis represents the ground truth of inhibition score measured by LIVE/DEAD staining, and Y-axis represents drug

inhibition score predicted using brightfield image with the trained CNN model. Each dot represents a sphere, and different colors mean different drug concentrations. The R-value of linear regression is 0.84, indicating a strong correlation between the ground truth and prediction. (c, d) Drug efficacy IC50 curves of two chemotherapy drugs. X-axis represents drug concentration, and Y-axis represents drug inhibition score. Blue curve is plotted based on the ground truth measured by LIVE/DEAD staining, and red curve is plotted based on the prediction using brightfield images. Error bars indicate standard deviation (S.D.). (c) Drug efficacy IC50 curves of Doxorubicin treatment on cancer spheres. The estimated IC50 based on LIVE/DEAD staining is 1.7 μ M, and the estimated IC50 based on brightfield images is 1.6 μ M. (d) Drug efficacy IC50 curves of Oxaliplatin treatment on cancer spheres. The estimated IC50 based on LIVE/DEAD staining is 51 μ M, and the estimated IC50 based on brightfield images is 47 μ M.

(accuracy: 84.3%). Since 1 μ M Doxorubicin was close to IC50, it was expected to generate a larger variation in morphology, making it more challenging to predict. As compared to tricky situations, high prediction accuracy (around 95%) was achieved for spheres treated with high dose of Doxorubicin. We also examined the prediction of drug inhibition score based on brightfield images in Fig. 5-4 (b). The drug inhibition scores determined by LIVE/DEAD staining and predicted by brightfield images with CNN model were highly correlated with a correlation coefficient R of 0.84 (Fig. 5-4 (b)). In addition to Doxorubicin, we tested another chemotherapy drug, Oxaliplatin. After training the model as we did for Doxorubicin, we got an even higher correlation coefficient R of 0.89 (Fig. 5-6). Using the prediction model, we sampled 20% of cancer spheres for the estimation of IC50. Fig. 5-4 (c, d) demonstrates that the IC50 curves fitted by ground truth (LIVE/DEAD staining) and CNN prediction model are similar. For the two drugs we tested, the mean difference of IC50s estimated by ground truth and CNN prediction is 7% (6% for Doxorubicin and 8% for Oxaliplatin). In literature, we could not find the IC50 of Doxorubicin and Oxaliplatin using exactly the same treatment condition and cell line, yet the measured IC50 in this work is comparable with reported IC50 of relevant breast cancer cell lines [40, 41]. The accurate IC50 estimation validates the presented label-free method to estimate sphere viability based on its brightfield image.

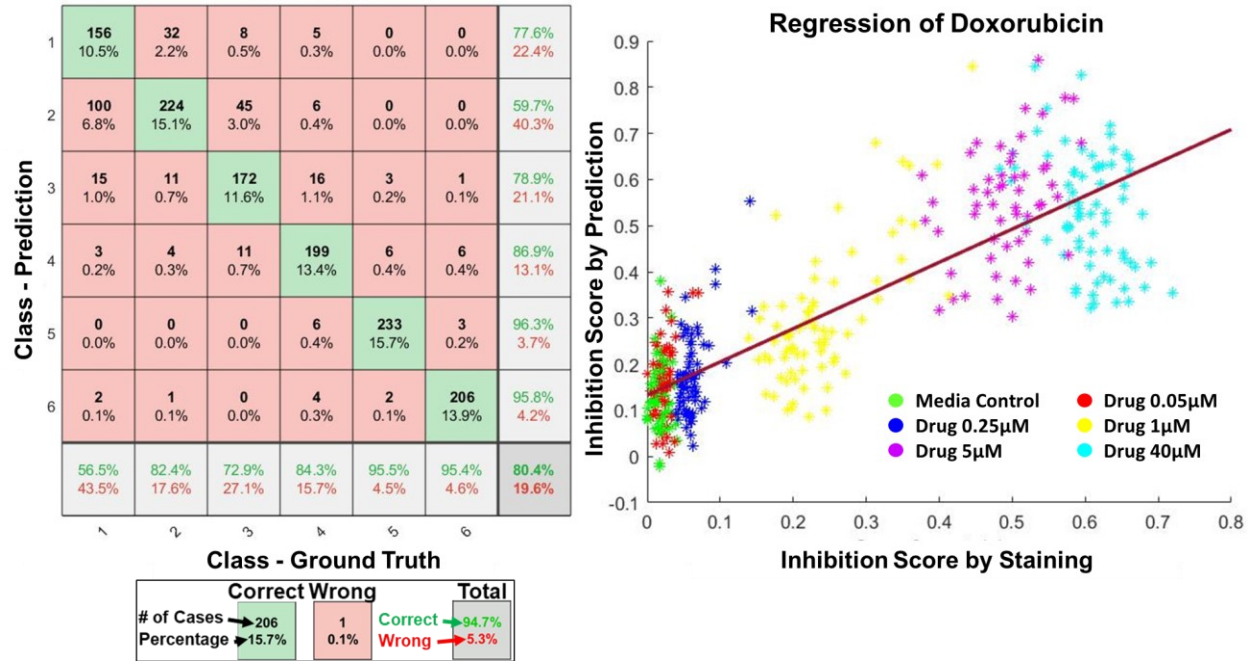


Figure 5-5. Cancer spheres classification and drug inhibition score regression for Doxorubicin (a) Six-class classification accurately (80.4%) predicts the drug treatment concentration based on its bright-field image. (b) Regression of sphere inhibition score using the trained CNN model. X-axis represents the ground truth of inhibition score measured by LIVE/DEAD staining, and Y-axis represents drug inhibition score predicted using bright-field image and trained model. Each dot indicates a sphere, and different colors mean different drug concentrations. The R-value of this linear regression is 0.84, indicating a strong correlation between the ground truth and our prediction.

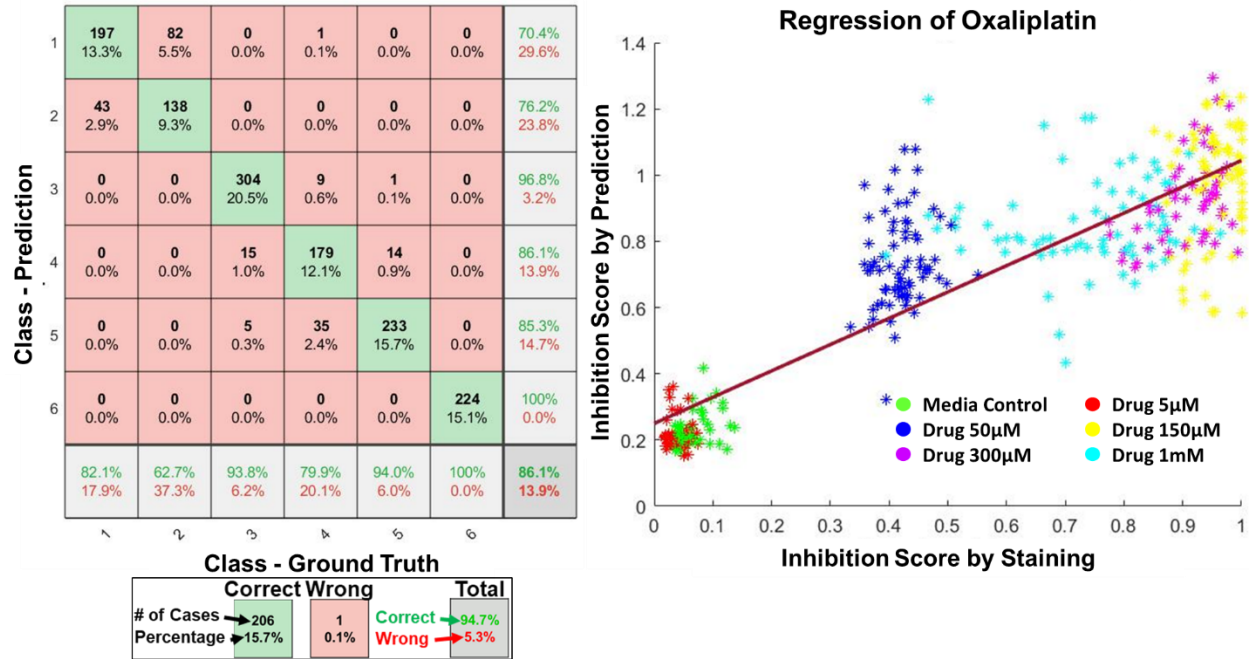


Figure 5-6. Cancer spheres classification and drug inhibition score regression for Oxaliplatin (a) Six-class classification accurately (86.1%) predicts the drug treatment concentration based on its bright-field image. (b) Regression of sphere inhibition score using the trained CNN model. X-axis represents the ground truth of inhibition score measured by LIVE/DEAD staining, and Y-axis represents drug inhibition score predicted using bright-field image and the trained model. Each dot indicates a sphere, and different colors mean different drug concentrations. The R-value of this linear regression is 0.89, indicating a strong correlation between the ground truth and our prediction.

5.5 Critical morphology features for sphere viability prediction

While it is known that CNN filters are difficult to interpret [42], we would like to visualize them to understand the key features distinguishing healthy and unhealthy spheres (Fig. 5-7 (a)). We used a representative brightfield sphere image (Fig. 5-7 (e)) as the input and processed it by all filters for visualization. Fig. 5-7 (b-d) demonstrates 64 filters in the first convolutional layer, 32 filters in the second convolutional layer, and 16 filters in the third convolutional layer, respectively. As expected, we found some relevant features in the filters of the first convolutional

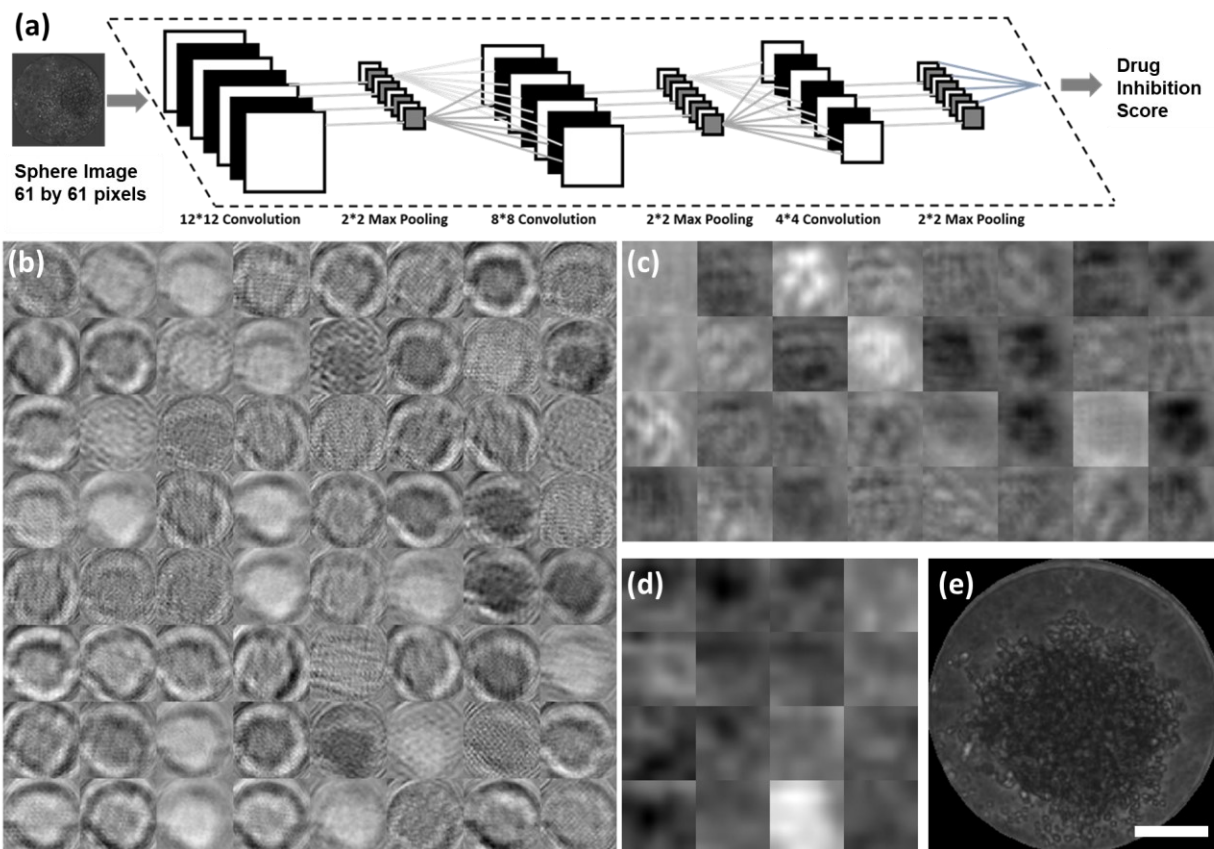


Figure 5-7. Neural network structure and trained filters for prediction (a) The 3-layer structure of neural network. (b-d) After processing a representative sphere image, the critical features are enhanced by filters of each convolutional layer in the neural network. The features are related to central darkness, sphere outline, and texture of cancer spheres. Each small square represents a filter. (b) The 64 filters in the first convolutional layer. (c) The 32 filters in the second convolutional layer. (d) The 16 filters in the final convolutional layer. (e) The input representative sphere image. (Scale bar: 100 μm)

layer. The majority of filters highlight the center of the image, where most spheres are located (Fig. 5-7 (b)), suggesting that trained filters catch spheres rather than background for prediction. Specifically, we can see three interpretable features: (1) bright (healthy)/ dark (unhealthy) center indicating sphere viability, (2) smooth (healthy)/ rough (unhealthy) outline of tumor spheres, and (3) strips/dots picking up different textures of cell spheres [43]. All those relevant features are also used by human beings to distinguish healthy and unhealthy spheres. For the second and the third

convolutional layers, filters show more abstract and high-order features that are difficult to interpret (Fig. 5-7 (c, d)). However, an interesting observation is that the microfluidic chamber outline diminishes in the second and the third layers, indicating that the tumor sphere itself rather than background noise pattern contributes to the classification and prediction results.

5.6 Inter-drug model validation and mixed prediction for different drugs

After demonstrating good prediction for individual drugs, we explored whether the model trained by one drug can be used for the prediction of another drug. As many chemotherapy drugs are associated with DNA damage to induce cell apoptosis, including Doxorubicin and Oxaliplatin, we expect there are some similarities in mechanism and resulting sphere morphology [44,45]. Here, we used the model trained by Doxorubicin data for the prediction of Oxaliplatin images in Fig. 5-8 (a). We found that the model can make good prediction for relatively healthy spheres (inhibition score < 0.5), yet the model is less accurate to handle totally dead spheres (inhibition score > 0.75). This situation can be explained by the fact we did not get totally dead spheres by Doxorubicin treatment. Thus, Doxorubicin model is inexperienced with those totally dead spheres. While the Doxorubicin model is not perfect for Oxaliplatin, it still yields a good correlation coefficient of 0.82. Due to this encouraging preliminary results, we further pooled together the databases of two drugs for training a new model. With this new model covering a wide range of inhibition score from 0 to 1, we made a better prediction with a correlation coefficient of 0.93 (Fig. 5-8 (b)). The results suggest that unhealthy spheres inhibited by different drugs share a similar set of morphological features. The existence of generic features is very encouraging, meaning the model

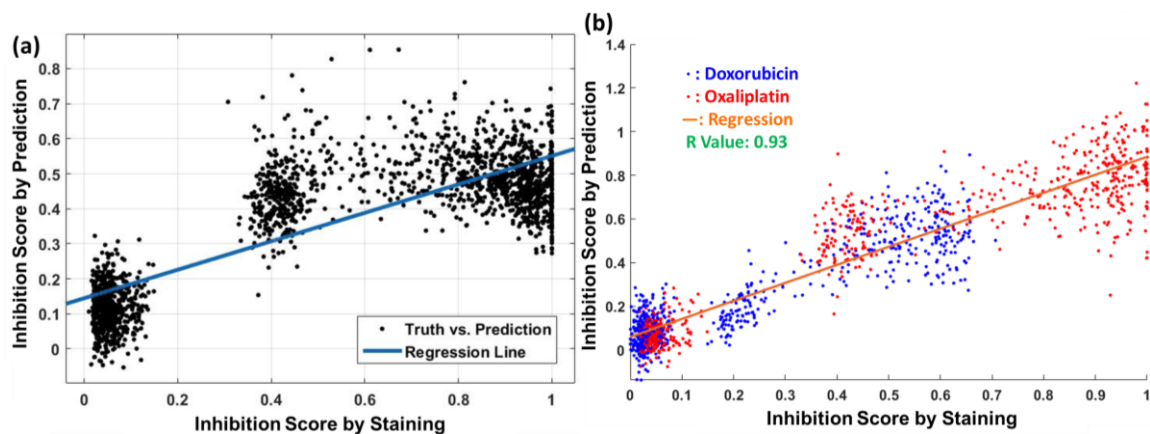


Figure 5-8. Inter-drug model validation and prediction model combining different drugs. (a) CNN model trained by Doxorubicin treated spheres was used for predicting the drug inhibition scores of Oxaliplatin treated spheres. X-axis represents the ground truth of inhibition score measured by LIVE/DEAD staining, and Y-axis represents drug inhibition score predicted using brightfield images with Doxorubicin trained model. Each dot represents a sphere. The R-value for linear regression is 0.82 showing a strong correlation between the ground truth and prediction. (b) Tumor spheres treated by Doxorubicin and Oxaliplatin were combined for training and prediction. Each dot represents a sphere, and different colors mean different drug treatments. The R-value of linear regression is 0.93, which is even higher than prediction of individual drugs.

trained from some representative drugs can potentially be applied widely in large-scale drug screening.

5.7 Chapter summary

Exploration for better therapeutic reagents is a prolonged quest in cancer research, and the advance in microfluidic technologies facilitates more relevant 3D cell culture models and higher throughput for drug development. While microfluidics is emerging in drug studies, it has been hampered by lack of automatic, fast, and low-cost readout methods. In this work, we developed a high-throughput 3D cell culture platform growing 1,920 cancer spheres on-chip. The cancer sphere

images can be collected by programmed software and then automatically cropped for analysis. More importantly, we developed a novel method to precisely estimate cancer sphere viability using brightfield images based on a trained convolutional neural network. In this manner, we performed drug testing using two chemotherapy drugs (Doxorubicin and Oxaliplatin) on SUM159 breast cancer cells. The estimated drug inhibition score using brightfield images is highly (correlation coefficients > 0.84 for both drugs) correlated with that measured by conventional fluorescence-based LIVE/DEAD staining. As compared to LIVE/DEAD staining, the differences in IC₅₀ for both drugs are within 8%. When examining the filters in the trained CNN model, we identified the morphologies reflecting dark center and rough outline of unhealthy tumor spheres, matching well with the features used by human beings. With this capability, we can avoid struggling with LIVE/DEAD staining assay, which is slow and costly. In addition, the presented method relies on brightfield image alone, so it enables non-destructive (without the toxicity caused by cell viability staining) estimation of cell viability in real time. The method can potentially be used for studying the time dynamics of cancer cell death during drug treatment, helping us optimize treatment dose and frequency. In short, by incorporating machine learning with microfluidics, we present a highly automatic method for analyzing drug testing results. The automatic and low-cost readout method will help the dissemination of microfluidic 3D culture in drug screening, and the presented workflow can be widely applied to other cell biology assays.

Chapter 6 : Morphology-based Prediction of Cancer Cell Migration Using Artificial Neural Network and Random Decision Forest

Metastasis is the cause of death in most patients of breast cancer and other solid malignancies. Identification of cancer cells with highly migratory capability mainly relies on marker-based approaches, which are limited by inconsistencies among patients, types of cancer, and cancer states. Alternatively, machine learning has been applied in many research areas with good performance. However, machine learning has not yet been applied to analysis of cancer migratory behaviors.

Combining microfluidic single-cell migration chip and high-content imaging, we extracted morphological features and recorded migratory direction and speed of breast cancer cells. By applying Random Decision Forest (RDF) and Artificial Neural Network (ANN), we achieved over 99% accuracy for cell movement direction prediction and 91% for speed prediction. Unprecedentedly, we identified highly motile cells and non-motile cells based on microscope images and machine learning model, and pinpointed and validated morphological features determining cell migration, including not only known features related to cell polarization but also novel ones that can drive future mechanistic studies. Predicting cell movement by computer vision and machine learning establishes a ground-breaking approach to analyze cell migration and metastasis.

6.1 Introduction

Metastasis is the leading cause of mortality in patients with breast cancer, being responsible for over 40,000 deaths per year in the US. Despite advances in early detection and treatment, once metastases develop, breast cancer is incurable [1, 2]. Cancer cells with enhanced motility and invasiveness migrate away from the primary tumor site and initiate the metastatic process [1]. Therefore, identifying key aspects for cell migration is crucial for understanding and ultimately overcoming metastasis. Currently, considerable efforts have focused on elucidating mechanisms that govern epithelial-to-mesenchymal-transition (EMT), a developmental program in which epithelial cells acquire migratory and invasive phenotypes to promote metastasis. In recent decades, various EMT biomarkers including membrane proteins (e.g. E-CAD, N-CAD), cytoskeletal markers (e.g. Vimentin, Cytokeratins), transcriptional factors (e.g. Snail, Slug, ZEB1, ZEB2, Twist) were developed [3-5]. However, these and other markers for defining EMT underscore problems of marker-based approaches across multiple cancers: 1) cancer cells undergo differing extents of partial EMT; 2) multiple sets of markers have been used to define EMT even within a single type of cancer; 3) markers are inconsistent across different malignancies [3]. Inconsistencies of existing EMT markers highlight the need for new approaches to identify highly migratory cells.

Not only does the recent development of Artificial Intelligence (AI) and computer vision provide a potent alternative to define cell properties based on morphology, but also use of fluorescent probes and reporters to label proteins, protein activity, and organelles has advanced our ability to study mitochondria. Mitochondrial morphology correlates with metabolic state, drug response, and cell viability, providing potential insights into overall status and function of cells [6-8]. Advances in computer technology now allow high-content images of mitochondria to be processed by the computer vision program [9,10]. After training on data sets, the computer vision

software can autonomously interpret meanings of images and classify cells based on imaging features. Various algorithms such as Random Decision Forests [11] (RDFs construct decision trees in training and make decisions based on voting of trees) and Artificial Neural Networks (ANNs build a group of nodes interconnected with weighted linkage in training and classify things accordingly) [12] were developed. However, people so far have only analyzed single imaging features using small numbers of cells to investigate correlations between the distribution of mitochondria and cell movement [13]. Cutting-edge computer vision techniques were not used to fully explore the potency of morphological features in determining cell migration direction and speed.

In addition to imaging analysis capability, an effective cell monitoring scheme is also critical to the success of comprehensive cell morphological analysis. Microfluidic technology has emerged as a state-of-the-art approach for cell biology because of precise manipulation of single cells and high potential in scaling [14-16]. As compared to tracking cells randomly seeded in a dish, cells in a microfluidic chip are precisely positioned and easily tracked in a high-throughput manner. Thus, the migration distance of individual cells can be accurately measured to correlate with its morphology. More importantly, chemoattractant gradients can be generated on-chip to model chemotaxis in cancer metastasis. Hence, we applied the high-throughput cell migration chip we have previously developed for this study [17].

In this work, we present a comprehensive morphological analysis using cutting-edge computer vision methods including random decision forests and artificial neural networks to establish the correlation between cellular morphological features and cell movement direction and speed. We first collected 1,358 cellular and mitochondrial images and then trained and optimized the machine learning model. Using the model we built, we successfully predicted the migration

direction for more than 99% of cells and picked out highly-motile cells (top 10% fast-moving cells) and non-motile cells (top 10% slow-moving cells) with 91% accuracy. Based on the prediction, we identified critical morphological markers determining cell movement direction and speed. To validate the importance of markers we found, we impaired cell movement using commonly used chemotherapeutics as well as sorted highly migratory cells from the bulk population for comparison. Both experiments validated the importance of identified morphological features in determining cell movement. The presented work represents a new method to predict and understand the cell migration process, which will advance studies of mechanisms driving cell migration.

6.2 Morphological prediction of cell migration pipeline

In order to discover and validate morphological features that contribute to migration, we developed a workflow including 4 steps: experiment, image processing, machine learning, and validation (Fig. 6-1). Firstly, the microfluidic migration chip provided single-cell resolution for cellular morphological analysis. After 6 hours of incubation time, fluorescence microscopy was used to obtain 40X high-content images of both the mitochondria and cell profile. After implementing image pre-processing procedures Based on pre-processed images, we implemented single-cell segmentation and a Random Decision Forest (RDF) classifier for mitochondrial classification, in which all the pieces of mitochondria in each single cell were sorted into three categories: fiber, intermediate, and dots [6], with important morphology features including major axis, area, and aspect ratio. The distribution of mitochondrial types was then applied as one of the 61 extracted cellular morphological features (Supplementary information). Using these features

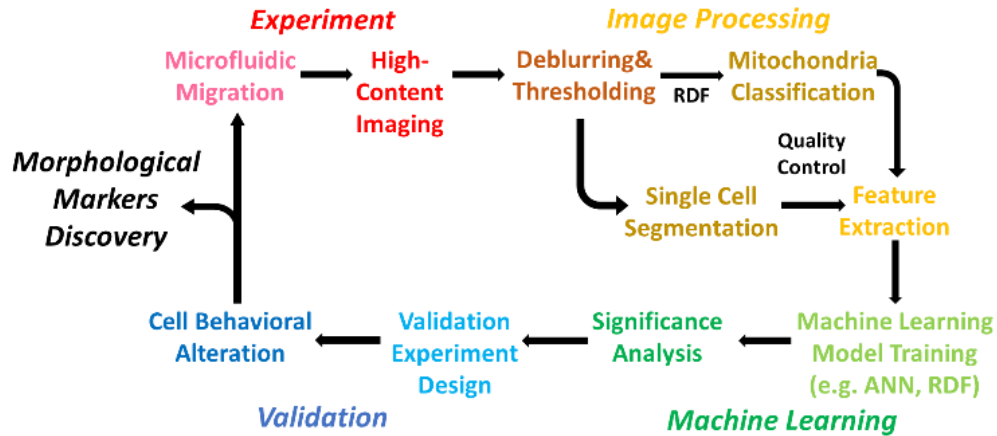


Figure 6-1. Workflow of critical morphological features discovery in cell migration, which includes microfluidic migration chip experiments, high-content imaging, image processing, machine learning modelling, and control experiment validation.

from both cellular morphology and mitochondria profiles as inputs, we trained two machine learning models to predict cell migration direction and cell migration speed. The Random Decision Forest (RDF) and Artificial Neural Network (ANN) achieved 99.6% and 91.0% accuracy, respectively. More importantly, we were also able to pinpoint significant morphological features critical to migration behavior based on the predictor importance analysis from the RDF classifier. By performing control experiments, we validated that our discovered morphological markers are highly correlated with cancer cell migration.

6.3 Microfluidic single cell migration chip design and cell migration experiment

In order to accurately quantify the moving speed of individual cancer cells, we loaded the cell suspension into a microfluidic migration chip (Fig. 6-2 (a)), which consisted of 2×450 individual narrow migration channels divided into an upper half and lower half. A total of three

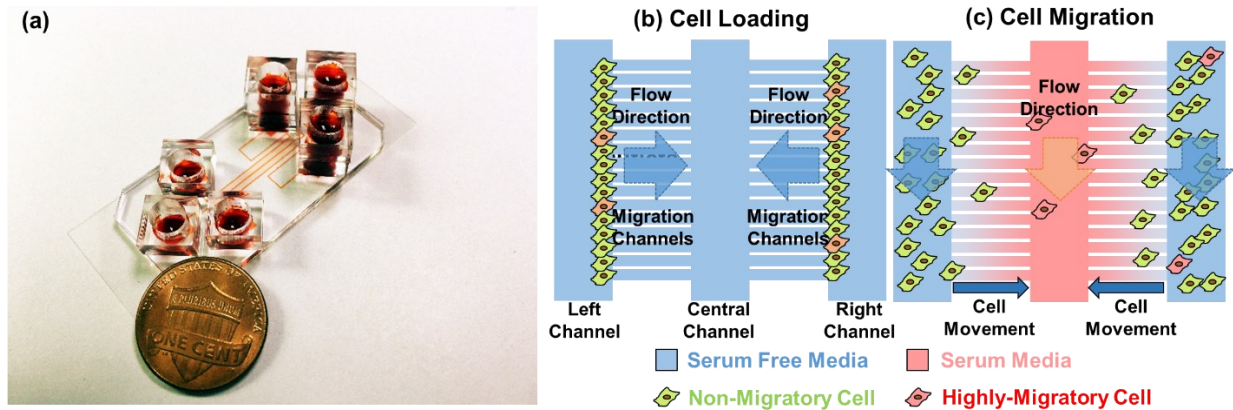


Figure 6-2. Microfluidic migration chip overview. (a) Photograph of a migration device with a one-cent coin, depicting the 3 inlets and 3 outlets reservoirs with red dye flowing through each device. The serpentine loading channels can be seen running vertically, with the horizontal migration channels running perpendicularly between them. (b) Cells were loaded along both left side and right side of the vertical cell loading channels and (c) migrate through the horizontal migration channels due to chemoattraction.

inlets and three outlets are deployed on the chip as the loading interface. Cancer cells were loaded to the inlets on both upper and lower sides and allowed to migrate towards the center with serum as the chemoattractant (Fig. 6-2 (b)). The migration channels were designed to be $1000 \mu\text{m} \times 30 \mu\text{m} \times 5 \mu\text{m}$ ($L \times W \times H$). The dimension of the cross-section is small enough that only single cells could be positioned in each channel, while the migrating direction was also confined to the orientation of the migration channels (Fig. 6-2 (c)). The migration devices were fabricated from a single layer of PDMS (Polydimethylsiloxane, Sylgard 184, Dow Corning), which was fabricated on a silicon substrate by standard soft lithography, and a glass slide. Two masks were used to fabricate the multiple heights for main channel ($40 \mu\text{m}$ height) and the migration channel ($5 \mu\text{m}$ height). One device contains 900 migration channels (450 channels in one side), and the migration channel is $30 \mu\text{m}$ in width, $5 \mu\text{m}$ height, and 1mm in length. The PDMS layer was bonded to the glass slide after activated by oxygen plasma treatment (80 Watts, 60 seconds) to form a complete

fluidic channel. The microfluidic chips were sanitized by UV radiation prior to use to ensure aseptic conditions. Before cell loading, a collagen (Collagen Type 1, 354236, BD Biosciences) solution (1.45 mL Collagen, 0.1 mL acetic acid in 50 mL DI water) was flowed through the device for ten hours to coat collagen on the substrate to enhance cell adhesion. Devices were then rinsed with PBS (Gibco 10082) for five minutes to remove the residual collagen solution. Culture media was used to rinse devices before cell loading.

For device loading, cells were harvested from culture plates with 0.05% Trypsin/EDTA (Gibco 25200) and centrifuged at 1000 rpm for 5 minutes. Then, the cells were re-suspended in culture media to a concentration of 3×10^5 cells/ mL. One hundred microliters (100 μ L) of this cell suspension was pipetted into the lower inlets. After 3 minutes, cell solution in the left and right inlets was replaced with 50 μ L of serum culture media, and 40 μ L serum culture media was applied to the central inlet for both high and low sides. After 30 minutes, media in all inlets were emptied out and replaced by 200 μ L serum-free culture media (for the high-left and high-right inlets), and 200 μ L serum culture media (for the high-central inlet) to induce chemotactic migration. Then, the entire chip was put into a cell culture incubator for 5 hours to prepare for image acquisition.

6.4 Mitochondrial classification and image processing

As the “powerhouse” of eukaryotic cells [18], mitochondria are important in energy demanding behaviors. This includes cell migration, which requires cellular polarization, reorganization of actin filaments, and recruitment of structural and signaling components [19]. Studies have shown that perturbations to mitochondria dynamics (i.e. fragmentation and fusion) may affect cell development, cell cycle or cell signaling [20]. However, those studies were mostly

carried out by means of subjective observation or qualitative explanation, instead of objective, quantitative analysis. To investigate mitochondria in migration more in-depth, we segmented each mitochondrion after a series of image pre-processing steps, including background noise removal, contrast enhancement, deblurring, and histogram-based auto-thresholding (Fig. 6-3 (a-f)). We trained an RDF classifier to automatically categorize each mitochondrion into three types: dots, which represent fragmented mitochondria; fiber, which includes interconnected networks and elongated mitochondrial fibers; or intermediate, which defines mitochondria whose length is in between dots and fibers. By using 1000 manually labelled mitochondria as training sets and 200 as test sets, we achieved 97.5% overall accuracy in mitochondrial classification (Fig. 6-3 (g, h)). As an average of the result, 61.1% of the total area of mitochondria are classified as fiber, 20.5% as intermediate, while 18.4% as dots. This mitochondrial class distribution is skewed to 71.1% for fiber, 13.2% for intermediate, and 15.7% for dot, when exposed to a chemotherapeutic drug, and to 49.1% for fiber, 28.3% for intermediate, and 22.6% for dot when cells are classified as highly migratory from our microfluidic device.

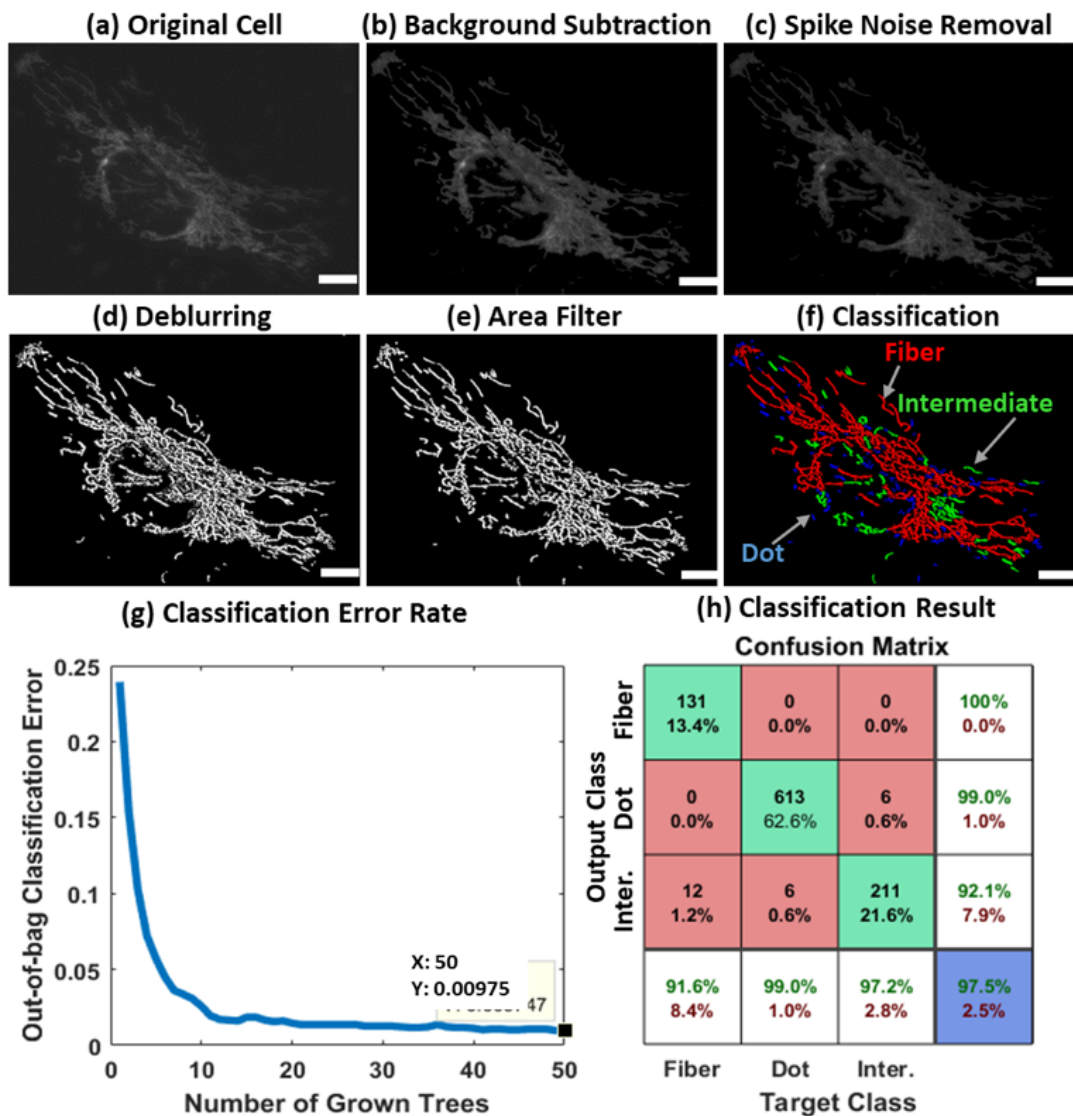


Figure 6-3. Image processing flow for the original microscope image (a-f) and mitochondrial classification (g, h). (a) The original image of a SUM159 cell was taken with a 40x objective lens. (b) Background of the original image was removed to have a clear view of the cell. (c) Spike noise was removed from the image. (d) A 5-pixel by 5-pixel Wiener filter was applied for deblurring purposes. (e) A 15-pixel large area filter was applied for sharpening and thresholding. (f) All mitochondria of a cell were classified into three classes: fiber, intermediate and dot based on a Random Decision Forest (RDF) classifier. (scale bar: 10 μ m). (g-h) Results of mitochondrial classification. (g) Out-of-bag classification error decreased with the increased number of grown trees using the RDF model. (h) Classification results shown by confusion matrix stated that the correction rate was above 97%, with no misclassification between fiber and dot class.

6.5 Feature extraction and data pre-processing

With the information of processed images from FITC/TRITC channel, we extracted 61 features for all 1358 single cells in our database. Definitions for these features were included in the Supplementary Information and feature extraction was done with the help of MATLAB R2017a. For direction prediction, these 61 features were taken with their original value. For speed prediction, features with name starting like “TopDownXXX”, CenterShift, FiberUpDownRatio, MaxWidth, MaxWidthSum, TotalAreaRatio, TotalPerimeterRatio, TotalPerimeterHalfRatio, HeadAverageWidth, HeadAverageWidthRatio, RedShift, RedFoot, RedGreenDist, and TotalAreaHalfRatio were reconsidered to make cell moving direction no longer important (e.g. CenterShift values -1 (for up-moving cells) and 1 (for down-moving cells) were different for direction prediction but the same for speed prediction. Therefore, both values should be taken as 1 in speed prediction.

After data normalization, whitening transformation was applied for feature decorrelation, which makes the covariance matrix of feature space to an identity matrix. By deploying Zero-phase Component (ZCA) whitening method with a ZCA constant of 0.0001, the correlation coefficient between most of the features are reduced to below 0.1 (Fig. 6-4). Wrapper method feature reduction was implemented to minimize the influence of unrelated or redundant features. These 61 features were first normalized (zero mean and unit variance), and then took turns to be all zeros for one feature. For each arrangement, an average error rate was calculated from 50 predictions using our Artificial Neural Network (ANN). In all 61 error rates, the feature with the lowest error rate was deleted. Features were deleted one by one until a new deletion would visibly increase the prediction error rate.

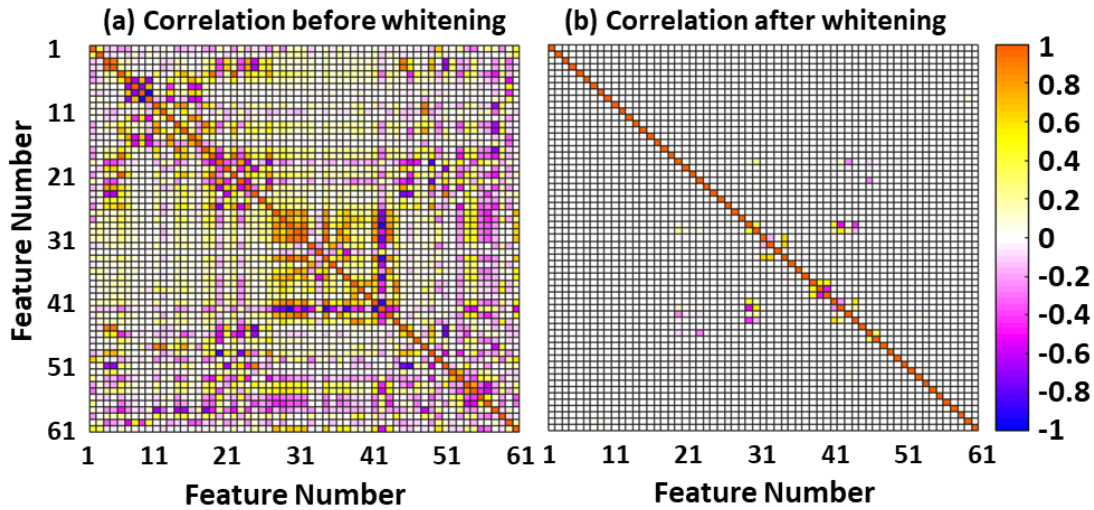


Figure 6-4. Morphological feature correlation heatmap (a) before whitening transformation, (b) after whitening transformation

6.6 Cell migration direction prediction

The study of migration direction, which involves the process of cellular reaction to mechanical/ chemical cue, cytoskeleton polarization, and signaling dynamics, provides important clues to our understanding of underlying mechanisms of metastasis [21,22]. Therefore, we developed a machine learning model to predict and explain cell migration merely based on the morphological features of cancer cells. Random Decision Forest (RDF) is a commonly used classifier, as well as a regression tool, which constructs a binary decision tree by asking a sequence of simple questions to inputs and assign a label to each condition [23]. To overcome an overfitting issue that is caused by using an over-complicated tree structure, a bootstrap-aggregated decision tree technique is often adopted for better model performance because it decreases the number of variables of the model and combines the results of multiple decision trees [24].

We first implemented RDF for cell migration direction classification. Bootstrapped-aggregated decision trees were constructed based on subsets of the training data set and this could

reduce the variance significantly. We took the mode of all outputs from trees for classification and took the average for regression. In MATLAB, we used the function “TreeBagger” to simulate the growth of random decision forest. For cell direction prediction and cell speed prediction, 500 trees were grown to let the error rate become stable. Artificial neural network was also chosen for cell direction and speed predictions because of its nonlinear characteristic. Every single feature in our raw data were set to zero average and unit variance before being inputted into our model. We chose a two-hidden-layer pattern net as our model and by going through all possible combinations of hidden node numbers for two hidden layers, the best result was achieved when the first hidden layer had 21 nodes and the second had 7 nodes. In our model, 70% of our data were used for training, 20% for validation and 10% for test. With the aim of distinguishing highly-motile cells against non-motile cells, we randomly pick out 134 cells (10% of the total dataset) from top 10% fast-moving cells and top 10% slow-moving cells as test set, while the rest of the cells were split to training set and validation set. Hyperbolic tangent sigmoid transfer function (“tansig” in MATLAB) was used as the activation function for two hidden layers and linear transfer function (“purelin” in MATLAB) was used as the activation function for the output layer. Scaled conjugate gradient backpropagation (“trainscg” in MATLAB) was used as our training function with the intention to reduce the mean square error.

Due to confinement of the migration channels, all the cancer cells were only allowed to move bidirectionally and were labeled according to the movement of the center of mass measurement by computer program. With the randomly scrambled cell image inputs, we achieved more than 99% accuracy in prediction of cell migration direction (Fig. 6-5 (a)). We also performed a feature importance analysis by summing the estimates of all weak learners in the bagged decision trees. Based on the importance analysis, we validated that features reflecting cellular polarization

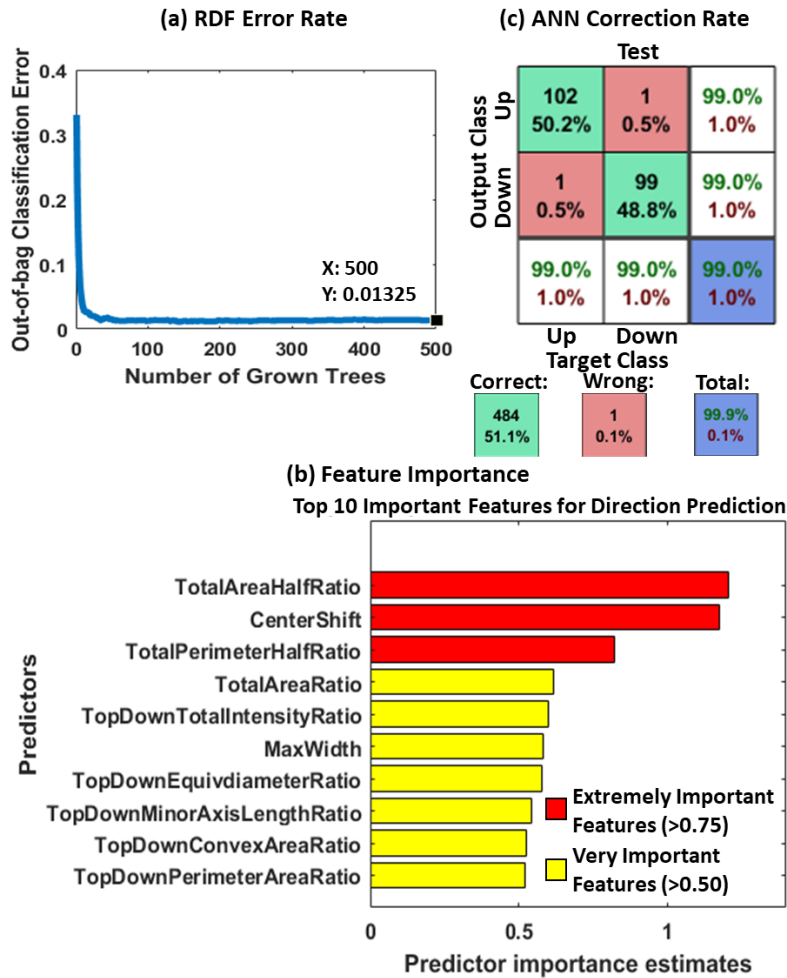


Figure 6-5. Results and important features for cell migration direction prediction. (a) Out-of-bag error rate for cell migration direction prediction using RDF. With the increase in number of grown trees, the error rate reduces to less than 1%. (b) Confusion matrices for testing datasets. Accuracy for cell migration direction prediction is above 99%. (c) Top 10 important features for cell migration direction prediction.

are essential in deciding the migration direction (Fig. 6-5 (b), and Fig. 6-6). These features include: TotalAreaRatio, which defines the ratio of the areas between the upper and lower half of the cell, CenterShift, which defines of the deviation of the center of mass from the graphic center, as well as TotalPerimeterRatio, which defines the ratio of the perimeters between upper and lower half of the cell. Although most of the critical morphological features are about cell polarization, each

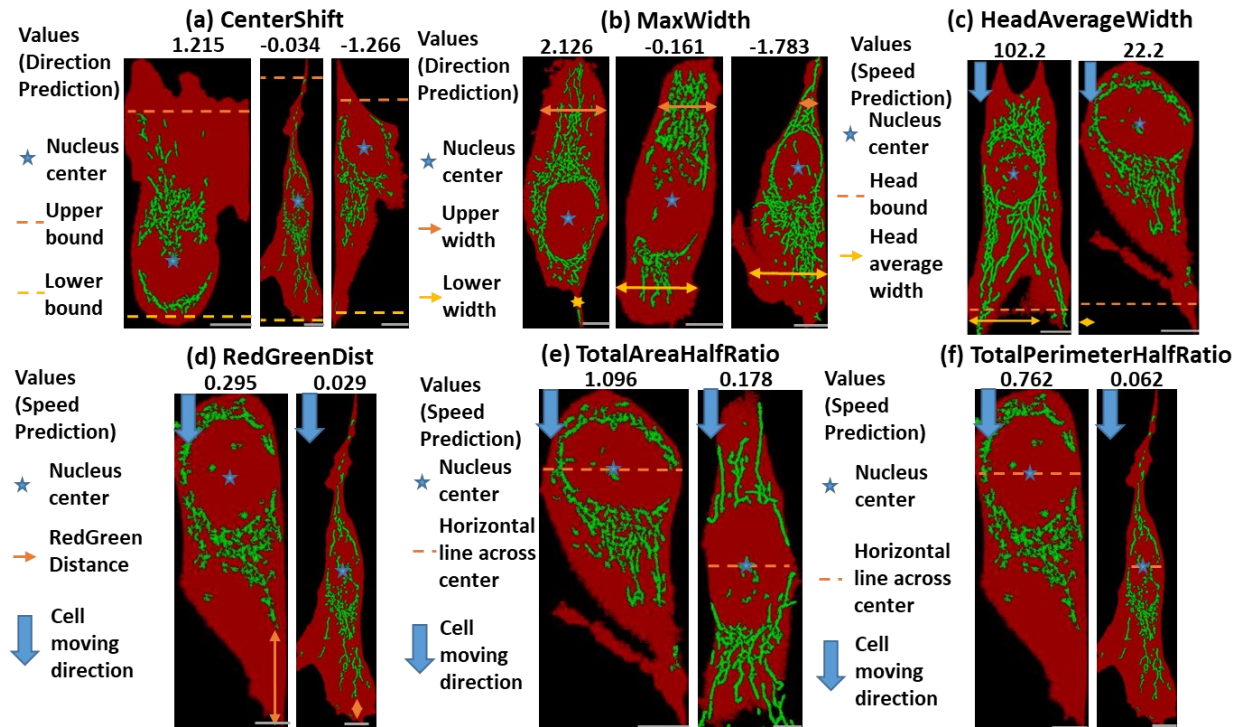


Figure 6-6. Selected important features for cell migration direction/speed prediction. (a) For direction prediction, up-moving cells tend to have positive CenterShift values and down-moving ones tend to have negative CenterShift values. For speed prediction, large CenterShift values typically indicated fast-moving cells. (b) For direction prediction, up-moving cells often had positive MaxWidth values and down-moving ones often had negative MaxWidth values. For speed prediction, large MaxWidth values typically indicated fast-moving cells. (c) For speed prediction, large HeadAverageWidth values typically indicated fast-moving cells. (d) For speed prediction, large RedGreenDist values typically indicated fast-moving cells. (e) For direction prediction, up-moving cells often had positive TotalAreaHalfRatio values and down-moving ones often had negative TotalAreaHalfRatio values. For speed prediction, large TotalAreaHalfRatio values typically indicated fast-moving cells. (f) For direction prediction, up-moving cells often had positive TotalPerimeterHalfRatio values and down-moving ones often had negative TotalPerimeterHalfRatio values. For speed prediction, large TotalPerimeterHalfRatio values typically indicated fast-moving cells. (scale bar: 10 μ m).

feature conveys its own unique information. For example, CenterShift indicates that the nucleus is more likely to appear in the rear portion of the cell, with a protrusion stretched to the front;

TotalPerimeterRatio represents not only the effect from nucleus center shift, but also the border length of the cell frontier (i.e. cells with filopodia-like protrusions tend to have larger perimeters).

Although RDF is straightforward to handle and advantageous in interpreting feature importance, it sometimes will only give suboptimal solutions due to the nature of greedy growing algorithm, as well as unstable to even slight perturbations of the training data. Artificial Neural Network (ANN) is a nonlinear model for universal function approximation. With enough data sets, ANN is more likely to provide better prediction power. Therefore, we further explored ANN for predicting cell migration direction. Based on a database of 1,358 single-cell images collected using the presented method, we trained a four-layer-ANN model which achieves an overall accuracy of 99.6% combining training, validation, and test data (Fig. 6-5 (c)).

6.7 Cell motility (migration speed) prediction

In addition to direction, we further explored the capability of our machine learning model in predicting motility or migration speed. This will provide insights for the discovery of critical markers determining cancer metastasis. To quantify cell migration speed, images for cells at the same location were taken with a roughly 10-minute period. Movement for a single cell was defined as the movement of center of mass of images under FITC channel. In order to allow the cell speed to be more accurate, imaging time was recorded for each image. With this information, cell speed could be calculated by dividing movement of a single cell by difference of imaging time.

Using the same workflow as described previously, we first applied RDF to pinpoint the important features affecting cell migration speed (Fig. 6-7 (a, b)), and further enhanced the prediction power using ANN. Previous studies suggest that cell migration is correlated with

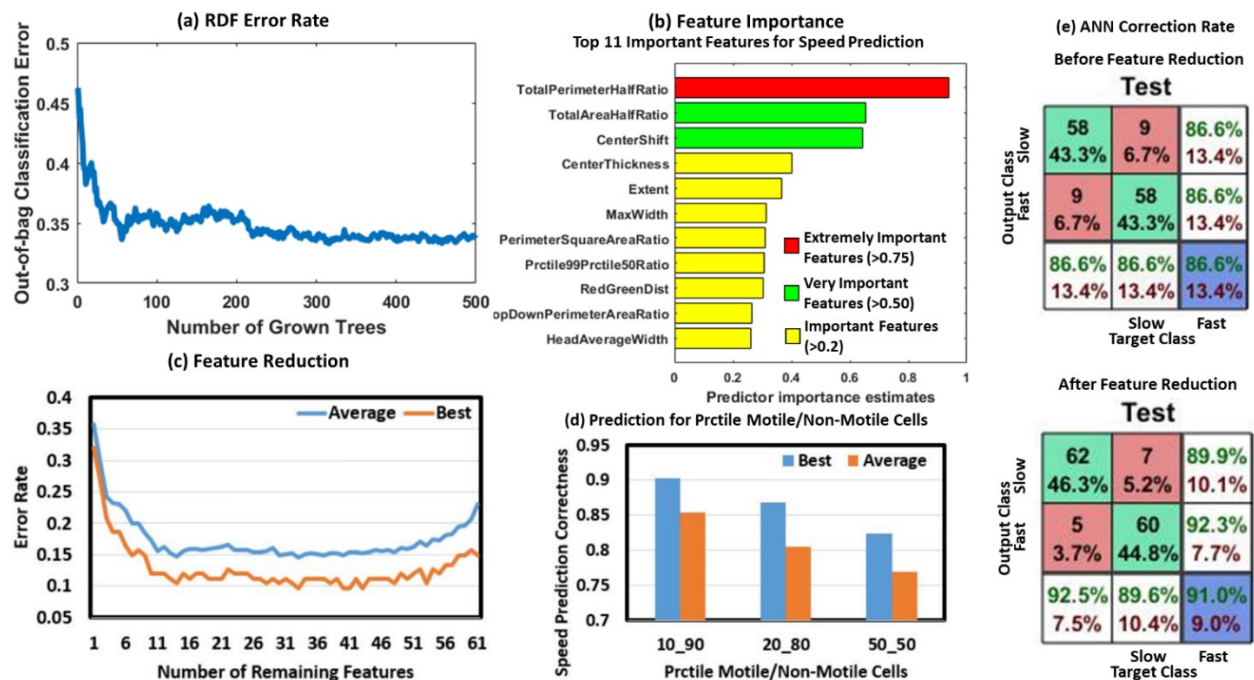


Figure 6-7. Cell migration speed prediction. (a) Out-of-bag error rate for cell migration speed prediction using RDF. With the increase in number of grown trees, the error rate reduces to 33%. (b) Top 10 important features for cell migration speed prediction. (c) The error rate (average of 50 individual runs) can be further reduced to about 18% by eliminating 15 less relevant features and then the error rate remains stable until having 24 residual features. After that, the error rate goes up rapidly with the reduction of features. The features reduced at the last stage are critical features. (d) Correction rate for cell migration speed prediction before feature reduction was 86.6%. (e) Speed regression from our neural network model is correlated with cell actual speed. (pixels/s)

mitochondria distribution within a cell [6]. With the help of our machine learning model, we discovered that many other morphological features can also predict cell migration. Similar to cell migration direction, we found that cellular polarization-related features are still critical in determining speed. Unexpectedly, our model also found that other features also provide interesting insights into cell migration. For example, RedGreenDist, which is defined as the distance from the front of a cell to the first mitochondrion, normalized with the total length of the cell, is positively correlated with migration speed. This reveals that the mitochondria network does not necessarily

have to be located at the leading edge of a cell to affect cell migration. Furthermore, CenterThickness, which is measured by taking the ratio of the average intensity over a small area of the nucleus region to the median intensity of the whole cell, suggests that the larger the difference is between the center area and cell edge, the more likely a cell moves faster. Evidence suggests that a fiber-like or fused mitochondrial network structure is favorable for supplying energy for cell migration, whereas dotted mitochondria, or mitochondrial fission, has been reported as an indicator of extracellular stress or cell apoptosis. However, in our study, we did not find strong correlation between mitochondria morphology with migration behaviors.

In the next step, we also implemented a neural network for migration speed prediction including classification of fast/slow moving cells and regression of moving speed. Targeting on selecting the high-migratory cells, which has been reported with significantly greater tumor formation and metastasis capabilities in mouse models, we set top 10% migration speed as a labelling threshold for fast-moving cells. Similarly, bottom 10% migration speed was used to label slow-moving cells, so that balanced inputs for both classes was obtained. Based on the extracted 61 morphology features, our 4-layer neural network classifier achieves 86.6% prediction accuracy at the best case (77.1% as average). To improve computational efficiency as well as avoid overfitting, we performed the wrapper method feature selection using the neural network as a performance evaluation model. We took an average of 50 individual runs on each of the leave-one-out subset of features and picked the subsets that achieve the best accuracy on test data. As shown in Fig. 6-7 (c), the NN classifier obtained an increase in accuracy when the number of features was reduced from 61 to around 33 with the best case reaching 91.0% accuracy (85.3% as average) (Fig. 6-7 (d)). The further reduction of features will lead to a dramatic increase in error rate due to the loss of significant information. This also suggests that the longer one feature remains

in the feature reduction process, the more it contributes to speed prediction. The remaining last 5 features were TotalAreaHalfRatio, TotalAreaRatio, CenterShift, TotalPerimeterHalfRatio, and MaxWidth, which matches well with the feature importance analysis in the random forest model. In addition, we also applied a neural network for regression to predict cell movement in a quantitative manner. This optimized model yields 0.0004 pixels/s (0.00006 $\mu\text{m/s}$) in normalized mean square error of migration speed (Fig. 6-7 (e)).

6.8 Validation of morphological features by altering cell migration behaviors

Following our workflow, several morphological features were identified as critical markers of cellular migration. Due to the statistical nature of machine learning models, and its strong dependence on data inputs, our computational results could lead to a trivial or irreproducible discovery. Therefore, to validate the robustness and biological relevance of our model, we further designed control experiments with altered cell migration behavior and examined whether the critical morphological markers we found changed as the migration speed changed (Fig. 6-8). As a negative control, we inhibited the migration of SUM159 cells with doxorubicin, which has been widely used as treatment of metastatic breast cancer [25]. Doxorubicin treatment reduced the average migration speed by 25.3% as compared to cells treated with vehicle (control). As expected, we also observed a decrease in the average of some morphological markers, such as CenterShift, MaxWidth, and TotalAreaHalfRatio, which demonstrates a positive correlation with migration speed in our RDF prediction model. We also performed a positive control experiment by harvesting fast-moving cells (top 1% of the bulk SUM159 population), re-loading these selected cells to another of our migration devices, and observing their migratory behavior. We observed

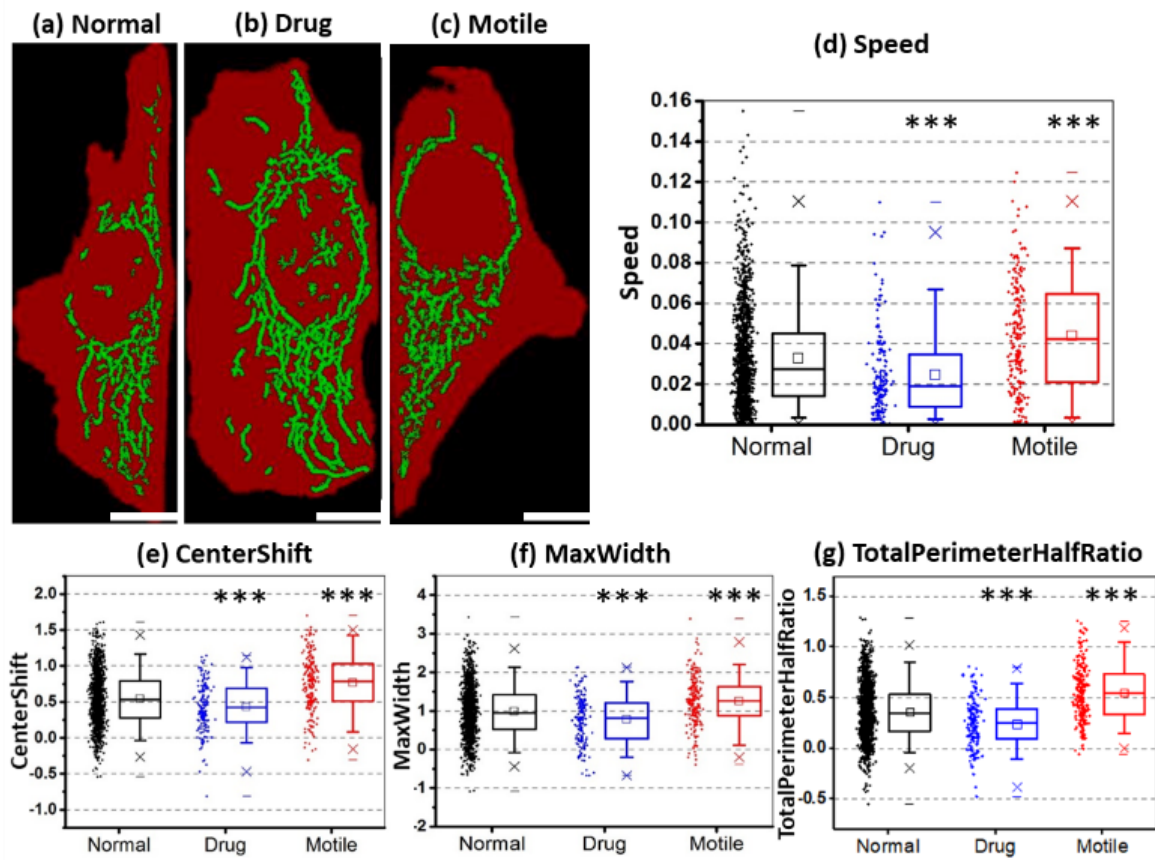


Figure 6-8. Typical images for normal/drug-pretreated/motile cells and medium value differences of selected important features for cell migration direction/speed prediction. (a-c) Typical images for normal/drug-pretreated/motile cells. (a) Normal cells was not too fat and CenterShift was not so obvious. (b) Drug-pretreated cells were fat, flat and their mitochondria were more filamentous. (c) CenterShift values for motile cells were often quite large and their mitochondria were more fragmented. (scale bar: 10 μm). (d) Median speed for motile cells is faster than normal ones while median speed for drug-pretreated cells is slower than normal ones. (e-g) Medium value differences of selected important features for cell migration direction/speed prediction. The unit is pixel per second. (e) Medium CenterShift value for drug cells was below the one for normal cells while medium CenterShift value for motile cells was above the one for normal cells. (f) Medium MaxWidth value for drug cells was below the one for normal cells while medium MaxWidth value for motile cells was above the one for normal cells. (g) Medium TotalPerimeterHalfRatio value for drug cells was below the one for normal cells while medium TotalAreaHalfRatio value for motile cells was above the one for normal cells. “***” means significance level is smaller than 0.001.

that highly motile cells maintained their highly migratory properties, and moved on average 34.0% faster than wild-type SUM159 cells. As a result, we also observed significantly higher values in those positively correlated morphological markers. A combination of the two experiments with “slow runners” and “fast runners” confirmed that the important features we pinpointed can be reliably used as morphological markers for cancer cell migration.

6.9 Chapter summary

Due to limitations of conventional marker-based approaches to identify motile cells, we aimed to establish a direct link between morphological features and cell migration. We focused on mitochondrial morphology because studies have shown that mitochondria influence cell migration. Although mitochondrial fragmentation has been reported to be associated with migratory behavior in different breast cancer cell lines²⁶, we found it has a weak correlation with the fast-moving and slow-moving SUM159 triple negative breast cancer cells. Furthermore, another study suggests a link between mitochondria distribution and cell migration, yet the prediction power (53.4% accuracy) is too low to be reliable¹³. To improve upon this, our method extracted 61 morphological features of both mitochondria and the whole cell and correlated these features with migration at an accuracy of 72.0% max, 51.6% min, 54.7% mean, and 53.9% median. Although the accuracy is improved, this result suggests that the mechanisms underlying cell migration are complex and highlights limitations of conventional hypothesis-driven studies using only one parameter.

To address limitations of using single features, we applied cutting-edge Random Decision Forest (RDF) and Artificial Neural Network (ANN) models for prediction. To generate a large

database for training models, we used our single-cell microfluidic migration chip¹⁷ to track hundreds of cells on a chip. Using a database of 1,358 SUM159 cancer cells, we determined that the comprehensive computer vision method is significantly better than the conventional single feature-based prediction. To optimize the RDF model, we swept the number of trees and found that 500 trees are enough for prediction. Optimization of ANN was more complicated, as we had to remove redundant and irrelevant features as well as determine the numbers of layers and hidden nodes. We found that removing around 28 features and building a geometry using a 4-layer neural network (2 layers with hidden nodes, 21 hidden nodes in the first layer and 7 hidden nodes in the second layer) achieves the highest prediction power. Using the ANN model, we achieved over 99% correct prediction for movement direction and 91% for speed, while the RDF model is slightly less accurate (67% for speed).

In addition to prediction, we used the RDF model and reduced the features in the ANN model to pinpoint top-ranked key features important for cell migration. Some of these key features are known to relate to cell polarization (such as CenterShift), but we also identified novel features (such as RedGreenDist and CenterThickness) that correlated with cell migration. The identification of novel features highlights the limitations of current methods, and potentially advances our understanding about mechanisms involved in cell migration. To validate that the identified features are indeed critical for cell migration, we performed migration experiments using pharmaceutically pre-treated cells (expected to have lower speed), and highly migratory cells from our microfluidic device (expected to have higher speed) [27]. When comparing these experimental cell populations with wild-type cancer cells, we found the same associations between morphological features (CenterShift, MaxWidth, and TotalAreaHalfRatio) and cell speed, further supporting the importance of our discovered features in cell movement.

In this study, we established a method to predict cell movement by morphological features using computer vision and machine learning, achieving unprecedented prediction power for cell movement. This unbiased method discovers both known and novel features critical for the cell migration process. The features identified here can aid in our understanding of cancer cell migration, and lead to new approaches for identifying metastatic cancer cells. Although the current study focuses on one breast cancer cell line on a 2D substrate, the strong prediction power of the morphological markers suggests broader applications for this method. In the future, this method can be used to explore other cancer types, cell movement in a 3D environment, and other cell behaviors, such as metabolism and cell-cell interaction.

Chapter 7 : Conclusions

7.1 Summary

In the past decades, large amount of efforts and investment has been given to the development of cancer chemo-drugs. Although therapeutic efficacy has improved, both clinical research and industrial development continue to suffer from extremely low success rates in translating preclinical discoveries into clinical approval. A large percentage of promising compound candidates from preclinical trials eventually fail the validation in human testing. In order to achieve desirable patient outcomes and reduce development cost, it is imminent to improve the preclinical drug screening model with both good physiological relevance and good scalability. One of the key components that contributes to cancer drug response is tumor micro-environment (TME). Recently, TME has drawn more and more attention in cancer drug development as the accumulating evidence shows that drug efficacy significantly variation in different TME. Recently, considerable efforts have been put forward to develop high-throughput TME-mimicking platform. Microfluidic techniques stand out among many candidates due to low cost, precise fluidic control and cell manipulation, and compatibility of biomimetic structures, .

In addition, High-throughput microfluidic drug screening platforms could provide the large amount of high-dimensional data. In order to automate the extraction of image features and analysis of biological information from large dataset, an increasing number of research works have attempted to incorporate microfluidic devices with machine learning tools for system automation and rapid data analysis. Recent advances in machine learning (especially deep learning,

which relies on the structure of neural network) have enabled analysis of biomedical images in a high-throughput manner. However, very few works explored the deep learning algorithms for drug screening. We integrate machine learning techniques and microfluidic chip to facilitate the high-throughput drug response analysis and cellular behavior interpretation and prediction.

Here, we first presented three microfluidic platforms using three different TME-mimicking drug screening models: spheres in matrix, aggregated spheres in suspension, and clonal spheres in suspension. The first work reports a novel gel-island microfluidic platform enabling drug screening in 3D extracellular matrix (ECM). Since cellular heterogeneity contributes to drug resistance, we investigate the heterogeneous drug response in ECM at single cell resolution. The platform has several advantages: (1) reliable single cell loading in 3D gel-islands, (2) high-throughput (1500-well) drug screening, and (3) automatic single cell lineage tracking. The presented platform enabled automatic tracking of single cell behaviors and analyzing drug response of thousands of individual cells in biomimetic 3D microenvironment. Combining 3D ECM culture and single cell resolution screening, we identified the cancer subpopulation that showed resistance to the conventional cancer drug, which should be targeted for new drug development.

The second platform realized the cell aggregated sphere model to mimic 3D tumor structures for combinatorial drug screening. Drug combinations have been widely accepted in cancer treatment for better therapeutic efficacy as compared to single compound. Although several systems have been presented for drug combination screening, they were limited to low throughput of only two drugs, requiring complicated operation systems, or time-consuming serial processes. We developed a scalable, easy-to-handle, high-throughput drug combination screening platform, which enables screening of any possible dual-drug combinations from N different drugs with five different mixing ratios in each combination. As a proof of concept, we implemented an 8-drug

combination platform. Combining 28 drug combinations, 7 mixing ratios, and 6 replicates, total 1,032 drug-efficacy screening experiments could be accomplished in a single chip. Using breast cancer cell lines, pancreatic cancer cell lines, and patient-derived cell lines, we demonstrated effective drug combination screening for precision medicine.

Recent studies suggested that among bulk tumors only a small subpopulation of cancer cells, known as cancer stem-like cells (CSCs), possess capabilities of self-renewal, differentiation, tumor-initiation, and cancer drug resistance, which may lead to cancer relapse after drug treatment. In order to identify CSCs in a tumor clone, we developed a Hi-Sphere chip to realize the single-cell derived 3D clonal sphere model. Combined with fluorescence labelling techniques, Hi-Sphere chip enables the study of cancer heterogeneity in two aspects: inter-clonal heterogeneity and intra-clonal heterogeneity. The Hi-Sphere chip is capable of culturing more than 2,400 single-cell-derived clonal spheres and selectively retrieve them based on sphere size, which separates different subtypes from the clonal spheres, e.g. holoclones, meroclones, and paraclones. We discovered the majority of CSCs were located at the leading edge of holoclones.

To enable automatic readout of cancer drug efficacy in a low-cost, time-efficient, and reliable manner, we applied the computer vision and machine learning algorithms to the microscope images of cells acquired from the presented drug screening chip. We used the 6-drug-condition microfluidic chip that allowed thousands of tumor spheres formed, cultured, and drug treated on-chip. The cellular bright-field microscope images were collected, and the micro-chambers containing spheres were tracked for analysis automatically. We trained a convolutional neural network for sphere viability estimation based on live/dead staining results. The machine learning model could distinguish tumor sphere viability with only bright-field microscopy images. In this manner, we could accurately estimate the half-maximal inhibitory concentration (IC50).

More interestingly, we found there were common features indicating viability across different chemo-drugs, suggesting the potential that a generic model could be established for various drugs. The presented method provided an automatic, high-throughput and non-invasive method to assess tumor sphere viability for large-scale drug screening.

In addition, an approach of analyzing single-cell migration in a microfluidic platform was explored in conjunction with artificial neural network (ANN). Cancer cells with enhanced motility and invasiveness tend to migrate away from primary tumor site and initiate metastatic process. Therefore, identifying key aspects for cell migration is crucial for understanding and ultimately overcoming metastasis. Considerable efforts have focused on discovering markers for epithelial-to-mesenchymal transition (EMT), a developmental program in which epithelial cells acquire migratory and invasive phenotypes to promote metastasis. Yet marker-based approaches are limited by inconsistencies among patients, types of cancer, and partial EMT states. In this work, we presented a comprehensive morphological analysis using deep learning methods, including Random Decision Forest (RDF) and ANN to establish the correlation between cellular morphology and migration direction/speed. We developed a workflow to discover and validate morphological features that associate with migration. Thanks to the high throughput of microfluidics, we easily accumulated the images from 1,358 cells migrating in microfluidic channels. The images were processed by noise removal, deblurring, sharpening, and thresholding, and then extracted 61 morphological features. Using both cellular and mitochondrial features as inputs, we trained the RDF and ANN models to predict cell migration direction, and achieved 99% accuracy with both models, and identified key predictive features. We further developed one method to recognize fast-moving cancer cells associated with metastasis. We started with the RDF model but had a low accuracy of 67%. Thus, we focused on more advance ANN model. We iteratively removed

redundant and irrelevant features as well as optimized the numbers of layers and hidden nodes. We found the optimized neural network geometry and achieved a highest accuracy of 91%. In addition, we also applied regression to accurately estimate cell speed with an extremely small mean square error of 0.0004 pixels/s (0.00006 $\mu\text{m/s}$) mean square error. The accurate results demonstrated the feasibility of correlating cell behaviors with morphology using deep learning models.

7.2 Future works

7.2.1 Pharmacokinetic study:

We explored the application of drug pairs in cancer therapy with high-throughput drug combination screening microfluidic chip. However, there is another key component in the course of drug combination treatment, which is drug administration scheduling. Recent studies have shown that the temporal order and during of combinatorial cancer treatment had influence on the outcome [1-3]. This phenomenon involves the interaction between drug compounds [4, 5] and the study of pharmacokinetics [6], which is affected by drug absorption, distribution, and metabolism [7]. It is also critical to include the optimization of drug combination temporal scheduling in drug combination screening experiment to achieve the best therapeutic efficacy. The advantage of microfluidics in accurate fluidic control makes it a promising screening tool for temporal scheduling optimization. Combined with automatic syringe pump, various types of flow pattern in different duty cycles could be generated in microfluidic drug screening platforms to simulate different drug treatment regimen.

7.2.2 Interpretable deep learning model to understand cancer cell behavior

As a universal function approximator, deep learning models have the ability to model complexed and abstract relationship between random variables using the data-driven approach [8]. Although deep learning emerges as a powerful tool in automatic image analysis and cellular behavior prediction, it has been treated as a black box in most cases. The poor interpretability limits its wider fields of application in biological study. In recent years, a large number of works [9-11] attempted to narrow the gap between deep learning models and human reasoning. Among the important advancement, attention mechanism stands out by improving model transparency and visualization of model functionality [12, 13]. When human looks at an image input for classification task, the eye first grabs a rough image of the scene, from which the vision system extracts regions of interest [14]. Then we focus on specific areas of the image and recognition tasks are performed using a combination of features extracted from all such regions. Inspired by this mechanism, attention model improves the visualization and interpreting the latent layers of CNNs by generating a attention map: a matrix with the same size of the input tensor representing the relative importance of layer activations at different 2D spatial locations with respect to the ground truth target [15]. For example, in an image classification task between cats and dogs, the regions of ears, whiskers, or tails may play a more important role in distinguishing the two animals [16], compared to other regions in the input images, such as background and torsos. By calculating a compatibility score between local feature maps and global features used for image classification, an attention map representing the importance weight of different regions towards final classification task was generated. This provides human observers a visible clue in reasoning the inner CNN working mechanism.

References

Chapter 1:

- [1] DeVita, Vincent T., and Edward Chu. "A history of cancer chemotherapy." *Cancer research* 68.21 (2008): 8643-8653.
- [2] Rubin, Eric H., and D. Gary Gilliland. "Drug development and clinical trials—the path to an approved cancer drug." *Nature reviews Clinical oncology* 9.4 (2012): 215.
- [3] Basch, Ethan, et al. "Patient-reported outcomes in cancer drug development and US regulatory review: perspectives from industry, the Food and Drug Administration, and the patient." *JAMA oncology* 1.3 (2015): 375-379.
- [4] Kelloff, Gary J., et al. "Biomarkers, surrogate end points, and the acceleration of drug development for cancer prevention and treatment: an update prologue." *Clinical cancer research* 10.11 (2004): 3881-3884.
- [5] Kinch, Michael S. "An analysis of FDA-approved drugs for oncology." *Drug discovery today* 19.12 (2014): 1831-1835.
- [6] Blagosklonny, Mikhail V. "Analysis of FDA approved anticancer drugs reveals the future of cancer therapy." *Cell Cycle* 3.8 (2004): 1033-1040.
- [7] Siegel, Rebecca L., et al. "Colorectal cancer statistics, 2020." *CA: a cancer journal for clinicians* (2020).
- [8] Morgan, Steve, et al. "The cost of drug development: a systematic review." *Health policy* 100.1 (2011): 4-17.
- [9] Stewart, David J., et al. "The importance of greater speed in drug development for advanced malignancies." *Cancer medicine* 7.5 (2018): 1824-1836.
- [10] Teicher, Beverly A., ed. *Anticancer drug development guide: preclinical screening, clinical trials, and approval*. Springer Science & Business Media, 2013.
- [11] Takebe, Tohru, Ryoka Imai, and Shunsuke Ono. "The current status of drug discovery and development as originated in United States academia: the influence of industrial and academic collaboration on drug discovery and development." *Clinical and translational science* 11.6 (2018): 597-606.
- [12] Morgan, Steve, et al. "The cost of drug development: a systematic review." *Health policy* 100.1 (2011): 4-17.
- [13] Lowenstein, Pedro R., and Maria G. Castro. "Uncertainty in the translation of preclinical experiments to clinical trials. Why do most phase III clinical trials fail?." *Current gene therapy* 9.5 (2009): 368-374.
- [14] Seyhan, Attila A. "Lost in translation: the valley of death across preclinical and clinical divide—identification of problems and overcoming obstacles." *Translational Medicine Communications* 4.1 (2019): 1-19.
- [15] Imamura, Yoshinori, et al. "Comparison of 2D-and 3D-culture models as drug-testing platforms in breast cancer." *Oncology reports* 33.4 (2015): 1837-1843.
- [16] Friedman, Adam A., et al. "Precision medicine for cancer with next-generation functional diagnostics." *Nature Reviews Cancer* 15.12 (2015): 747.

- [17] Dugger, Sarah A., Adam Platt, and David B. Goldstein. "Drug development in the era of precision medicine." *Nature reviews Drug discovery* 17.3 (2018): 183.
- [18] Ross, Jeffrey S. "Targeted therapies for cancer." *Essentials of Genomic and Personalized Medicine*. Academic Press, 2010. 532-547.
- [19] Friedman, Adam A., et al. "Precision medicine for cancer with next-generation functional diagnostics." *Nature Reviews Cancer* 15.12 (2015): 747.
- [20] Garnett, Mathew J., and Ultan McDermott. "The evolving role of cancer cell line-based screens to define the impact of cancer genomes on drug response." *Current opinion in genetics & development* 24 (2014): 114-119.
- [21] Wagner, Bridget K. "The resurgence of phenotypic screening in drug discovery and development." (2016): 121-125.
- [22] Moffat, John G., Joachim Rudolph, and David Bailey. "Phenotypic screening in cancer drug discovery—past, present and future." *Nature reviews Drug discovery* 13.8 (2014): 588.
- [23] Hart, Charles P. "Finding the target after screening the phenotype." *Drug discovery today* 10.7 (2005): 513-519.
- [24] Moffat, John G., et al. "Opportunities and challenges in phenotypic drug discovery: an industry perspective." *Nature reviews Drug discovery* 16.8 (2017): 531.
- [25] Lee, Jonathan A., et al. "Modern phenotypic drug discovery is a viable, neoclassic pharma strategy." *Journal of medicinal chemistry* 55.10 (2012): 4527-4538.
- [26] Krutzik, Peter O., and Garry P. Nolan. "Fluorescent cell barcoding in flow cytometry allows high-throughput drug screening and signaling profiling." *Nature methods* 3.5 (2006): 361.
- [27] Astashkina, Anna, Brenda Mann, and David W. Grainger. "A critical evaluation of in vitro cell culture models for high-throughput drug screening and toxicity." *Pharmacology & therapeutics* 134.1 (2012): 82-106.
- [28] Zanella, Fabian, James B. Lorens, and Wolfgang Link. "High content screening: seeing is believing." *Trends in biotechnology* 28.5 (2010): 237-245.
- [29] Nam, Ki-Hwan, et al. "Biomimetic 3D tissue models for advanced high-throughput drug screening." *Journal of laboratory automation* 20.3 (2015): 201-215.
- [30] Bleicher, Konrad H., et al. "A guide to drug discovery: hit and lead generation: beyond high-throughput screening." *Nature reviews Drug discovery* 2.5 (2003): 369.
- [31] Zheng, Fuyin, et al. "Organ-on-a-Chip Systems: Microengineering to Biomimic Living Systems." *Small* 12.17 (2016): 2253-2282.
- [32] Zhang, Boyang, et al. "Advances in organ-on-a-chip engineering." *Nature Reviews Materials* 3.8 (2018): 257.
- [33] Mak, Isabella WY, Nathan Evaniew, and Michelle Ghert. "Lost in translation: animal models and clinical trials in cancer treatment." *American journal of translational research* 6.2 (2014): 114.
- [34] Bishop, Laura Jane, and Anita L. Nolen. "Animals in research and education: Ethical issues." *Kennedy Institute of Ethics Journal* 11.1 (2001): 91-112.
- [35] Zononi, Michele, et al. "3D tumor spheroid models for in vitro therapeutic screening: a systematic approach to enhance the biological relevance of data obtained." *Scientific reports* 6 (2016): 19103.
- [36] Imamura, Yoshinori, et al. "Comparison of 2D-and 3D-culture models as drug-testing platforms in breast cancer." *Oncology reports* 33.4 (2015): 1837-1843.
- [37] Friedl, Peter, and Katarina Wolf. "Tumour-cell invasion and migration: diversity and escape mechanisms." *Nature reviews cancer* 3.5 (2003): 362.

- [38] Lara Rodriguez, Laura, and Ian C. Schneider. "Directed cell migration in multi-cue environments." *Integrative Biology* 5.11 (2013): 1306-1323.
- [39] Cortese, Barbara, et al. "Influence of electrotaxis on cell behaviour." *Integrative Biology* 6.9 (2014): 817-830.
- [40] Ravi, Maddaly, et al. "3D cell culture systems: advantages and applications." *Journal of cellular physiology* 230.1 (2015): 16-26.
- [41] Balkwill, Frances R., Melania Capasso, and Thorsten Hagemann. "The tumor microenvironment at a glance." (2012): 5591-5596.
- [42] Whiteside, T. L. "The tumor microenvironment and its role in promoting tumor growth." *Oncogene* 27.45 (2008): 5904.
- [43] Cavo, Marta, et al. "Microenvironment complexity and matrix stiffness regulate breast cancer cell activity in a 3D in vitro model." *Scientific reports* 6 (2016): 35367.
- [44] Walker, Cameron, Elijah Mojares, and Armando del Río Hernández. "Role of extracellular matrix in development and cancer progression." *International journal of molecular sciences* 19.10 (2018): 3028.
- [45] Swartz, Melody A., et al. "Tumor microenvironment complexity: emerging roles in cancer therapy." (2012): 2473-2480
- [46] Wei, Spencer C., and Jing Yang. "Forcing through tumor metastasis: the interplay between tissue rigidity and epithelial–mesenchymal transition." *Trends in cell biology* 26.2 (2016): 111-120.
- [47] Janet, M. Tse, et al. "Mechanical compression drives cancer cells toward invasive phenotype." *Proceedings of the National Academy of Sciences* 109.3 (2012): 911-916.
- [48] Meads, Mark B., Lori A. Hazlehurst, and William S. Dalton. "The bone marrow microenvironment as a tumor sanctuary and contributor to drug resistance." *Clinical Cancer Research* 14.9 (2008): 2519-2526.
- [49] Correia, Ana Luísa, and Mina J. Bissell. "The tumor microenvironment is a dominant force in multidrug resistance." *Drug resistance updates* 15.1-2 (2012): 39-49.
- [50] Trédan, Olivier, et al. "Drug resistance and the solid tumor microenvironment." *Journal of the National Cancer Institute* 99.19 (2007): 1441-1454.
- [51] Östman, Arne. "The tumor microenvironment controls drug sensitivity." *Nature medicine* 18.9 (2012): 1332.
- [52] Abhyankar, Vinay V., et al. "A platform for assessing chemotactic migration within a spatiotemporally defined 3D microenvironment." *Lab on a Chip* 8.9 (2008): 1507-1515.
- [53] Pedron, Sara, Eftalda Becka, and Brendan A. Harley. "Spatially graded hydrogel platform as a 3D engineered tumor microenvironment." *Advanced Materials* 27.9 (2015): 1567-1572.
- [54] Herter-Sprue, Grit S., Andrew L. Kung, and Kwok-Kin Wong. "New cast for a new era: preclinical cancer drug development revisited." *The Journal of clinical investigation* 123.9 (2013): 3639-3645.
- [55] Sackmann, Eric K., Anna L. Fulton, and David J. Beebe. "The present and future role of microfluidics in biomedical research." *Nature* 507.7491 (2014): 181.
- [56] Riordon, Jason, et al. "Deep learning with microfluidics for biotechnology." *Trends in biotechnology* (2018).
- [57] Bellazzi, Riccardo, et al. "Data analysis and data mining: current issues in biomedical informatics." *Methods of information in medicine* 50.06 (2011): 536-544.
- [58] Guo, Baoshan, et al. "High-throughput, label-free, single-cell, microalgal lipid screening by machine-learning-equipped optofluidic time-stretch quantitative phase microscopy." *Cytometry Part A* 91.5 (2017): 494-502.
- [59] Singh, Dhananjay Kumar, et al. "Label-free, high-throughput holographic screening and enumeration of tumor cells in blood." *Lab on a Chip* 17.17 (2017): 2920-2932.

- [60] Li, Yueqin, et al. "Deep cytometry: Deep learning with Real-time inference in cell Sorting and flow cytometry." *Scientific reports* 9.1 (2019): 11088.
- [61] Chen, Claire Lifan, et al. "Deep learning in label-free cell classification." *Scientific reports* 6 (2016): 21471.
- [62] Ko, Jina, et al. "Combining machine learning and nanofluidic technology to diagnose pancreatic cancer using exosomes." *ACS nano* 11.11 (2017): 11182-11193.

Chapter 2:

- [1] M. J. Bissell, H. G. Hall, G. Parry, *J. Theor. Biol.*, 1982, **99(1)**, 31-68.
- [2] E. L. Baker, R. T. Bonnecaze, M. H. Zaman, *Biophys. J.*, 2009, **97(4)**, 1013-1021.
- [3] G. Y. Lee, P.A. Kenny, E. H. Lee, M. J. Bissell, *Nat. Methods*, 2007, **4(4)**, 259-265.
- [4] E. Jabbari, S. K. Sarvestani, L. Daneshian, S. Moeinzadeh, *PLoS One*, 2015, **10(7)**, e0132377.
- [5] J. S. Park, J. S. Chu, A. D. Tsou, R. Diop, Z. Tang, A. Wang, S. Li, *Biomaterials*, 2011, **32(16)**, 3921-3930.
- [6] Benien, Parul, and Archana Swami. "3D tumor models: history, advances and future perspectives." *Future Oncology* 10.7 (2014): 1311-1327.
- [7] W. J. Polacheck, R. Li, S. G. Uzel, R. D. Kamm, *Lab Chip*, 2013, **13(12)**, 2252-2267.
- [8] P. Lu, V. M. Weaver, Z. Werb, *J. Cell Biol.*, 2012, **196(4)**, 395-406.
- [9] N. J. Maitland, A. T. Collins, *JCO*, 2008, **26(17)**, 2862-2870.
- [10] J. Zhou, Y. Zhang, *Cell Cycle*, 2008, **7(10)**, 1360-1370.
- [11] D. L. Dexter, J. T. Leith, *JCO*, 1986, **4(2)**, 244-257.
- [12] J. P. Geisler, S. L. Rose, H. E. Geisler, G. A. Miller, M. C. Wiemann, *CME J. Gynecol Oncol.*, 2002, **7**, 25-28.
- [13] S. J. Morrison, J. Kimble, *Nature*, 2006, **441(7097)**, 1068-1074.
- [14] A. Cicalese, G. Bonizzi, C. E. Pasi, M. Faretta, S. Ronzoni, B. Giulini, C. Brisken, S. Minucci, F. P. Di, P. G. Pelicci, *Cell*, 2009, **138(6)**, 1083-1095.
- [15] C. Gonzalez, *Nat. Rev. Genet.*, 2007, **8(6)**, 462-472.
- [16] L. Chen, Z. Xiao, Y. Meng, Y. Zhao, J. Han, G. Su, B. Chen, J. Dai, *Biomaterials*, 2012, **33(5)**, 1437-1444.
- [17] F. Li, H. Tan, J. Singh, J. Yang, X. Xia, J. Bao, J. Ma, M. Zhan, S. T. Wong, *BMC Syst Biol*, 2013, **7 Suppl 2**, S12.
- [18] S. Liu, M. S. Wicha, *J Clin Oncol*, 2010, **28(25)**, 4006-4012.
- [19] S. Vinogradov, X. Wei, *Nanomedicine*, 2012, **7(4)**, 597-615.
- [20] J. El-Ali, P. K. Sorger, K. F. Jensen, *Nature*, 2006, **442(7101)**, 403-411.
- [21] P. J. Hung, P. J. Lee, P. Sabounchi, R. Lin, L. P. Lee, *Biotechnol. Bioeng.*, 2005, **89(1)**, 1-8.
- [22] F. K. Balagaddé, L. You, C. L. Hansen, F. H. Arnold, S. R. Quake, *Science*, 2005, **309(5731)**, 137-140.
- [23] Y. C. Chen, Y. H. Cheng, H. S. Kim, P. N. Ingram, J. E. Nor, E. Yoon, *Lab Chip*, 2014, **14(16)**, 2941-2947.
- [24] Y. C. Chen, P. Ingram, E. Yoon, *Analyst.*, 2014, **139(24)**, 6371-6378

- [25] M. D. Ungrin, C. Joshi, A. Nica, C. Bauwens, P. W. Zandstra, *PLoS One*, 2008, **3(2)**, e1565.
- [26] Y.-C. Chen, Z. Zhang, S. Fouladdel, Y. Deol, P. N. Ingram, S. P. McDermott, E. Azizi, M. S. Wicha, and E. Yoon, “Single Cell Dual Adherent-Suspension Co-Culture Micro-Environment for Studying Tumor-Stromal Interactions with Functionally Selected Cancer Stem-like Cells” *Lab Chip*, 2016, 16(15), 2935-45.
- [27] Y. C. Chen, X. Lou, Z. Zhang, P. Ingram, E. Yoon, *Sci. Rep.*, 2015, **5**, 12175.
- [28] A. Kunze, M. Giugliano, A. Valero, P. Renaud, *Biomaterials*, 2011, **32(8)**, 2088-2098.
- [29] V. Vickerman, J. Blundo, S. Chung, R. Kamm, *Lab Chip*, 2008, **8(9)**, 1468-1477.
- [30] I. K. Zervantonakis, C. R. Kothapalli, S. Chung, R. Sudo, R. D. Kamm, *Biomicrofluidics*, 2011, **5(1)**, 13406.
- [31] Y. Shin, S. Han, J. S. Jeon, K. Yamamoto, I. K. Zervantonakis, R. Sudo, R. D. Kamm, S. Chung, *Nat. Protoc.*, 2012, **7(7)**, 1247-1259.
- [32] E. Tumarkin, L. Tzadu, and E. Kumacheva, *Integr. Biol.*, 2011, **3**, 653-662.
- [33] E. Brouzes, M. Medkova, N. Savenelli, D. Marran, M. Twardowski, J. B. Hutchison, J. M. Rothberg, D. R. Link, N. Perrimon, and M. L. Samuels, *Proc Natl Acad Sci USA*, 2009, **106(34)**, 14195-14200.
- [34] S. V. Murphy, A. Atala, *Nat. Biotechnol.*, 2014, **32(8)**, 773-785.
- [35] A. B. Bernard, C. C. Lin, K. S. Anseth, *Tissue Eng. Part C Methods*, 2012, **18(8)**, 583-592.
- [36] K. A. Hassan, L. Wang, H. Korkaya, G. Chen, I. Maillard, D. G. Beer, G. P. Kalemkerian, and M. S. Wicha, *Clin Cancer Res.*, 2013, **19(8)**, 1972-1980.
- [37] N. Takebe, P. J. Harris, R. Q. Warren and S. Percy Ivy, *Nat Rev Clin Oncol.*, 2011, **8(2)**, 97-106.
- [38] A. Pannuti, K. Foreman, P. Rizzo, C. Osipo, T. Golde, B. Osborne, and L. Miele, *Clin Cancer Res.*, 2010, **16(12)**, 3141-3152.

Chapter 3:

- [1] D. Gonzalez de Castro, P. A. Clarke, B. Al-Lazikani, P. Workman, *Clin. Pharmacol. Ther.* 2012, 93 (3), 252–259.
- [2] J. Gagan, E. M. Van Allen, *Genome Med.* 2015, 7 (1), 80.
- [3] C. Cummings, E. Peters, L. Lacroix, F. Andre, M. Lackner, *M. Clin. Transl. Sci.* 2016, 9 (6), 283–292.
- [4] M. Arnedos, C. Vicier, S. Loi, C. Lefebvre, S. Michiels, H. Bonnefoi, F. Andre, *Nat. Rev. Clin. Oncol.* 2015, 12 (12), 693–704.
- [5] K. A. Lipinski, L. J. Barber, M. N. Davies, M. Ashenden, A. Sottoriva, M. Gerlinger, *Trends Cancer* 2016, 2 (1), 49–63.
- [6] Y. J. Park, R. Claus, D. Weichenhan, C. Plass, *Epigenetics and Disease* 2010, 25–49.
- [7] B. Lehner, *Nat. Rev. Genet.* 2013, 14 (3), 168–178.
- [8] M. Schneider, J. Schüler, R. Höfflin, N. Korzeniewski, C. Grüllich, W. Roth, D. Teber, B. Hadaschik, S. Pahernik, M. Hohenfellner, S. Duensing, *Urol. Oncol.: Semin. Orig. Invest.* 2014, 32 (6), 877–884.
- [9] W. Zheng, N. Thorne, J. McKew, *Drug Discovery Today* 2013, 18 (21-22), 1067–1073.

- [10] J. Moffat, J. Rudolph, D. Bailey, *Nat. Rev. Drug Discovery* 2014, 13 (8), 588–602.
- [11] E. W. Esch, A. Bahinski, D. Huh, *Nat. Rev. Drug Discovery* 2015, 14 (4), 248–260.
- [12] B. Al-Lazikani, U. Banerji, P. Workman, *Nat. Biotechnol.* 2012, 30 (7), 679–692.
- [13] R. Fisher, L. Pusztai, C. Swanton, *Br. J. Cancer* 2013, 108 (3), 479–485.
- [14] K. Masui, B. Gini, J. Wykosky, C. Zanca, P. Mischel, F. Furnari, W. Cavenee, *Carcinogenesis* 2013, 34 (4), 725–738.
- [15] G. R. Zimmermann, J. Lehár, C. T. Keith, *Drug Discovery Today* 2007, 12 (1-2), 34–42.
- [16] C. Holohan, S. Van Schaeybroeck, D. B. Longley, P. G. Johnston, *Nat. Rev. Cancer* 2013, 13 (10), 714–726.
- [17] V. T. Devita, R. C. Young, G. P. Canellos, *Cancer* 1975, 35 (1), 98–110.
- [18] D. A. Yardley, *Int. J. Breast Cancer* 2013, 2013, 1–15.
- [19] R. Macarron, M. N. Banks, D. Bojanic, G. S. Sittampalam, *Nat. Rev. Drug Discovery* 2011, 10 (3), 188–195.
- [20] J. Tang, L. Karhinen, T. Xu, A. Szwarzajda, B. Yadav, K. Wennerberg, T. Aittokallio, *PLoS Comput. Biol.* 2013, 9 (9), e1003226.
- [21] R. H. Shoemaker, *Nat. Rev. Cancer* 2006, 6 (10), 813–823.
- [22] US Food and Drug Administration. *Guidance for Industry: Codevelopment of Two or More New Investigational Drugs for Use in Combination*, 2013, 1-16.
- [23] L. A. M. Griner, R. Guha, P. Shinn, R. M. Young, J. M. Keller, D. Liu, I. S. Goldlust, A. Yasgar, C. Mcknight, M.B. Boxer, D. Y. Duveau, J.-K. Jiang, S. Michael, T. Mierzwa, W. Huang, M. J. Walsh, B. T. Mott, P. Patel, W. Leister, D. J. Maloney, C. A. Leclair, G. Rai, A. Jadhav, B. D. Peyser, C. P. Austin, S. E. Martin, A. Simeonov, M. Ferrer, L. M. Staudt, C. J. Thomas, *Proc. Natl. Acad. Sci.* 2014, 111 (6), 2349–2354.
- [24] S. Michael, D. Auld, C. Klumpp-Thomas, A. Jadhav, W. Zheng, N. Thorne, C. Austin, J. Inglese, A. Simeonov, *A. Assay Drug Dev. Technol.* 2008, 6 (5), 637–657.
- [25] G.-S. Du, J.-Z. Pan, S.-P. Zhao, Y. Zhu, J. M. D. Toonder, Q. Fang, *Anal. Chem.* 2013, 85 (14), 6740–6747.
- [26] L. A. M. Griner, R. Guha, P. Shinn, R. M. Young, J. M. Keller, D. Liu, I. S. Goldlust, A. Yasgar, C. Mcknight, M.B. Boxer, D. Y. Duveau, J.-K. Jiang, S. Michael, T. Mierzwa, W. Huang, M. J. Walsh, B. T. Mott, P. Patel, W. Leister, D. J. Maloney, C. A. Leclair, G. Rai, A. Jadhav, B. D. Peyser, C. P. Austin, S. E. Martin, A. Simeonov, M. Ferrer, L. M. Staudt, C. J. Thomas, *Proc. Natl. Acad. Sci.* 2014, 111 (6), 2349–2354.
- [27] R. Riahi, A. Tamayol, S. A. M. Shaegh, A. M. Ghaemmaghami, M. R. Dokmeci, A. Khademhosseini, *Curr. Opin. Chem. Eng.* 2015, 7, 101–112.
- [28] Y.-C. Chen, Z. Zhang, S. Fouladdel, Y. Deol, P. N. Ingram, S. P. Mcdermott, E. Azizi, M. S. Wicha, E. Yoon, *Lab Chip* 2016, 16 (15), 2935–2945.
- [29] J. Kim, D. Taylor, N. Agrawal, H. Wang, H. Kim, A. Han, K. Rege, A. Jayaraman, *Lab Chip* 2012, 12 (10), 1813–1822.
- [30] D. An, K. Kim, J. Kim, *J. Biomol. Ther.* 2014, 22 (4), 355–362.
- [31] R. Tallarida, L. S. Jacob, *Dose-Response Relation in Pharmacology*; Springer New York: New York, 2012.
- [32] B. G. Chung, L. A. Flanagan, S. W. Rhee, P. H. Schwartz, A. P. Lee, E. S. Monuki, N. L. Jeon, *Lab Chip* 2005, 5 (4), 401–406.

- [33] J. Y. Yun, S. Jambovane, S.-K. Kim, S.-H. Cho, E. C. Duin, J. W. Hong, *Anal. Chem.* 2011, 83 (16), 6148–6153.
- [34] J. H. Tsui, W. Lee, S. H. Pun, J. Kim, D.-H. Kim, *Adv. Drug Delivery Rev.* 2013, 65 (11-12), 1575–1588.
- [35] D. Antoni, H. Burckel, E. Josset, G. Noel, *Int. J. Mol. Sci.* 2015, 16 (3), 5517–5527.
- [36] A. Nyga, U. Cheema, M. Loizidou, *J. Cell Commun. Signal* 2011, 5 (3), 239–248.
- [37] Z. Zhang, Y.-C. Chen, Y.-H. Cheng, Y. Luan, E. Yoon, *Lab Chip* 2016, 16 (13), 2504–2512.
- [38] C. Li, D. G. Heidt, P. Dalerba, C. F. Burant, L. Zhang, V. Adsay, M. Wicha, M. F. Clarke, D. M. Simeone, *Cancer Res.* 2007, 67(3), pp.1030-1037.
- [39] V. A. Liu, W. E. Jastromb, S. N. Bhatia, *J Biomed Mater Res A*, 2002, 60.1: 126-134.
- [40] Y.-C. Chen, X. Lou, Z. Zhang, P. Ingram, E. Yoon, *Sci. Rep.* 2015, 5 (1), 12175.
- [41] J. C. Boik, R. A. Newman, R. J. Boik, *Stat. Med.* 2008, 27 (7), 1040–1061.
- [42] J. Fouquier, M. Guedj, *Pharmacol. Res. Perspect.* 2015, 3 (3), e00149.
- [43] T. Panczyk, A. Jagusiak, G. Pastorin, W. H. Ang, J. Narkiewicz-Michalek, *J. Phys. Chem. C* 2013, 117 (33), 17327–17336.
- [44] N. A. Mortensen, F. Okkels, H. Bruus, *Phys. Rev. E* 2005, 71 (5), 057301.
- [45] B. Burtneß, L. Thomas, R. Sipples, M. Mcgurk, S. Salikooti, M. Christoforou, G. Mirto, R. Salem, J. Sosa, R. Kloss, Z. Rahman, G. Chung, J. Lacy, J. R. Murren, *Cancer J*, 2007, 13 (4), 257–262.
- [46] M. W. Oster, R. Gray, L. Panasci, M. C. Perry, *Cancer* 1986, 57 (1), 29-33.
- [47] T. J. Ettrich, L. Perkhofer, G. V. Wichert, T. M. Gress, P. Michl, H. F. Hebart, P. Büchner-Stuedel, M. Geissler, R. Mueche, B. Danner, V. Kächele, A. W. Berger, M. Güthle, T. Seufferlein, *BMC Cancer* 2016, 16 (1), 21.
- [48] A. Lipton, C. Campbell-Baird, L. Witters, H. Harvey, S. Ali, *J. Clin. Gastroenterol.* 2010, 44 (4), 286–288.
- [49] G. Bellone, A. Carbone, V. Busso, T. Scirelli, A. Buffolino, C. Smirne, A. Novarino, O. Bertetto, L. Tosetti, G. Emanuelli, *Cancer Biol. & Ther.* 2006, 5 (10), 1294–1303.
- [50] R. K. Mehmood, *Oncol. Rev.* 2014, 8 (2), 97–108.
- [51] Bellone, Graziella, et al. "Antagonistic interactions between gemcitabine and 5-fluorouracil in the human pancreatic carcinoma cell line Capan-2." *Cancer biology & therapy* 5.10 (2006): 1294-1303.
- [52] S. Y. C. Choi, D. Lin, P. W. Gout, C. C. Collins, Y. Xu, Y. Wang, *Adv. Drug Delivery Rev.* 2014, 79-80, 222–237.
- [53] Conroy, Thierry, et al. "FOLFIRINOX versus gemcitabine for metastatic pancreatic cancer." *New England Journal of Medicine* 364.19 (2011): 1817-1825.
- [54] Poon, Christopher, et al. "Self-assembled nanoscale coordination polymers carrying oxaliplatin and gemcitabine for synergistic combination therapy of pancreatic cancer." *Journal of controlled release* 201 (2015): 90-99.

Chapter 4

- [1] Jögi, M. Vaapil, M. Johansson, and S. Pählman, *Uppsala J. Med. Sci.*, 2012, **117**(2), 217-224.

- [2] I. Dago-Jack, and A. T. Shaw, *Nat. Rev. Clin. Oncol.*, 2018, **15(2)**, 81.
- [3] M. C. Cabrera, R. E. Hollingsworth, and E. M. Hurt, *World J. Stem. Cells.*, 2015, **7(1)**, 27.
- [4] J. Liu, H. Dang, and X. W. Wang, *Exp. Mol. Med.*, 2018, **50**, e416
- [5] T. M. Grzywa, W. Paskal, and P. K. Włodarski, *Trans. Oncol.*, 2017, **10(6)**, 956-975.
- [6] L. O. B, D. M. Guimarães, C. H. Squarize, and R. M. Castilho, *Cancers*, 2018, **8(1)**, 7.
- [7] C. Swanton, *Cancer research*, 2012, **72(19)**, 4875-4882.
- [8] N. E. Navin, and J. Hicks, *Mol. Oncol.*, 2010, **4(3)**, 267-283.
- [9] C. M. Beaver, A. Ahmed, and J. R. Masters, *Plos One*, 2014, **9(2)**, e89834.
- [10] H. Li, X. Chen, T. Calhoun-Davis, K. Claypool, and D. G. Tang, *Cancer Research*, 2008, **68(6)**, 1820-1825.
- [11] T. A. Yap, M. Gerlinger, P. A. Futreal, L. Pusztai, and C. Swanton, *Sci. Trans. Med.*, 2012, **4(127)**, 127ps10.
- [12] B. Beck, and C. Blanpain, *Nat. Rev. Cancer*, 2013, **13(10)**, 727-738.
- [13] H. Clevers, *Nat. Med.*, 2011, **17(3)**, 313-319.
- [14] M. Shackleton, E. Quintana, E. R. Fearon, and S. J. Morrison, *Cell*, 2009, **138(5)**, 822-829.
- [15] B. Bao, A. Ahmad, A. S. Azmi, S. Ali, and F. H. Sarkar, *Current protocols in pharmacology*, 2013, **61(1)**, 14-25.
- [16] U. Karsten, and S. Goletz, *Springerplus*, 2013, **2(1)**, 301.
- [17] H. F. Bahmad, K. Cheaito, R. M. Chalhoub, O. Hadadeh, A. Monzer, F. Ballout, A. El-Hajj, D. Mukherji, Y-N. Liu, G. Daoud, W. Abou-Keir, *Front. Oncol.*, 2018, **8**, 347.
- [18] C. A. Gilbert, A. H. Ross, *J. Cell. Biochem.*, 2009, **108(5)**, 1031-1038.
- [19] Y.-C. Chen, P. N. Ingram, S. Fouladdel, S. P. McDermott, E. Azizi, M. S. Wicha, E. Yoon, *Sci. Rep.*, 2016, **6**, 27301.
- [20] J.-J. Duan, W. Qiu, S.-L. Xu, B. Wang, X.-Z. Ye, Y.-F. Ping, X. Zhang, X.-W. Bian, and S.-C. Yu, *Stem Cells Dev.*, 2013, **22(16)**, 2221-2239.
- [21] P. Mehta, C. Novak, S. Raghavan, M. Ward, and G. Met. *Mol. Biol. (Clifton, N.J.)*, 2018, **1692**, 61-75.
- [22] Y. Lombardo, A. de Giorgio, C. R. Coombes, J. Stebbing, and L. Castellano, *J. Vis. Exp.*, 2015, **97**, e52671.
- [23] S. Kim, and C. M. Alexander, *Biotech. Letters*, 2014, **36(3)**, 481-488.
- [24] R. Foty, *J. Vis. Exp.*, 2015, **51**, e2720.
- [25] S. Lindström, and H. Andersson-Svahn, *Lab Chip*, 2010, **10(24)**, 3363-3372.
- [26] Y-C. Chen, Z. Zhang, S. Fouladdel, Y. Deol, P. N. Ingram, S. P. McDermott, E. Azizi, M. S. Wicha, and E. Yoon, *Lab Chip*, 2016, **16(15)**, 2935-2945.
- [27] M. Cardinali, H. Pietraszkiwicz, J. F. Ensley, and K. C. Robbins, *Int. J. Cancer*, 1995, **61(1)**, 98-103.
- [28] K. A. Warner, A. Adams, L. Bernardi, C. Nor, K. A. Finkel, Z. Zhang, S. A. McLean, J. Helman, G. T. Wolf, V. Divi, L. Queimado, F. J. Kaye, R. M. Castilho, and J. E. Nör, *Oral Oncol*, 2013, **49(11)**, 1059-1066.
- [29] A. Adams, K. Warner, A. T. Pearson, Z. Zhang, H. S. Kim, D. Mochizuki, G. Basura, J. Helman, A. Mantesso, R. M. Castilho, M. S. Wicha, and J. E. Nör, *Oncotarget*, 2015, **6(29)**, 26633.

- [30] V. A. Liu, W. E. Jastromb and S. N. Bhatia, *J. Biomed. Mater. Res.*, 2002, **60(1)**, 126-34.
- [31] Y. H. Cheng, Y.-C. Chen, R. Brien and E. Yoon, *Lab Chip*, 2016, **16(19)**, 3708-3717.
- [32] G. M. Faustino, M. Gattass, S. Rehen, and C. J. P. de Lucena, *2009 IEEE Int. Symp. Biomed. Imag.: From Nano to Macro.*, Boston, MA, 2009, 799-802. doi: 10.1109/ISBI.2009.5193170.
- [33] J. Shao, W. Fan, B. Ma and Y. Wu, *Mol. Med. Rep.*, 2016, **14(6)**, 4991-4998.
- [34] R. B. Keithley, E. M. Weaver, A. M. Rosado, M. P. Metzinger, A. B. Hummon and N. J. Dovichi, *Anal. Chem.*, 2013, **85(19)**, 8910-8918.
- [35] I. Russo, A. Oksman, B. Vaupel and D. E. Goldberg, *Proc. Nat. Acad. Sci.*, 2009, **106(5)**, 1554-1559.
- [36] D. W. Clark and K. Palle, *Annals Trans. Med.*, 2016, **4(24)**, 518.
- [37] D. Raha, T. R. Wilson, J. Peng, D. Peterson, P. Yue, M. Evangelista, C. Wilson, M. Merchant and J. Settleman, *Cancer Research*, 2014, **74(13)**, 3579-3590.
- [38] Z. F. Lim and P. C. Ma, *J. Hema. Oncol.*, 2019, **12(1)**, 1-18.
- [39] D. Wu, D. C. Wang, Y. Cheng, M. Qian, M. Zhang, Q. Shen and X. Wang, *Sem. Cancer Biol.*, 2017, **42**, 13-19.
- [40] E. Rangel-Huerta and E. Maldonado, *Stem Cells Inter.* 2017, **2017**, 7602951.

Chapter 5

- [1] American Cancer Society (ACS). Cancer facts & figures 2018. ACS website. <https://www.cancer.org/research/cancer-facts-statistics/all-cancer-facts-figures/cancer-facts-figures-2018.html>. 2018. Accessed April 9, 2018.
- [2] Ravi, M.; Paramesh, V.; Kaviya, S.; Anuradha, E.; Solomon, F. P. J. *Cell. Physiol.* 2015, 230 (1), 16–26.
- [3] Williams, J. J. *Clin. Med. Res.* 2018, 7 (3), 41.
- [4] Edmondson, R.; Broglie, J. J.; Adcock, A. F.; Yang, L. *Assay Drug Dev. Technol.* 2014, 12 (4), 207–218.
- [5] Maltman, D. J.; Przyborski, S. A. *Biochem. Soc. Trans.* 2010, 38 (4), 1072–1075.
- [6] Langhans, S. A. *Front. Pharmacol.* 2018, 9.
- [7] Riedl, A.; Schleder, M.; Pudenko, K.; Stadler, M.; Walter, S.; Unterleuthner, D.; Unger, C.; Kramer, N.; Hengstschläger, M.; Kenner, L.; Pfeiffer, D.; Krupitza, G.; Dolznig, H. J. *Cell Sci.* 2016, 130 (1), 203–218.
- [8] Melissaridou, S.; Wiechec, E.; Magan, M.; Jain, M. V.; Chung, M. K.; Farnebo, L.; Roberg, K. *Cancer Cell Int.* 2019, 19 (1).
- [9] Halldorsson, S.; Lucumi, E.; Gómez-Sjöberg, R.; Fleming, R. M. *Biosens. Bioelectron.* 2015, 63, 218–231.
- [10] Meyvantsson, I.; Beebe, D. J. *Annu. Rev. Anal. Chem.*, 2008, 1, 423-449.
- [11] Li, X. J.; Valadez, A. V.; Zuo, P.; Nie, Z. *Bioanalysis* 2012, 4 (12), 1509–1525.
- [12] Gupta, N.; Liu, J. R.; Patel, B.; Solomon, D. E.; Vaidya, B.; Gupta, V. *Bioeng. Transl. Med.* 2016, 1 (1), 63–81.
- [13] Zhang, Z.; Chen, Y.-C.; Urs, S.; Chen, L.; Simeone, D. M.; Yoon, E. *Small* 2018, 14 (42), 1703617.

- [14] Chen, Y.-C.; Lou, X.; Zhang, Z.; Ingram, P.; Yoon, E. *Sci. Rep.* 2015, 5 (1).
- [15] Tung, Y.-C.; Hsiao, A. Y.; Allen, S. G.; Torisawa, Y.-S.; Ho, M.; Takayama, S. *Analyst* 2011, 136 (3), 473–478.
- [16] Patra, B.; Peng, C.-C.; Liao, W.-H.; Lee, C.-H.; Tung, Y.-C. *Sci. Rep.* 2016, 6 (1).
- [17] Jeong, S.-Y.; Lee, J.-H.; Shin, Y.; Chung, S.; Kuh, H.-J. *Plos One* 2016, 11 (7).
- [18] Lecault, V.; Vaninsberghe, M.; Sekulovic, S.; Knapp, D. J. H. F.; Wohrer, S.; Bowden, W.; Viel, F.; McLaughlin, T.; Jarandehi, A.; Miller, M.; Falconnet, D.; White, A. K.; Kent, D. G.; Copley, M. R.; Taghipour, F.; Eaves, C. J.; Humphries, R. K.; Piret, J. M.; Hansen, C. L. *Nat. Methods* 2011, 8 (7), 581–586.
- [19] Tomasi, R. F.-X.; Sart, S.; Champetier, T.; Baroud, C. N. *Biorxiv*, 2018.
- [20] Yuan, T.; Gao, D.; Li, S.; Jiang, Y. *Chin. Chem. Lett.* 2019, 30 (2), 331–336.
- [21] Xu, X.; Farach-Carson, M. C.; Jia, X. *Biotechnol. Adv.* 2014, 32 (7), 1256–1268.
- [22] Zuchowska, A.; Jastrzebska, E.; Chudy, M.; Dybko, A.; Brzozka, Z. *Analytica Chimica Acta* 2017, 990, 110–120.
- [23] Gong, X.; Lin, C.; Cheng, J.; Su, J.; Zhao, H.; Liu, T.; Wen, X.; Zhao, P. *Plos One* 2015, 10 (6).
- [24] Riss, T. L.; Moravec, R. A.; Niles, A. L.; Benink, H. A.; Worzella, T. J.; Minor, L. *Cell Viability Assays*, in *Assay Guidance Manual*, ed. Sittampalam, G. S.; Gal-Edd, N.; Arkin, M.; Auld, D.; Austin, C.; Bejcek, B.; Glicksman, M.; Inglese, J.; Lemmon, V.; Li, Z.; McGee, J.; McManus, O.; Minor, L.; Napper, A.; Riss, T.; Trask, O. J.; Weidner, J. Eli Lilly & Company and the National Center for Advancing Translational Sciences, Bethesda (MD), 2004–2013.
- [25] Cory, A. H.; Owen, T. C.; Barltrop, J. A.; Cory, J. G. *Cancer Commun.* 1991, 3 (7), 207–212.
- [26] Chen, C. L.; Mahjoubfar, A.; Tai, L.-C.; Blaby, I. K.; Huang, A.; Niazi, K. R.; Jalali, B. *Sci. Rep.* 2016, 6 (1).
- [27] Manak, M. S.; Varsanik, J. S.; Hogan, B. J.; Whitfield, M. J.; Su, W. R.; Joshi, N.; Steinke, N.; Min, A.; Berger, D.; Saphirstein, R. J.; Dixit, G.; Meyyappan, T.; Chu, H.-M.; Knopf, K. B.; Albala, D. M.; Sant, G. R.; Chander, A. *C. Nat. Biomed. Eng.* 2018, 2 (10), 761–772.
- [28] Eulenberg, P.; Köhler, N.; Blasi, T.; Filby, A.; Carpenter, A. E.; Rees, P.; Theis, F. J.; Wolf, F. A. *Nat. Commun.* 2017, 8 (1).
- [29] Blasi, T.; Hennig, H.; Summers, H. D.; Theis, F. J.; Cerveira, J.; Patterson, J. O.; Davies, D.; Filby, A.; Carpenter, A. E.; Rees, P. *Nat. Commun.* 2016, 7 (1).
- [30] Pärnamaa, T.; Parts, L. *G3* 2017, 7 (5), 1385–1392.
- [31] Christiansen, E. M.; Yang, S. J.; Ando, D. M.; Javaherian, A.; Skibinski, G.; Lipnick, S.; Mount, E.; O’Neil, A.; Shah, K.; Lee, A. K.; Goyal, P.; Fedus, W.; Poplin, R.; Esteva, A.; Berndl, M.; Rubin, L. L.; Nelson, P.; Finkbeiner, S. *Cell* 2018, 173 (3).
- [32] Cheng, Y.-H.; Chen, Y.-C.; Brien, R.; Yoon, E. *Lab Chip* 2016, 16 (19), 3708–3717.
- [33] Corey, J. M.; Gertz, C. C.; Sutton, T. J.; Chen, Q.; Mycek, K. B.; Wang, B.-S.; Martin, A. A.; Johnson, S. L.; Feldman, E. L. *J. Biomed. Mater. Res. A* 2009, 9999A.
- [34] Bielecka, Z. F.; Maliszewska-Olejniczak, K.; Safir, I. J.; Szczylik, C.; Czarnecka, A. M. *Biol. Rev.* 2016, 92 (3), 1505–1520.

- [35] Chen, Y.-C.; Ingram, P. N.; Fouladdel, S.; Mcdermott, S. P.; Azizi, E.; Wicha, M. S.; Yoon, E. *Sci. Rep.* 2016, 6 (1).
- [36] Shorten, C.; Khoshgoftaar, T. M. *J. Big Data* 2019, 6 (1).
- [37] Sebaugh, J. L. *Pharm. Stat.* 2011, 10 (2), 128–134.
- [38] Komarova, N. L.; Wodarz, D. *Proc. Natl Acad. Sci.* 2005, 102 (27), 9714–9719.
- [39] Gupta, P. B.; Onder, T. T.; Jiang, G.; Tao, K.; Kuperwasser, C.; Weinberg, R. A.; Lander, E. S. *Cell* 2009, 138 (4), 645–659.
- [40] Wen, S.-H.; Su, S.-C.; Liou, B.-H.; Lin, C.-H.; Lee, K.-R. *Cancer Cell Int.* 2018, 18 (1).
- [41] Xin, X. Development of 3D Cell-Based Assay for High Throughput Screening of Cancer Drugs. Doctoral dissertation, The Ohio State University: Columbus, OH, 2017.
- [42] Zhang, Q.-S.; Zhu, S.-C. *Frontiers of Information Technology & Electronic Engineering* 2018, 19 (1), 27–39.
- [43] Liu, L.; Chen, J.; Fieguth, P.; Zhao, G.; Chellappa, R.; Pietikäinen, M. *International Journal of Computer Vision* 2018, 127 (1), 74–109.
- [44] Tacar, O.; Sriamornsak, P.; Dass, C. R. *J. Pharm. Pharmacol.* 2012, 65 (2), 157–170.
- [45] Alcindor, T.; Beauger, N. *Curr. Oncol.* 2011, 18 (1).

Chapter 6

- [1] Hanahan, D. & Weinberg, R. A. Hallmarks of cancer: the next generation. *Cell*. **144**, 646–674 (2011).
- [2] Steeg, P. S. Tumor metastasis: mechanistic insights and clinical challenges. *Nat. Med.* **12**, 895–904 (2006).
- [3] Zeisberg, M. & Neilson, E. G. Biomarkers for epithelial-mesenchymal transitions. *J. Clin. Invest.* **119**, 1429–1437 (2009).
- [4] Chaw, S. *et al.* Epithelial to mesenchymal transition (EMT) biomarkers – E-cadherin, beta-catenin, APC and Vimentin – in oral squamous cell carcinogenesis and transformation. *Oral Oncol.* **48**, 997–1006 (2012).
- [5] Liu, F., Gu, L. N., Shan, B. E., Geng, C. Z. & Sang, M. X. Biomarkers for EMT and MET in breast cancer: An update (Review). *Oncol. Lett.* **12**, 4869-4876 (2016).
- [6] Giedt, R. J. *et al.* Computational imaging reveals mitochondrial morphology as a biomarker of cancer phenotype and drug response. *Sci. Rep.* **6**, 32985; 10.1038/srep32985 (2016).
- [7] Westermann, B. Bioenergetic role of mitochondria fusion and fission. *Biochim. Biophys. Acta.* **1817**, 1833-1838 (2012)
- [8] Peng, J.-Y. *et al.* Automatic Morphological Subtyping Reveals New Roles of Caspases in Mitochondrial Dynamics. *PLoS Comput. Biol.* **7**, e1002212 (2011).
- [9] Danuser, G. Computer Vision in Cell Biology. *Cell* **147**, 973–978 (2011).
- [10] Grys, B. T. *et al.* Machine learning and computer vision approaches for phenotypic profiling. *J. Cell Biol.* **216**, 65–71 (2016).
- [11] Breiman, L. Random forests. *Machine learning* **45(1)**, 5-32 (2001).
- [12] Zell, A. Simulation neuronaler netze (Vol. 1). Bonn: Addison-Wesley (1994).

- [13] Desai, S. C. A. P., Bhatia, S. N., Toner, M. & Irimia, D. Mitochondrial Localization and the Persistent Migration of Epithelial Cancer cells. *Biophys. J.* **104**, 2077–2088 (2013).
- [14] Whitesides, G. M. The origins and the future of microfluidics. *Nature* **442**, 368–373 (2006).
- [15] Xia, Y. & Whitesides, G. M. Soft lithography. *Annu. Rev. Mater. Sci.* **28**, 153-184, (1998)
- [16] El-Ali, J., Sorger, P. K. & Jensen, K. F. Cells on chips. *Nature* **442**, 403–411 (2006).
- [17] Chen, Y.-C. *et al.* Single-cell Migration Chip for Chemotaxis-based Microfluidic Selection of Heterogeneous Cell Populations. *Sci. Rep.* **5**, 9980; 10.1038/srep09980 (2015).
- [18] Lane, N. Mitochondrial disease: Powerhouse of disease. *Nature* **440**, 600–602 (2006).
- [19] Ridley, A. J. Cell Migration: Integrating Signals from Front to Back. *Science* **302**,1704–1709 (2003).
- [20] Detmer, S. A. & Chan, D. C. Functions and dysfunctions of mitochondrial dynamics. *Nat. Rev. Mol. Cell Biol.* **8**, 870-879 (2007).
- [21] Sheetz, M. P., Felsenfeld, D. P. & Galbraith, C. G. Cell migration: regulation of force on extracellular-matrix-integrin complexes. *Trends Cell Biol.* **8**, 51–54 (1998).
- [22] Gardel, M. L., Schneider, I. C., Aratyn-Schaus, Y. & Waterman, C. M. Mechanical integration of actin and adhesion dynamics in cell migration. *Annu. Rev. Cell Dev. Biol.* **26**, 315-333 (2010).
- [23] Ho, T. K. The random subspace method for constructing decision forests. *IEEE Trans. Pattern Anal. Mach. Intell.* **20**, 832-844 (1998).
- [24] Mellor, A., Haywood, A., Stone, C. & Jones, S. The Performance of Random Forests in an Operational Setting for Large Area Sclerophyll Forest Classification. *Remote Sens.* **5**, 2838–2856 (2013).
- [25] Bandyopadhyay, A. *et al.* Doxorubicin in Combination with a Small TGF β Inhibitor: A Potential Novel Therapy for Metastatic Breast Cancer in Mouse Models. *PLoS One* **5**, e10365 (2010).
- [26] Tu, Y. *et al.* Abstract 467: Mitochondrial dynamics regulates migration and invasion of breast cancer cells. *Cancer Res.* **72**, 467–467 (2012).
- [27] Chen, Y.-C. *et al.* Microfluidic high-throughput motility-based cell selection for enriching tumor initiating cells and discovering inhibition pathways of cancer migration. In *The 20th International Conference on Miniaturized Systems for Chemistry and Life Sciences (MicroTAS '16)* 49-50, Dublin, Oct. (2016).
- [28] Kitay, B. M., McCormack, R., Wang, Y., Tsoulfas, P. & Zhai, R. G. Mislocalization of neuronal mitochondria reveals regulation of Wallerian degeneration and NMNAT/WLDS-mediated axon protection independent of axonal mitochondria. *Hum. Mol. Genet.* **22**, 1601–1614 (2013).
- [29] Smith, M. C. P. *et al.* CXCR4 Regulates Growth of Both Primary and Metastatic Breast Cancer. *Cancer Res.* **64**, 8604–8612 (2004).

Chapter 7

- [1] Curtis, Louis T., Victor H. van Berkel, and Hermann B. Frieboes. "Pharmacokinetic/pharmacodynamic modeling of combination-chemotherapy for lung cancer." *Journal of theoretical biology* 448 (2018): 38-52.
- [2] Nagar, Swati. "Pharmacokinetics of anti-cancer drugs used in breast cancer chemotherapy." *Chemo Fog*. Springer, New York, NY, 2010. 124-132.
- [3] Van der Veldt, Astrid AM, Adriaan A. Lammertsma, and Egbert F. Smit. "Scheduling of anticancer drugs: timing may be everything." *Cell Cycle* 11.23 (2012): 4339-4343.

- [4] Jia, Jia, et al. "Mechanisms of drug combinations: interaction and network perspectives." *Nature reviews Drug discovery* 8.2 (2009): 111-128.
- [5] Seitz, Kathleen, and Ghui Zhou. "Pharmacokinetic drug - drug interaction potentials for therapeutic monoclonal antibodies: reality check." *The Journal of Clinical Pharmacology* 47.9 (2007): 1104-1118.
- [6] Garralda, Elena, Rodrigo Dienstmann, and Josep Taberner. "Pharmacokinetic/pharmacodynamic modeling for drug development in oncology." *American Society of Clinical Oncology Educational Book* 37 (2017): 210-215.
- [7] Doogue, Matthew P., and Thomas M. Polasek. "The ABCD of clinical pharmacokinetics." (2013): 5-7.
- [8] Nielsen, Michael A. *Neural networks and deep learning*. Vol. 2018. San Francisco, CA: Determination press, 2015.
- [9] Preuer, Kristina, et al. "Interpretable deep learning in drug discovery." *Explainable AI: Interpreting, Explaining and Visualizing Deep Learning*. Springer, Cham, 2019. 331-345.
- [10] Zhang, Quan-shi, and Song-Chun Zhu. "Visual interpretability for deep learning: a survey." *Frontiers of Information Technology & Electronic Engineering* 19.1 (2018): 27-39.
- [11] Cruz-Roa, Angel Alfonso, et al. "A deep learning architecture for image representation, visual interpretability and automated basal-cell carcinoma cancer detection." *International Conference on Medical Image Computing and Computer-Assisted Intervention*. Springer, Berlin, Heidelberg, 2013.
- [12] Vaswani, Ashish, et al. "Attention is all you need." *Advances in neural information processing systems*. 2017.
- [13] Xu, Kelvin, et al. "Show, attend and tell: Neural image caption generation with visual attention." *International conference on machine learning*. 2015.
- [14] Chen, Yaran, et al. "A visual attention based convolutional neural network for image classification." *2016 12th World Congress on Intelligent Control and Automation (WCICA)*. IEEE, 2016.
- [15] Jetley, Saumya, et al. "Learn to pay attention." *arXiv preprint arXiv:1804.02391* (2018).
- [16] Zheng, Heliang, et al. "Learning multi-attention convolutional neural network for fine-grained image recognition." *Proceedings of the IEEE international conference on computer vision*. 2017.